Coupling of Peridynamics and Inverse Finite Element Method for Shape Sensing and Crack Propagation Monitoring of Plate Structures

Adnan Kefal[1,2,3,*], Cagan Diyaroglu[2,3], Mehmet Yildiz[1,2,3], Erkan Oterkus[4]

[1]Faculty of Engineering and Natural Sciences, Sabanci University, Tuzla, Istanbul 34956, Turkey

[2]Integrated Manufacturing Technologies Research and Application Center, Sabanci University, Tuzla, Istanbul 34956, Turkey

[3]Composite Technologies Center of Excellence, Istanbul Technology Development Zone, Sabanci University-Kordsa, Pendik, Istanbul 34906, Turkey

[4]Department of Naval Architecture, Ocean and Marine Engineering, University of Strathclyde, Glasgow G4 0LZ, United Kingdom

*Corresponding author: adnankefal@sabanciuniv.edu

Abstract: A novel structural health monitoring approach is developed by coupling the inverse finite element method (iFEM) and peridynamic theory (PD) for real-time shape sensing analysis and crack propagation monitoring of plate structures. This hybrid method, called iFEM-PD, can account for deformation, stress, and damage states of any sensor-equipped structure in real time without the need for loading knowledge and regardless of the complexity of structural topology or boundary conditions. The integrated iFEM-PD approach first reconstructs continuous (full-field) deformations from discrete strain measurements and then utilizes them to obtain full-field strains within the structure. Subsequently, iFEM-reconstructed strains are employed with a suitable damage diagnosis index to quantify the critical (possibly damaged/cracked) zone of the structural domain. Next, this critical zone is modelled by populating PD material points and establishing non-local interactions between the material points. Enforcing the real-time deformations predicted by iFEM to the boundary material points of the PD domain as displacement boundary conditions, the deformations of the material points located internal to the damaged zone is recalculated through PD analysis. During this simulation, the damage prognosis is achieved by precisely modelling structural discontinuities (crack etc.) and analyzing crack propagation based on non-local particle interactions. The shape sensing and damage monitoring capabilities of the iFEM-PD method are numerically verified for crack monitoring problems of composite structures subjected to various static/dynamic loads. Also, the high accuracy of the iFEM-PD formulation is experimentally validated by comparing the numerical results with those of digital image correlation. Overall, the merits of the new approach are revealed for precise crack growth monitoring in composite structures.

Keywords: Structural health monitoring; inverse finite element method; peridynamic theory; shape sensing; crack monitoring; damage propagation; composite structures.

1. Introduction

Structural health monitoring (SHM) is an integrated and automated monitoring process to assess real-time damage state of various engineering structures used in the fields of marine [1], aerospace [2], and civil [3] engineering. Early diagnosis and posteriori prognosis of defects such as cracks, damages, corrosion through an SHM system can prevent the catastrophic failure of the structure, thereby playing a crucial role for decreasing the direct economic losses and increasing environmental and human safety. Considering large-scale structural systems, combination of sensor technologies and digital twins can enable collection of precise structural integrity information to be used for condition-based maintenance scheduling. In this context, robust and efficient sensing algorithms capable of performing real-time and full-field structural integrity assessment is required to construct effective SHM systems that can realize a reliable monitoring of the lifecycle phases of a structure [4].

Dynamic reconstruction of structural deformations from in situ measurements, the so-called shape sensing, is an inverse problem that requires combination of parametric mathematical models together with experimental measurements. In the last decades, new sensor technologies have been developed for real-time experimental data collection, which were extensively applied to monitoring of strains, displacements, and mechanical loads at the discrete positions of the structures [5-7]. Among existing sensor types, fiber optic sensing systems have become popular for SHM applications of aerospace structures since they can be practically embedded between plies of composite laminates for interior strain measurements [8-11]. As these distributed systems use light scattering methods such as Brillouin [12] or Rayleigh [13] scattering, they offer an advantage of continuous strain measurement along an optical cable. In addition to the sensor technologies, different shape sensing methods have been introduced over the years such as Ko's displacement theories [14-15], modal based algorithms [16-18], neural network algorithms [19-22], and inverse finite element method (iFEM) [23]. Moreover, Tikhonov regularization [24] were employed to solve the parametric differential equations of the inverse problems including sparse identification of nonlinear dynamical systems [25], inverse wave propagation [26], damage detection [27], among others.

In short, Ko's formulation [14-15] is based on simple analytical integration of in situ strain measurements, where appropriate boundary conditions are used to determine the integration

constants. Besides, the modal methods [16-18] employ continuous weighted basis functions to approximate displacements based on mode shapes of the structure and predict the unknown weights of the displacement function by using curve-fitting of experimental strains. Furthermore, neural network approaches [19-22] is based on training various classification and regression models via supervised/unsupervised learning algorithms to gain maximum information from the experimental measurements. Lastly, the iFEM [23] is a continuum-mechanics-based least-squares variational principle that can be categorized as a new class of shape sensing algorithms. More details of these algorithms with various numerical and experimental comparisons can be found in references [28-29].

Recent studies [30-31] have shown that iFEM methodology provides very robust and reliable deformation reconstruction results for both static and dynamic conditions. The iFEM has the following characteristics for shape sensing process: (1) Shape sensing without material and loading information, (2) modelling capability of complex plate/shell structural geometries, (3) applicability to any geometrical and/or natural boundary conditions, (4) suitability to deformation reconstruction in real time, and (5) insensitivity to measurement errors such as noisy strains. As a result, the iFEM methodology fulfills all requirements of a reliable SHM system as being the most general shape sensing method among the approaches mentioned above. Least-squares variational principle of iFEM enforces the match between analytical and experimental section strains of beam/plate/shell/solid geometries through a minimization process with respect to the unknown displacements, resulting in the partial differential equations. These equations are commonly solved in a weak form by using inverse finite elements where kinematic variables are approximated through Lagrangian shape functions.

Up to now, various inverse element formulations were proposed in literature ranging from beam to shell elements. The most attractive ones including iMIN3 [32], iQS4 [33], and iCS8 [34] inverse-shell elements employ C^0-continuous interpolation functions in accordance with the first-order shear deformation theory (FSDT). Particularly, the iQS4 element has recently gained a popularity for shape sensing applications on simple/complex geometries, e.g., ship and offshore structures [35-39] and stiffened aerospace panels [40-41], due to its merits for practical modelling of large-scale structures with low-cost sensor measurement and highly accurate displacement estimations [42-43]. Several studies have shown the superior applications of iFEM/iQS4 approach

for damage identification in monolithic/stiffened structures having isotropic/orthotropic material properties [44-49].

Furthermore, a variety of inverse-beam elements were developed for displacement monitoring of thick/thin beam structures [50-53]. Numerous combined experimental and numerical studies have proven their high efficiency and accuracy for real-time deformed shape detection [54-57]. Recently, isogeometric iFEM analysis [58-60] were introduced by employing the iFEM as a general framework and the non-uniform rational B-splines (NURBS) as the discretization strategy for both structural geometry and displacement domain. This new framework simply merges the concepts of isogeometric analysis [61-62] with the iFEM methodology. The first method [60] was developed for thin doubly-curved shell structures, which was simplified later for shape sensing applications of straight beams with variable cross sections [63-64]. Additionally, robust displacement theories such as refined zigzag theory (RZT) [65] have been combined with iFEM to reconstruct zigzag deformation through the thickness of sandwich plate [66], shell [67], and beam [68] structures. The predictive capabilities of iFEM-RZT method were numerically and experimentally verified for moderately thick wing-shaped sandwich panel in [69-70]. Recently, a two-step formulation, so-called "smoothed iFEM" [71], has been proposed to (*i*) generate smooth (continuous) strain data from discrete sensor measurement and (*ii*) use the continuous data for performing shape sensing by iFEM. The combined experimental and numerical results have validated the improved accuracy of smoothed iFEM against the classical formulations.

Full-field shape sensing information can be suitably utilized to perform structural anomaly identification, which is another important step of SHM to estimate exact damage location, size, and amount of material degradation. Current SHM developments to support damage diagnosis and/or characterization include investigation of guided waves and modal parameters [72-75] via acoustic sensors [76]. Since fiber reinforced polymer matrix materials are broadly used in manufacturing of primary load bearing structural components of aerospace structures, the robust anomaly identification approaches have extensively been implemented for laminated composite structures. Moreover, researchers have used methods such as acoustic emission, digital image correlation (DIC), infrared thermography, and fiber Bragg grating sensors in an individual/combined manner to understand the specific damage mode and its accumulation under various loading conditions in fiber reinforced laminates and sandwich structures [77-79]. Among

the methods mentioned herein, with the ability to provide local and global displacement field as discrete point clouds, the DIC system has become ever more appealing for failure analysis, thereby lending itself to become one of the most popular noncontact measurement systems [80].

Albeit their high specific strength and corrosion resistance properties, composite materials are prone to complex damage/failure mechanisms. These may include delaminations [81], fiber/matrix cracking [82], and face/core debonding [83] due to the continuous operational loading conditions over the service life of a structure. Current SHM methods to prognose full-field detail of gradual damage accumulation inside these composite materials followed by abrupt failure may be limited due to their simplified/inherent assumptions. To solve such a challenging problem as forward analysis (i.e., requiring knowledge of material, loading, constraint conditions), an advanced nonlocal continuum-mechanics formulation, peridynamic theory, has been proposed [84]. Peridynamics (PD) is a state-of-the-art theory for improved modelling of crack growth dynamics and damage simulation in materials and structures. Unlike classical continuum mechanics and/or linear elastic fracture mechanics, PD equations do not involve any spatial derivatives and do not require an external crack/damage growth criterion, thus being always valid regardless of discontinuities. Hence, since its first publication, various research studies have been dedicated to simulating failure analysis of different materials including multi-physics and multi-scale problems [85-87] and topology optimization [88-89].

In particular, the peridynamic theory to capture failure and damage in composites is first introduced in [90] where the matrix and delamination damages of graphite-epoxy laminates under low-velocity impact were predicted. Moreover, inhomogeneous nature of composite laminates was modelled considering volume fractions of stiff-fiber and softer-matrix materials to predict damage evolution of laminates with different fiber orientations using PD [91]. Besides, a robust homogenized peridynamic model [92] was developed for dynamic fracture analysis of fiber-reinforced composites utilizing a conical micro-modulus function for the homogenization process. Afterwards, this model was extended to partially and fully homogenized peridynamic models in [93] to capture accurate damage results in a three-point-bending experiment. Furthermore, the concept of transverse micro-modulus was introduced to refine the anisotropy of PD composite model [94]. More recently, orthogonal anisotropy of composite lamina was represented utilizing a lattice PD model as well [95]. The robustness of this model was extensively validated with tension

experiments of a notched lamina. Most recently, an efficient PD composite laminate model was implemented [96] adopting the kinematic relations of FSDT plate theory for transverse shear deformation effects. The accuracy of this method was demonstrated with double cantilever beam experiment.

Apart from those PD approaches for fracture simulations of laminate structures, a robust peridynamic composite model [97] was proposed by defining fiber and matrix bonds on 2D lamina as well as interlayer and shear bonds in the thickness direction between each lamina. This model was verified for different matrix cracking failures along fiber directions based on quasi-static problems. Later, it was used to analyze damage behavior of stiffened composite curved panel with a central slot in [98], where the PD model was also coupled with FEM to increase the computational efficiency. Additionally, this PD laminate model was implemented to simulate all damage types (matrix cracking, fiber breakage, mode I-II delaminations) of 13-plies composite laminate subjected to extreme shock/blast loading conditions in [99].

In this study, we propose a novel algorithm that enables the effective coupling of iFEM and PD, which can predict damage propagation based on discrete strain information such as sensor measurements. Here, we will clearly convey the novelty and originality of the present study by addressing the gap in literature in terms of structural anomaly identification and crack propagation. These can be listed as follows. (1) From an application point of view specific to SHM procedures, PD has never been utilized to characterize damage evaluation based on the real-strain information. (2) The application of iFEM in damage/crack propagation analysis of composite materials is still unexplored. (3) The combined usage of PD with novel iFEM techniques has not been investigated at all. One of the main novel aspects of the present study is to combine a strong and well-accepted nonlocal continuum theory, Peridynamics, and a powerful shape-sensing method, iFEM, to handle problems that would be otherwise rather impossible to treat by individual usage of either iFEM or PD as well as other traditional SHM methods. As such, iFEM can neither classify or prognose damage type and its complex mechanics (e.g., matrix failure, fiber breakage, etc.) and cannot handle damage propagation with detailed crack path evolution. As being a forward analysis technique, the PD may not be suitable for solving an inverse problem of shape sensing using sensor information. However, a need for a technique that can predict and prognose details of crack propagation using sensor information only is evident. Here, we have used the advantage of PD

theory for particularly treating the crack propagation prognosis of damaged structures that are concurrently monitored using iFEM methodology in real time. Coupling the iFEM tool with PD can be beneficial to understand crack growth dynamics in engineering structures by leveraging the full-field deformations/strains reconstructed by iFEM. All in all, to our best knowledge, this is the first study in literature that creates an important step towards combining PD together with the iFEM under a unique framework. It is important to note that nonlocal operator methods [100-101] have recently proposed to solve partial differential equations, where the extensive application areas of the formulation were proved regardless of any limitations like discretization pattern and horizon size. The present iFEM-PD methodology can also be extended by using these nonlocal operators for more applications of crack monitoring.

The remainder of this paper is organized as follows. Section 2 presents the individual mathematical formulations of iFEM and PD approaches and their synthesis to efficiently construct a database of shape sensing and SHM processes under both static and dynamic conditions of laminates. The effective coupling-algorithm and workflow of iFEM-PD hybrid system are also presented in relation to relevant equations. In section 3, analyses of various test cases are performed to provide numerical and experimental evidence of high accuracy of the iFEM-PD in terms of deformation reconstruction and damage prognosis. Concluding remarks are provided in Section 4.

2. Mathematical Formulation of the iFEM-PD Methodology for Shape Sensing and Crack Monitoring

In this section, the mathematical formulation of coupled iFEM and PD methodology will be presented for plate structures. Let us briefly describe the main inverse problem first. Rigid-body-motion of the plate is fully constrained, and external forces are applied to the plate. Moreover, the surface strain measurements are collected via strain sensors mounted at the discrete positions over the top/bottom bounding surfaces of the plate. The inverse problem herein is the full-field solution of the deformations in three-dimensional space of the plate without knowing the loading and material information and only using sensor data. Essentially, the iFEM methodology can be utilized to obtain a real-time solution of this problem. The deformation field provided by iFEM can be logically utilized to identify any damage scenario of the structure. Although there exist various attempts for such calculations, none of them is applied to crack propagation monitoring.

With the aid of a non-local continuum theory, peridynamics, it would be possible to account for realistic damage/crack propagation simulations of the engineering structures. Herein, the iFEM methodology is coupled with PD formulation to detect and characterize real-time damage mechanisms during SHM process. Therefore, iFEM-PD methodology can serve as a diagnostic and prognostic technology for various SHM systems used in the today's engineering industry.

2.1. The inverse finite element formulation for plate/shell structures

Consider a plate domain bounded as $\Omega = \left\{ (x_1, x_2, z) \subset \mathbb{R}^3;\ z \in [-h, +h];\ \mathbf{x} \equiv (x_1, x_2) \in A \subset \mathbb{R}^2 \right\}$ in a rectangular Cartesian coordinate system, where the plate is laminated with isotropic and/or orthotropic layers with a total thickness of $2h$ as shown in Fig. 1(a). Here, the x_1- and x_2- axes corresponds to the in-plane coordinates of the plate, and thickness coordinate is represented by the z-axis with $z = 0$ being the mid-plane of the laminate. For the solution of the inverse problem mentioned above, FSDT formulation is adopted to describe the deformation of a material point in the laminated plate as:

$$\mathbf{u} \equiv \begin{Bmatrix} u_1(\mathbf{x}, z) \\ u_2(\mathbf{x}, z) \\ u_z(\mathbf{x}, z) \end{Bmatrix} = \begin{bmatrix} 1 & 0 & 0 & z & 0 \\ 0 & 1 & 0 & 0 & z \\ 0 & 0 & 1 & 0 & 0 \end{bmatrix} \begin{Bmatrix} v_1(\mathbf{x}) \\ v_2(\mathbf{x}) \\ v_z(\mathbf{x}) \\ \theta_1(\mathbf{x}) \\ \theta_2(\mathbf{x}) \end{Bmatrix} \tag{1}$$

where u_1, u_2, and u_z are the components of the deformation vector, $\mathbf{u}$. These components are aligned with the positive directions of coordinate system as illustrated in Fig. 1(a). The $\mathbf{v} \equiv [v_1 \quad v_2 \quad v_z \quad \theta_1 \quad \theta_2]^T$ vector contains five kinematic variables of FSDT. Here, v_1 and v_2 are translations along the positive x_1- and x_2-axes, respectively, while v_z is transverse deflection along positive z-axis. Besides, θ_1 and θ_2 are bending rotations around x_2- and x_1-axes, in the given order. The positive directions of these variables are clearly depicted in Fig. 1(a) as well.

The infinitesimally small in-plane $(\varepsilon_{11}, \varepsilon_{22}, \gamma_{12})$ and transverse-shear $(\gamma_{1z}, \gamma_{2z})$ strains of a material point can be defined by taking the first-order derivatives of Eq. (1) with respect to the x_1, x_2, z axes as:

$$\begin{Bmatrix} \varepsilon_{11} \\ \varepsilon_{22} \\ \gamma_{12} \end{Bmatrix} = \begin{Bmatrix} v_{1,1} \\ v_{2,2} \\ v_{1,2}+v_{2,1} \end{Bmatrix} + z \begin{Bmatrix} \theta_{1,1} \\ \theta_{2,2} \\ \theta_{1,2}+\theta_{2,1} \end{Bmatrix} \equiv \mathbf{e}(\mathbf{v}) + z\boldsymbol{\kappa}(\mathbf{v}) \tag{2}$$

$$\begin{Bmatrix} \gamma_{1z} \\ \gamma_{2z} \end{Bmatrix} = \begin{Bmatrix} v_{z,1}+\theta_1 \\ v_{z,2}+\theta_2 \end{Bmatrix} \equiv \boldsymbol{\gamma}(\mathbf{v}) \tag{3}$$

where the vectors $\mathbf{e}$, $\boldsymbol{\kappa}$, $\boldsymbol{\gamma}$ contain membrane, bending, and transverse-shear section strains of the plate. These section strains are constant through the thickness of the laminate, yet they become a variable of the $\mathbf{x}$ coordinate since they are a function of the $\mathbf{v}$ vector only. Note that in Eqs. (2-3), the operator $(\bullet)_{,\alpha} \equiv \partial(\bullet)/\partial x_\alpha$ indicates the partial derivative of a functional with respect to $\mathbf{x}$ coordinates.

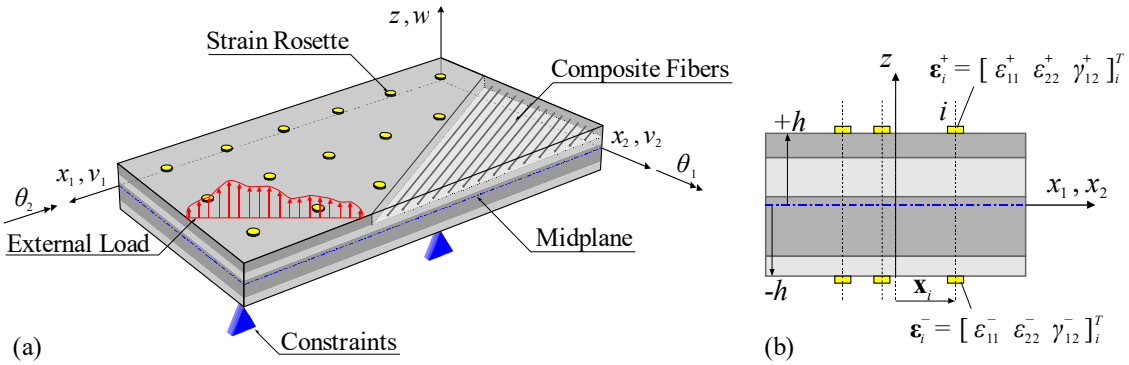

Fig. 1. (a) Geometry and kinematic variables of the laminated plate, (b) surface strain measurements with sensors.

The experimental counterparts of the section strains are one of the main inputs of the iFEM methodology. To obtain these experimental values at discrete positions of the plate, surface strain measurements need to be collected using strain sensors (i.e., strain gauges/rosettes, fiber optic sensors) as depicted in Fig. 1(b). Both membrane strain and bending curvatures of the plate can be experimentally determined using the surface strains that are measured at both top and bottom surfaces of the plate. Consider that the top and bottom strain rosettes provide discrete strains as a vector of $\boldsymbol{\varepsilon}_i^+ \equiv \left[(\varepsilon_{11}^+)_i \quad (\varepsilon_{22}^+)_i \quad (\gamma_{12}^+)_i \right]^T$, $\boldsymbol{\varepsilon}_i^- \equiv \left[(\varepsilon_{11}^-)_i \quad (\varepsilon_{22}^-)_i \quad (\gamma_{12}^-)_i \right]^T$, where the + and − superscripts denote the top and bottom surfaces, respectively. Besides, $i = 1, 2, ..., N_s$ subscript implies the discreteness of the strains collected from the spatial locations, $\{\mathbf{x}_i\}_{i=0}^{N_s} \in \Omega$, with N_s

9

being the total number of sensors attached to the domain. Additionally, normal strains along the x_1- and x_2-axes and engineering shear strain of the x_1x_2-plane are denoted by the symbols, $(\varepsilon_{11}^{\pm})_i$, $(\varepsilon_{22}^{\pm})_i$, $(\gamma_{12}^{\pm})_i$, respectively.

Utilizing in situ strain data, the experimental section strains can be defined at the positions of the sensors as:

$$\begin{Bmatrix} \mathbf{E}_i \\ \mathbf{K}_i \end{Bmatrix} = \frac{1}{2} \begin{Bmatrix} \boldsymbol{\varepsilon}_i^+ + \boldsymbol{\varepsilon}_i^- \\ (\boldsymbol{\varepsilon}_i^+ - \boldsymbol{\varepsilon}_i^-)/h \end{Bmatrix} \tag{4}$$

where the $\mathbf{E}_i$ and $\mathbf{K}_i$ vectors are experimental counterparts of the $\mathbf{e}$ and $\boldsymbol{\kappa}$ section strains at any sensor position, $\mathbf{x}_i$. The surface strain measurements $(\boldsymbol{\varepsilon}_i^+, \boldsymbol{\varepsilon}_i^-)$ cannot be directly employed to calculate the experimental conjugate of transverse-shear section strains, $\boldsymbol{\Gamma}_i$. Although various methods [67] have been suggested to compute the experimental values of $\boldsymbol{\Gamma}_i$, their contribution to the bending of the thin plates is much smaller than that of $\mathbf{K}_i$. Therefore, the role of this transverse-shear strain contributions can be safely eliminated for shape-sensing of thin plates, which is suitable for the geometry studied herein. Before performing an iFEM analysis, the experimental section strains can be smoothed utilizing strain pre-extrapolation techniques such as smoothing element analysis [102] and curve-fitting approaches [103]. For the sake of notational brevity, the smooth strains can be written without the subscript *i*, and the $\mathbf{E}_i \to \mathbf{E}$ and $\mathbf{K}_i \to \mathbf{K}$ notations are used to the describe the least-squares formulation of the iFEM hereafter.

Once the analytic and experimental values of the section strains are available for a given plate domain, their squared difference can be employed in the least-squares variational principle of iFEM methodology as:

$$\Phi(\mathbf{v}) = \frac{1}{\Omega}\int_{\Omega}\left(w_e \left\|\mathbf{e}(\mathbf{v}) - \mathbf{E}\right\|_2^2 + w_\kappa z^2 \left\|\boldsymbol{\kappa}(\mathbf{v}) - \mathbf{K}\right\|_2^2 + w_\gamma \left\|\boldsymbol{\gamma}(\mathbf{v}) - \boldsymbol{\Gamma}\right\|_2^2 \right) d\Omega \tag{5}$$

where the squared L_2-norms corresponding to the membrane, bending, and transverse-shear section strains are weighted by the w_i $(i = e, \kappa, \gamma)$ coefficients to generalize their individual contributions to the Φ functional. These weighting coefficients takes the value of one when the in situ section strains are available at a given position, $\mathbf{x}_i$. Otherwise, they are set to a small number

10

compared to unity ($\lambda \ll 1$, e.g., $\lambda = 10^{-3}$) to maintain accurate the strain-data connectivity between sensor positions.

The Eq. (5) can be rewritten more concisely by performing the through-the-thickness integral analytically as:

$$\Phi = \frac{1}{A}\int_A \left(w_e \mathbf{e}^T \left(\mathbf{e} - 2\mathbf{E}\right) + w_\kappa \frac{h^2}{3} \boldsymbol{\kappa}^T \left(\boldsymbol{\kappa} - 2\mathbf{K}\right) + w_\gamma \boldsymbol{\gamma}^T \left(\boldsymbol{\gamma} - 2\boldsymbol{\Gamma}\right) \right) dA + \varphi_0 \tag{6}$$

where the φ_0 is function of experimental measurements only, therefore its variation becomes zero, i.e., $\delta\varphi_0 = 0$. On the other hand, the first part of the Φ functional contains the quadratic and linear functions of the $\mathbf{v}$ deformations such as $\mathbf{e}^T\mathbf{e}$ and $\mathbf{e}^T\mathbf{E}$ terms, thereby leading to a non-zero variational equations. To obtain the final set of shape-sensing equations in accordance with the iFEM methodology, the error functional can be minimized with respect to the unknown deformations. For this purpose, its first variation can be calculated as:

$$\delta\Phi = \frac{2}{A}\int_A \left(w_e \delta\mathbf{e}^T \left(\mathbf{e} - \mathbf{E}\right) + w_\kappa \frac{h^2}{3} \delta\boldsymbol{\kappa}^T \left(\boldsymbol{\kappa} - \mathbf{K}\right) + w_\gamma \delta\boldsymbol{\gamma}^T \left(\boldsymbol{\gamma} - \boldsymbol{\Gamma}\right) \right) dA \tag{7}$$

which can be minimized as $\delta\Phi = 0$. This operation can be performed analytically by rewriting the section strains using derivative operator matrices as:

$$\chi = \mathbf{D}_\chi \mathbf{v} \quad (\chi = \mathbf{e}, \boldsymbol{\kappa}, \boldsymbol{\gamma}) \tag{8}$$

where $\mathbf{D}_\mathbf{e}, \mathbf{D}_\boldsymbol{\kappa}, \mathbf{D}_\boldsymbol{\gamma}$ matrices contain $\partial_i = \partial / \partial x_i$ $(i = 1, 2)$ derivative operators of x_1 and x_2 axes in relation to the section strain expressions as:

$$\mathbf{D}_\mathbf{e} \equiv \begin{bmatrix} \partial_1 & 0 & 0 & 0 & 0 \\ 0 & \partial_2 & 0 & 0 & 0 \\ \partial_2 & \partial_1 & 0 & 0 & 0 \end{bmatrix} \tag{9}$$

$$\mathbf{D}_\boldsymbol{\kappa} \equiv \begin{bmatrix} 0 & 0 & 0 & \partial_1 & 0 \\ 0 & 0 & 0 & 0 & \partial_2 \\ 0 & 0 & 0 & \partial_2 & \partial_1 \end{bmatrix} \tag{10}$$

$$\mathbf{D}_{\gamma} \equiv \begin{bmatrix} 0 & 0 & \partial_1 & 1 & 0 \\ 0 & 0 & \partial_2 & 0 & 1 \end{bmatrix} \tag{11}$$

Applying the first variation to the section strain expression given in Eq. (8), the following coupling equations can be formulated between variation of the $\mathbf{v}$ deformations and associated section strains as:

$$\delta\chi^T = \delta\mathbf{v}^T \mathbf{D}_{\chi}^{\ T} \quad (\chi = \mathbf{e}, \boldsymbol{\kappa}, \boldsymbol{\gamma}) \tag{12}$$

Substituting the Eq. (12) into the Eq. (7) and setting the resultant to zero yields:

$$\delta\Phi = \frac{\delta\mathbf{v}^T}{A}\int_A \left(w_e \mathbf{D}_{\mathbf{e}}^{\ T}\left(\mathbf{D}_{\mathbf{e}}\mathbf{v} - \mathbf{E}\right) + w_{\kappa}\frac{h^2}{3}\mathbf{D}_{\boldsymbol{\kappa}}^{\ T}\left(\mathbf{D}_{\boldsymbol{\kappa}}\mathbf{v} - \mathbf{K}\right) + w_{\gamma}\mathbf{D}_{\boldsymbol{\gamma}}^{\ T}\left(\mathbf{D}_{\boldsymbol{\gamma}}\mathbf{v} - \boldsymbol{\Gamma}\right)\right) dA = 0 \tag{13}$$

and rearranging the matrix-vector terms can give rise to the following final set of iFEM equations:

$$\delta\Phi = \delta\mathbf{v}^T\left(\mathbf{A}\mathbf{v} - \mathbf{q}\right) = 0 \rightarrow \mathbf{A}\mathbf{v} = \mathbf{q} \tag{14}$$

$$\mathbf{A} = \frac{1}{A}\int_A \left(w_e \mathbf{D}_{\mathbf{e}}^{\ T}\mathbf{D}_{\mathbf{e}} + w_{\kappa}\frac{h^2}{3}\mathbf{D}_{\boldsymbol{\kappa}}^{\ T}\mathbf{D}_{\boldsymbol{\kappa}} + w_{\gamma}\mathbf{D}_{\boldsymbol{\gamma}}^{\ T}\mathbf{D}_{\boldsymbol{\gamma}}\right) dA \tag{15}$$

$$\mathbf{q} = \frac{1}{A}\int_A \left(w_e \mathbf{D}_{\mathbf{e}}^{\ T}\mathbf{E} + w_{\kappa}\frac{h^2}{3}\mathbf{D}_{\boldsymbol{\kappa}}^{\ T}\mathbf{K} + w_{\gamma}\mathbf{D}_{\boldsymbol{\gamma}}^{\ T}\boldsymbol{\Gamma}\right) dA \tag{16}$$

where the $\mathbf{A}$ matrix contains second-order of differential operators and does not require experimental strain input whereas the $\mathbf{q}$ matrix constitutes first-order differential operators and is a function of experimental measurements. In fact, if the equation, $\mathbf{A}\mathbf{v} = \mathbf{q}$, is written explicitly, it involves five governing equations of the iFEM methodology. For example, if $\begin{bmatrix} \mathrm{E}_{11} & \mathrm{E}_{22} & \mathrm{E}_{12} \end{bmatrix}^T \subset \mathbf{E}_i$ and $\begin{bmatrix} \mathrm{K}_{11} & \mathrm{K}_{22} & \mathrm{K}_{12} \end{bmatrix}^T \subset \mathbf{K}_i$ are calculated at $\forall \mathbf{x}_i \ (i = 1, 2, ..., N_s)$ using sensor measurements, then their associated weights can be set as $w_e = w_{\kappa} = 1$. Moreover, setting $\boldsymbol{\Gamma} = 0$ and $w_{\gamma} = \lambda \in (10^{-6}, 10^{-2})$ in the case of modelling a thin plate, the partial differential equations of iFEM can be written in a component form on A as:

$$\frac{\partial^2 v_1}{\partial x_1^2} + \frac{\partial^2 v_1}{\partial x_2^2} + \frac{\partial^2 v_2}{\partial x_1 \partial x_2} = E_{11,1} + E_{12,2} \tag{17}$$

$$\frac{\partial^2 v_2}{\partial x_1^2}+\frac{\partial^2 v_2}{\partial x_2^2}+\frac{\partial^2 v_1}{\partial x_1 \partial x_2}=E_{22,2}+E_{12,1} \tag{18}$$

$$\frac{\partial^2 v_z}{\partial x_1^2}+\frac{\partial^2 v_z}{\partial x_2^2}+\frac{\partial \theta_1}{\partial x_1}+\frac{\partial \theta_2}{\partial x_2}=0 \tag{19}$$

$$\frac{\partial^2 \theta_1}{\partial x_1^2}+\frac{\partial^2 \theta_1}{\partial x_2^2}+\frac{\partial^2 \theta_2}{\partial x_1 \partial x_2}+\lambda\left(\frac{\partial v_z}{\partial x_1}+\theta_1\right)=\mathrm{K}_{11,1}+\mathrm{K}_{12,2} \tag{20}$$

$$\frac{\partial^2 \theta_2}{\partial x_1^2}+\frac{\partial^2 \theta_2}{\partial x_2^2}+\frac{\partial^2 \theta_1}{\partial x_1 \partial x_2}+\lambda\left(\frac{\partial v_z}{\partial x_2}+\theta_2\right)=\mathrm{K}_{22,2}+\mathrm{K}_{12,1} \tag{21}$$

Discretizing the structural domain with suitable inverse-elements, these equations can be written in an element level. For this purpose, the kinematic variables, $\mathbf{v}$, can be interpolated with suitable shape functions in an element domain. For example, iQS4 element is a viable four-node flat inverse-shell element that has recently gained a lot of attention from the shape-sensing research community. As shown in Fig. 2, this element has six degrees-of-freedom at its each node, i.e., three translations and three rotations including a drilling rotation, and interpolates the v_1, v_2, v_z translational kinematic variables using quadratic anisoparametric shape functions [104] and θ_1, θ_2 rotational kinematic variables by bilinear isoparametric shape functions.

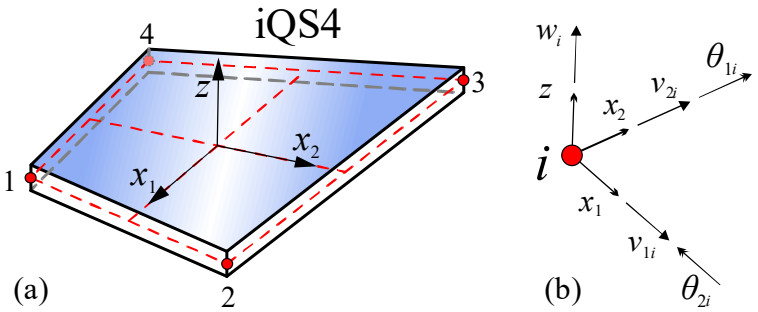

Fig. 2. (a) iQS4 element for shape sensing based on iFEM, (b) its degrees-of-freedom per node.

Utilizing the interpolation strategy of the iQS4 element, the $\mathbf{v}$ deformations can be expressed as $\mathbf{v}=\mathbf{N}^e\mathbf{v}^e$, where $\mathbf{v}^e$ is the element DOF vector, namely main unknowns of discretized domain, and the $\mathbf{N}^e$ matrix contains the shape functions of the iQS4 element. The explicit form of the shape function matrix can be formed by following the reference [33]. This approximation can be

13

substituted into the Eq. (8) and then the differential operator matrices $\mathbf{D}_i$ $(i=\mathbf{e},\boldsymbol{\kappa},\boldsymbol{\gamma})$ and shape function matrix $\mathbf{N}^e$ can be readily utilized to express iFEM equations over an iQS4 element as:

$$\mathbf{A}^e\mathbf{v}^e=\mathbf{q}^e \tag{22}$$

$$\mathbf{A}^e=\frac{1}{A_e}\int_{A_e}\left(w_e\mathbf{B}_\mathbf{e}{}^T\mathbf{B}_\mathbf{e}+w_\kappa\frac{h^2}{3}\mathbf{B}_\boldsymbol{\kappa}{}^T\mathbf{B}_\boldsymbol{\kappa}+w_\gamma\mathbf{B}_\boldsymbol{\gamma}{}^T\mathbf{B}_\boldsymbol{\gamma}\right)dA_e \tag{23}$$

$$\mathbf{q}^e=\frac{1}{A_e}\int_{A_e}\left(w_e\mathbf{B}_\mathbf{e}{}^T\mathbf{E}+w_\kappa\frac{h^2}{3}\mathbf{B}_\boldsymbol{\kappa}{}^T\mathbf{K}+w_\gamma\mathbf{B}_\boldsymbol{\gamma}{}^T\boldsymbol{\Gamma}\right)dA_e \tag{24}$$

where A_e is the area of the iQS4 element, the $\mathbf{B}_i$ $(i=\mathbf{e},\boldsymbol{\kappa},\boldsymbol{\gamma})$ matrices are strain-displacement relation matrices of the iQS4 element that can be calculated as $\mathbf{B}_i=\mathbf{D}_i\mathbf{N}^e$. These matrices involve the derivatives of shape functions with respect to local element coordinates as provided in reference [33]. In Eq. (22), the $\mathbf{A}^e$ matrix and $\mathbf{q}^e$ vector are the left-hand-side matrix and right-hand-side vector that are formed by considering the contributions of either analytical or experimental section strains.

Note that 2×2 gauss quadrature rule can be employed to numerically compute the area integrals given in Eqs. (23-24), for which necessary Jacobians needs to be established to perform the relevant isoparametric transformations between coordinate axes. After constructing the element level iFEM equations, they can be assembled to form the global system of the iFEM equations for the whole discretization. Then, applying relevant constraint boundary conditions, the global equations can be solved to give rise to the three-dimensional deformations in the full-field structural domain. This shape-sensing information can be utilized to compute the strain variations as provided in Eqs. (2-3); therefore, the full-field strain sensing of the structure can also be possible during the SHM process. For structural integrity assessment, von Mises equivalent strain can be predicted using the individual strain components under plane stress condition as:

$$\varepsilon_{vm}=\frac{\sqrt{2}}{3}\sqrt{\left(\varepsilon_{11}-\varepsilon_{22}\right)^2+\left(\varepsilon_{11}-\varepsilon_{zz}\right)^2+\left(\varepsilon_{22}-\varepsilon_{zz}\right)^2+6\left(\gamma_{12}^2+\gamma_{2z}^2+\gamma_{1z}^2\right)} \tag{25}$$

where the $\varepsilon_{zz}=\nu(\varepsilon_{11}+\varepsilon_{22})/(\nu-1)$ is the strain along thickness coordinate, and ν is the Poisson's ratio of the material. Finally, using the full-field strain components in the constitutive relations,

three-dimensional stresses can be obtained anywhere in the structural domain, thus enabling full-field stress sensing in real time.

2.2. Peridynamics for laminate mechanics

In the framework of peridynamics, it is assumed that the three-dimensional structure consists of an infinite number of infinitely small volumes that are so-called material points or particles. These material points interact with each other in areas where they are closest to each other as depicted in Fig. 3(a). Considering the conservation of linear and angular momentum, the PD equation of motion of a material point can be expressed in the form of integrodifferential equation as:

$$\rho\ddot{\mathbf{u}} = \mathbf{L}_{\mathbf{u}} + \mathbf{b} \quad \text{on} \quad \Omega\,,\ t \geq 0 \tag{26}$$

where the ρ is the density of the material, the $\ddot{\mathbf{u}}$ and $\mathbf{b}$ vectors contains the accelerations and body forces along x_1, x_2, and z coordinates at time t, respectively. Here, $\mathbf{L}_{\mathbf{u}}$ is the force per unit reference volume due to particles interactions, which can be stated as [84]:

$$\mathbf{L}_{\mathbf{u}}(\mathbf{x},t) = \int_{H_{\mathbf{x}}} \mathbf{f}\left(\mathbf{u}(\mathbf{x}',t) - \mathbf{u}(\mathbf{x},t), \mathbf{x}' - \mathbf{x}\right) \mathrm{d}V_{\mathbf{x}'} \quad \forall \mathbf{x} \in \Omega, \quad t \geq 0 \tag{27}$$

where $\mathbf{f}$ represents the interaction forces between particles located at $\mathbf{x}'$ and $\mathbf{x}$ positions, which are integrated over an interaction domain of the particle of interest, $\mathbf{x}$. This finite domain is referred to as 'horizon', which can be defined as $H_{\mathbf{x}} = \left\{ \left| \mathbf{x}' - \mathbf{x} \right| < \Psi;\ \Psi > 0;\ \forall \mathbf{x}' \in \Omega \right\}$, where Ψ is the size of the interaction domain, e.g., radius of a circular horizon in 2D space. In Eq. (27), the $\mathbf{u}(\mathbf{x}',t) \equiv \mathbf{u}'$ and $\mathbf{u}(\mathbf{x},t) \equiv \mathbf{u}$ terms are the deformation vectors of $\mathbf{x}'$ and $\mathbf{x}$ material points.

The Eqs. (26-27) are the general form of the peridynamic theory, and it can be restated for performing structural analysis of laminates in accordance with the bond-based PD composite model [97]. Given Ω laminate domain is composed of N layers, let $\Omega^{(k)} \subset \Omega$ denote the lamina level, i.e., $\Omega^{(k)} = \left\{ (\mathbf{x}, z) \subset \mathbb{R}^3;\ z \in \left[-h^{(k)}, +h^{(k)} \right];\ k = 1, 2, ..., N \right\}$, where the contact forces of the material points are defined in four different groups as shown in Fig. 3(b-c). The in-plane lamina-level interaction forces are classified according to the direction of the PD bonds relative to the fiber direction. Consider that the fibers are oriented by θ angle with respect to the reference x_1-

15

axis as illustrated in Fig. 3(b). In the *k*-th lamina, directional forces are introduced for fiber and arbitrary direction bonds. Here, the material point, i, interacts with material point, q, through fiber direction bond in its horizon, H_x, whereas it also interacts with other material points, p, through arbitrary direction bonds.

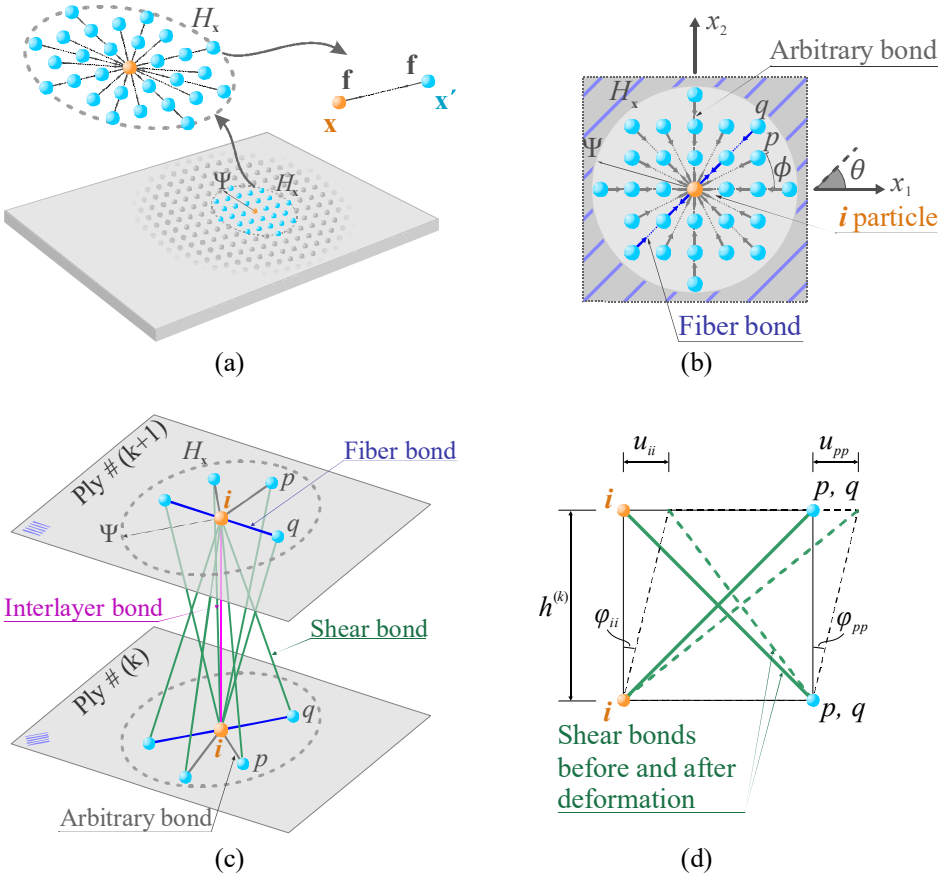

Fig. 3. (a) Interaction of material points in the horizon, (b) in-plane bond interactions, (c) interlaminar bond interactions, and (d) shear bond deformation for PD laminate model.

Moreover, in Fig. 3(c), two other peridynamic bonds, namely interlayer and shear bonds, between plies are introduced to account for the thickness direction deformation and/or deflection of a laminate subjected to bending loads. Essentially, two plies of a laminate are connected through interlaminar peridynamic bonds. The main material points, i, in *k*-th and (*k*+1)-th plies relate to interlayer bonds between plies. Besides, shear bonds are introduced by connecting the i material point in the *k*-th ply with the p and q particles in the (*k*+1)-th ply. Similarly, shear bonds are also established for the i particle in (*k*+1)-th ply as depicted in Fig. 3(c-d). With the existence of these bonds in the PD analysis, in-plane normal and shear deformations can be solved by considering

16

the internal forces generated by the in-plane bonds (fiber and arbitrary direction bonds), whereas out-of-plane deformation and transverse-shear deformations can be computed via interlaminar bonds (interlayer and shear bonds). Accordingly, the equation of motion can be defined for material points within the *k*-th lamina as :

$$\rho^{(k)}\ddot{\mathbf{u}}^{(k)} = \mathbf{L}_{\mathbf{u}}^{(k)} + \mathbf{b}^{(k)} \quad \text{on} \quad \Omega^{(k)} \,,\, t \geq 0 \tag{28}$$

where the $\rho^{(k)}$, $\ddot{\mathbf{u}}^{(k)}$, $\mathbf{b}^{(k)}$ terms represent density, acceleration, and body force of the $\mathbf{x}$ material point in the *k*-th lamina, in the given order. In addition, the $\mathbf{L}_{\mathbf{u}}^{(k)}$ peridynamic force is calculated by the integral of in-plane and interlaminar bond force densities over their respective horizons as:

$$\mathbf{L}_{\mathbf{u}}^{(k)} = \int_{H_{\mathbf{x}}} \mathbf{f}_{\phi}^{(k)}\left(\boldsymbol{\eta},\boldsymbol{\xi}\right) dV_{\mathbf{x}'} + \sum_{m=k+1,k-1} \left(\mathbf{f}_{N}^{(k)(m)}\left(\boldsymbol{\eta},\boldsymbol{\xi}\right) V_{\mathbf{x}'} + \int_{H_{\mathbf{x}}} \mathbf{f}_{S}^{(k)(m)}\left(\boldsymbol{\eta},\boldsymbol{\xi}\right) dV_{\mathbf{x}'} \right) \quad \forall \mathbf{x} \in \Omega^{(k)}, \quad t \geq 0 \tag{29}$$

where bond force vectors are the functions of relative displacement vector, $\boldsymbol{\eta} = \mathbf{u}' - \mathbf{u}$, and the relative position vector, $\boldsymbol{\xi} = \mathbf{x}' - \mathbf{x}$ of the bond. For interacting two particles, the horizon $H_{\mathbf{x}}$ always belongs to the $\mathbf{x}$ particle and contains its family members represented by the $\mathbf{x}'$ particle with the volume of $V_{\mathbf{x}'}$. This volume can be computed as $V_{\mathbf{x}'} = \Delta x \times \Delta x \times 2h^{(k)}$ for equal particle spacing of Δx.

In Eq. (29), single superscript (*k*) is used to indicate in-plane interaction terms associated the *k*-th lamina itself, and double superscripts (*k*)(*m*) are utilized to denote the interlaminar interaction terms between *k*-th and *m*-th laminae. For example, the $\mathbf{f}_{\phi}^{(k)}$ vector contains the bond forces corresponding to in-plane bonds aligned with either fiber or arbitrary directions. Besides, the $\mathbf{f}_{N}^{(k)(m)}$ and $\mathbf{f}_{S}^{(k)(m)}$ vectors include the interlayer and shear bond forces between *k*-th and *m*-th plies, respectively. These can be clearly defined between any two interacting material points as follows:

$$\mathbf{f}_{\chi} = \mu_{\chi} c_{\chi}\, s \frac{\boldsymbol{\xi} + \boldsymbol{\eta}}{\left|\boldsymbol{\xi} + \boldsymbol{\eta}\right|} \quad (\chi = N, \phi) \tag{30}$$

$$\mathbf{f}_{S} = \mu_{S} c_{S}\, \varphi \frac{\boldsymbol{\xi} + \boldsymbol{\eta}}{\left|\boldsymbol{\xi} + \boldsymbol{\eta}\right|} \tag{31}$$

where the $\mathbf{f}_N$, $\mathbf{f}_S$, and $\mathbf{f}_\phi$ peridynamic force vectors are aligned with the direction of the relative position of the interacting material points in the deformed configuration, i.e., $\boldsymbol{\xi}+\boldsymbol{\eta}=(\mathbf{x}'+\mathbf{u}')-(\mathbf{x}+\mathbf{u})$. The ($k$) and ($k$)($m$) superscripts are dropped from the bond force vectors in Eqs. (30-31) for conciseness of the mathematical expressions therein and hereafter. The s and φ symbols given in Eqs. (30-31) represent the stretch and shear angle between the $\mathbf{x}$ and $\mathbf{x}'$ material points and can be defined as $s=\left(\left|\boldsymbol{\xi}+\boldsymbol{\eta}\right|-\left|\boldsymbol{\xi}\right|\right)/\left|\boldsymbol{\xi}\right|$ and $\varphi=\left(u_{ii}+u_{pp}\right)/4h^{(k)}$ with u_{ii} and u_{pp} denoting the relative in-plane displacements of the corner points within two adjacent plies as clearly illustrated in Fig. 3(d).

Since the Eq. (29) does not contain spatial derivatives, this peridynamic laminate model becomes applicable to the mechanics of laminate even in the special cases such as the formation of a discontinuity (crack) within the structure. Thus, the peridynamic forces are related to the history-dependent failure parameters, μ_N, μ_S, μ_ϕ. Furthermore, in Eqs. (30-31), the interlayer, shear, and in-plane peridynamic forces are related with c_N, c_S, and c_ϕ bond constants. These material parameters can be found by equating the strain energy densities based on the classical continuum theory and peridynamics for simple loading conditions such as the uniform tensile (elongation) and shear tests [97]. Accordingly, the material parameters corresponding to each type of interaction can be expressed for three-dimensional PD laminate model as:

$$c_N=\frac{E_m}{2h^{(k)}V_{\mathbf{x}'}} \tag{32}$$

$$c_S=\frac{G_m/\pi\,2(h^{(k)})^2}{\left(\Psi^2+(2h^{(k)})^2\ln\left((2h^{(k)})^2/(\Psi^2+(2h^{(k)})^2)\right)\right)} \tag{33}$$

$$c_\phi=\begin{cases}c_F+c_A & \phi=\theta\\ c_A & \phi\neq\theta\end{cases} \tag{34}$$

where the E_m and G_m are the Young's and shear moduli of the matrix material, respectively. Note that the horizon size is commonly selected as $\Psi=3\Delta x$ for performing highly accurate PD analysis, where the Δx term represents the equal particle spacing between particles located at the same ply. As given in Eq. (34), the in-plane bond constant c_ϕ is determined by the angle of the bond relative

to the x_1-axis, ϕ. If this direction is equal to the fiber direction, then both arbitrary, c_A, and fiber, c_F, direction bond constants are taken into account to compute the c_ϕ constant. On the other hand, the contribution of c_F constant drops off for two material points interacting in any other direction except fiber direction. Accordingly, these bond constants can be defined using orthotropic material constants of a composite lamina as [97]:

$$c_A = \frac{4E_1E_2}{(E_1 - \frac{1}{9}E_2)\pi h^{(k)}\Psi^3} \tag{35}$$

$$c_F = \frac{E_1(E_1 - E_2)n}{(E_1 - \frac{1}{9}E_2)\pi h^{(k)}\Psi^2 \sum_{i=1}^{\psi}\xi_i} \tag{36}$$

where E_1 and E_2 are the elastic moduli of the composite material along the fiber and transverse directions, respectively, the n term is the total number of material points in the horizon, ξ_i $(i = 1, 2, ..., \psi)$ is the distance between material points interacting along the fiber direction within the horizon with ψ being the total number of these interactions. Note that the bond constants, c_ϕ, c_S and c_N, are derived under the assumption that the horizon of the main material point, $H_{\mathbf{x}}$, is completely inside the body. However, this is not generally the case for horizons truncated near the boundaries of a surface, which results in a reduction in material point stiffness. Hence, this stiffness reduction can be corrected by calculating the strain energy density of a material point with truncated horizon and equating it to that of CCM theory. Mathematical details of applying surface corrections can be viewed in [105].

In case of modelling any damage in the PD laminate analysis, the bond breaking criteria shown in Fig. 4 are defined to perform the crack propagation analysis of the laminate. Therefore, failure has direct relationship with critical parameters or stretches of the peridynamic bonds. In other words, if the mechanical strain and/or shear angle between any two material points exceeds its critical value, the interaction of two material points is terminated. These criteria are considered separately, namely, in-plane fiber and matrix direction, and between-layer vertical and shear directions.

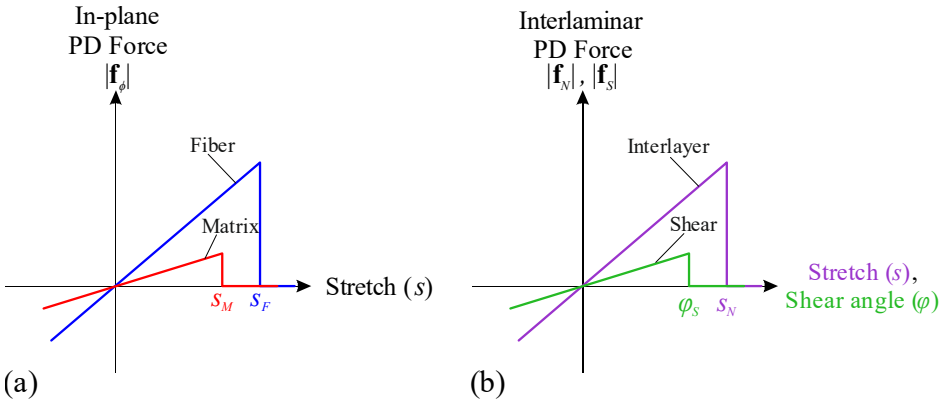

Fig. 4. Failure criteria of (a) in-plane and (b) interlayer bonds.

In Eqs. (30-31), the μ_N and μ_S damage parameters define interlaminar failures for mode I and mode II cracks in delamination for an orthotropic laminate (i.e., related with transverse normal and transverse shear deformations), in the given order. In addition to these out-of-plane damage modes, the μ_ϕ damage parameter can express the amount of in-plane damage that can be classified as matrix (μ_M) and fiber (μ_F) failures based on ϕ angle. All these parameters are defined as step functions ranging from 0 to 1 as follows:

$$\mu_N(t)=\begin{cases}1 & \text{if } s(t')<s_N \quad \forall t'\in[0,t]\\ 0 & \text{otherwise}\end{cases} \tag{37}$$

$$\mu_S(t)=\begin{cases}1 & \text{if } |\varphi(t')|<\varphi_S \quad \forall t'\in[0,t]\\ 0 & \text{otherwise}\end{cases} \tag{38}$$

$$\mu_\phi(t)=\begin{cases}1 & \text{if } \phi=\theta \text{ and } s(t')<s_F \quad \forall t'\in[0,t]\\ 1 & \text{if } \phi\neq\theta \text{ and } s(t')<s_M \quad \forall t'\in[0,t]\\ 0 & \text{otherwise}\end{cases} \tag{39}$$

where the s_F and s_M terms are the critical stretches of fiber direction and arbitrary (matrix) direction peridynamics bonds within the laminae. Depending on the in-plane bond type being evaluated, the μ_ϕ damage parameter can be equated to the matrix or fiber failure parameters, μ_M or μ_F (Fig. 4a). Moreover, the s_N symbol represents critical stretch of the interlayer peridynamic bonds and the φ_S defines the critical shear angle of shear peridynamic bonds between the layers (Fig. 4b). The critical values of s_N, φ_S, s_M, and s_F can be determined based on experimental

20

measurements of different lay-up configurations as indicated in [97]. Appropriately, they can be expressed in terms of orthotropic material properties laminae as:

$$s_N = \sqrt{\frac{G_{IC}}{h^{(k)} E_m}} \tag{40}$$

$$\varphi_S = \sqrt{\frac{G_{IIC}}{2h^{(k)} G_m}} \tag{41}$$

$$s_M = \sqrt{\frac{5G_{IC}}{9E_m \Psi}} \tag{42}$$

$$s_F = \sqrt{\frac{20G_{IC}}{9E_m \Psi}} \tag{43}$$

where G_{IC} and G_{IIC} parameters are the mode I and II critical energy release rates of the matrix material. The underlying idea on derivations of Eqs. (40-43) is that energies required to break all associated bonds crossing unit crack between particles within the same ply or two adjacent plies of a laminate are the same with related critical energy release rate. It is also important to note that the bonds are assumed to fail only in tension because of the predominant mechanism of the delamination/fiber/matrix failure modes of a laminate.

Local damage at any material point, $\varphi_\chi(\mathbf{x},t)$, can be expressed using the ratio of the number of broken (terminated) interactions in the non-local region to the total number of interactions as follows:

$$\varphi_\chi(\mathbf{x},t) = 1 - \frac{\int_{H_\mathbf{x}} \mu_\chi(t) dV_{\mathbf{x}'}}{\int_{H_\mathbf{x}} dV_{\mathbf{x}'}} \quad (\chi = N, S, M, F) \tag{44}$$

where local damage of a material point is characterized as matrix (φ_M) and fiber (φ_F) damages in the plies, and the delamination damage related with mode I (φ_N) and mode II (φ_S) cracks between plies. Note that the degree of damage herein is defined by a value between 0 and 1; where 0 indicates no damage at the material point, and 1 indicates complete damage. Also, a damage value of nearly 0.35 and greater indicates possible cracking.

For numerical implementation of the PD laminate model, all lamina-level peridynamic force relations can be summed for the composite laminate and equation of motion can be dynamically solved in three-dimensional space using explicit time-integration. To this end, after obtaining the acceleration in each time step, the velocity and displacement of each material point can be determined for the next time step by integrating the acceleration within the explicit time step. The advantage of explicit schemes over implicit time integration methods is that there is no need to solve equation of motion using large matrices because each equation related to the main material point, i, can be solved independently. However, the explicit schemes are stable only if the time step size, Δt, is smaller than a particular value. Adopting the von Neumann stability condition [106], a stable time-step size can be determined for a composite laminate as:

$$\Delta t < \sqrt{\frac{2\rho_{(i)}^{(k)}}{\sum_{p} c_{\phi} \frac{1}{\left|\xi_{(i)(p)}\right|} V_{(p)}^{(k)} + \frac{1}{h}\sum_{m} c_N V_{(i)}^{(m)} + \frac{1}{2h} c_S \left(\Delta x\right)^2}} \tag{45}$$

where $\xi_{(i)(p)}$ represents reference distance between material points p and i in the undeformed configuration, $\xi_{(i)(p)} = \left|\mathbf{x}_{(p)} - \mathbf{x}_{(i)}\right|$.

Contrary to classical continuum mechanics, normal and/or shear stresses are not considered when solving PD governing equations as is given in its original form [84]. Essentially, the interactions between particles are demonstrated by peridynamic forces, which are calculated as a function stretch, thus there is no direct definition of strain in PD formulation. Nevertheless, calculating the strain components within the scope of PD theory is important in terms of realizing numerical samples in the current study. In other words, experimental discrete strain data collected from a cracked structure under crack propagation case can be simulated through a PD analysis. This simulated data can be then utilized as experimental strain input in iFEM analysis for shape sensing and crack monitoring analysis. To this end, the strain calculation method used in the composite PD model [96] is adopted and rigorously implemented into the in-house PD laminate code.

Before summarizing the strain formulas of the PD model, three types of bonds needed for calculating in-plane strains are clearly described as:

1-) x_1*-axis normal bond:* As shown in Fig. 5, the material point *i* in the x_1x_2-plane can interact with a material point *j* in its horizon by forming a normal bond along the x_1 direction. In addition, material points *k* and *l* in the horizon of material point *i* can interact with material point *i* by establishing a normal bond in the x_2 direction. Similarly, material points *m* and *n* can interact with material points *j* via the x_2-axis directional bond.

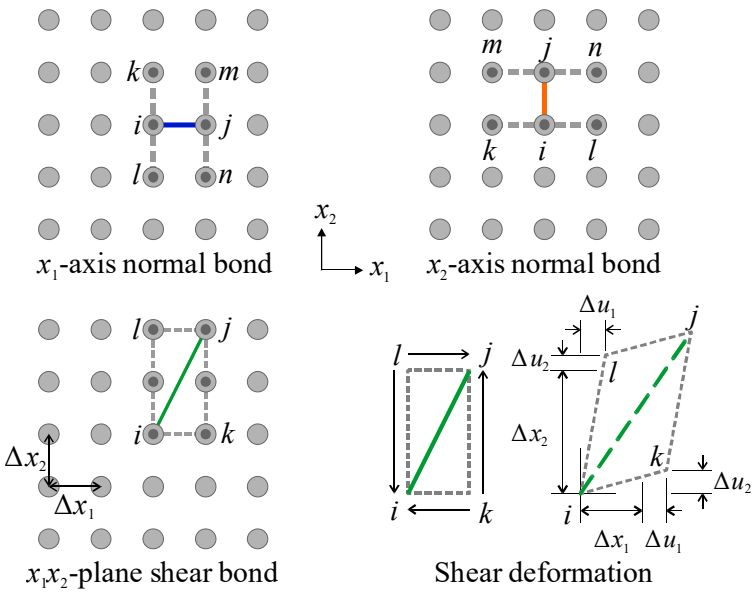

Fig. 5. Types of bonds formed by various directional interactions for PD strain calculation.

2-) x_2*-axis normal bond:* As shown in Fig. 5, the material point *i* can interact with material points *j* located along the x_2 direction in its horizon through a normal bond in the x_2-axis direction. In addition, material point *i* can interact with material points *k* and *l* along the normal bond in the x_1 -axis direction. Similarly, material point *j* can interact with material points *m* and *n* through the normal bond in the x_1-axis direction.

3-) x_1x_2 *-plane shear bond:* Any material point *i* on the x_1x_2 -plane can diagonally interact with any material point *j* within its horizon as such defining the shear bond between *i* and *j* material points as illustrated in Fig. 5. Then, to describe the shear strain that will occur in this case, one can consider the shear deformation of a rectangle formed by the interaction of material points *i*, *j*, *k*, and *l*.

23

Under the small displacement assumption, the normal strains along the x_1- and x_2-axes (ε_{ij}^{xx}, ε_{ij}^{yy}), and shear strains in the x_1x_2-plane (γ_{ij}^{xy}) of the *ij* bond can be expressed specifically for each bond type as:

$$\varepsilon_{ij}^{xx}=\begin{cases}\left(\dfrac{\Delta u_1}{\Delta x_1}\right)_{ij} & \text{if} \quad ij=x_1\text{-axis normal bond}\\ \dfrac{1}{2}\left(\left(\dfrac{\Delta u_1}{\Delta x_1}\right)_{kl}+\left(\dfrac{\Delta u_1}{\Delta x_1}\right)_{mn}\right) & \text{if} \quad ij=x_2\text{-axis normal bond}\\ \dfrac{1}{2}\left(\left(\dfrac{\Delta u_1}{\Delta x_1}\right)_{ik}+\left(\dfrac{\Delta u_1}{\Delta x_1}\right)_{jl}\right) & \text{if} \quad ij=x_1x_2\text{-plane shear bond}\end{cases} \tag{46}$$

$$\varepsilon_{ij}^{yy}=\begin{cases}\dfrac{1}{2}\left(\left(\dfrac{\Delta u_2}{\Delta x_2}\right)_{kl}+\left(\dfrac{\Delta u_2}{\Delta x_2}\right)_{mn}\right) & \text{if} \quad ij=x_1\text{-axis normal bond}\\ \left(\dfrac{\Delta u_2}{\Delta x_2}\right)_{ij} & \text{if} \quad ij=x_2\text{-axis normal bond}\\ \dfrac{1}{2}\left(\left(\dfrac{\Delta u_2}{\Delta x_2}\right)_{il}+\left(\dfrac{\Delta u_2}{\Delta x_2}\right)_{jk}\right) & \text{if} \quad ij=x_1x_2\text{-plane shear bond}\end{cases} \tag{47}$$

$$\gamma_{ij}^{xy}=\begin{cases}\left(\dfrac{\Delta u_2}{\Delta x_1}\right)_{ij}+\dfrac{1}{2}\left(\left(\dfrac{\Delta u_1}{\Delta x_2}\right)_{kl}+\left(\dfrac{\Delta u_1}{\Delta x_2}\right)_{mn}\right) & \text{if} \quad ij=x_1\text{-axis normal bond}\\ \left(\dfrac{\Delta u_1}{\Delta x_2}\right)_{ij}+\dfrac{1}{2}\left(\left(\dfrac{\Delta u_2}{\Delta x_1}\right)_{kl}+\left(\dfrac{\Delta u_2}{\Delta x_1}\right)_{mn}\right) & \text{if} \quad ij=x_2\text{-axis normal bond}\\ \dfrac{1}{2}\left(\left(\dfrac{\Delta u_1}{\Delta x_2}\right)_{il}+\left(\dfrac{\Delta u_1}{\Delta x_2}\right)_{jk}+\left(\dfrac{\Delta u_2}{\Delta x_1}\right)_{ik}+\left(\dfrac{\Delta u_2}{\Delta x_1}\right)_{jl}\right) & \text{if} \quad ij=x_1x_2\text{-plane shear bond}\end{cases} \tag{48}$$

where $\Delta(\bullet)_{ij}=(\bullet)_i-(\bullet)_j$ operates as displacement or coordinate difference between any two interacting *i* and *j* particles, and $u_{1\chi},u_{2\chi},x_{1\chi},x_{2\chi}\ (\chi=i,j,k,l,m,n)$ denote the displacement of material points *i, j, k, l, m, n* along the x_1- and x_2-axis, and their coordinates, in the given order. The strain expressions of the *ij* bond interactions herein can be used to find all in-plane strain

24

components for a material point *i* by simply averaging their contributions within the horizon as follows:

$$\varepsilon_{xx}(\mathbf{x}_i) = \sum_{j=1}^{n} \frac{\varepsilon_{ij}^{xx}}{n} \tag{49}$$

$$\varepsilon_{yy}(\mathbf{x}_i) = \sum_{j=1}^{n} \frac{\varepsilon_{ij}^{yy}}{n} \tag{50}$$

$$\gamma_{xy}(\mathbf{x}_i) = \sum_{j=1}^{n} \frac{\gamma_{ij}^{xy}}{n} \tag{51}$$

where the summation is performed for the total number of j particles available in the horizon of the i particle located at the $\mathbf{x}_i$ position, resulting in the in-plane strain component therein, $(\varepsilon_{xx}, \varepsilon_{yy}, \gamma_{xy})_i$. The PD strain calculation described herein will be utilized in the remainder of this study for generating the discrete strain data (i.e., simulated experimental strain) as input to the iFEM analysis during crack propagation condition of a laminate with crack performed by the presented PD laminate model.

2.3. iFEM-PD Coupling Algorithm

To summarize the motivation of the coupling of iFEM with PD theory for SHM, consider a real experimental tensile test of a laminate with a central crack depicted in Fig. 6. This structure will be exposed to further crack formation and/or crack propagation after a certain time due to the external loads. Is it possible to obtain how the crack propagates in the structure or how the full-field deformation of the damaged structure changes during crack propagation by using sensor information only? In fact, hybrid iFEM-PD method systematically answers this important engineering question: Yes, it is possible to diagnose crack propagation by performing the shape sensing with iFEM and subsequently using the reconstructed displacements to inform PD domain through relevant boundary conditions.

The integrated iFEM-PD system is a very important technology for performing real-time displacement and stress monitoring, detecting the types of damages/cracks, simulating the evolution of the cracks in a structure. The main purpose is to reconstruct full-field deformations using iFEM in real time from discrete strain (sensor) data and transform iFEM displacements to

25

full-field strains by simply taking their relevant derivatives. After this step, one can use the iFEM deformations to describe appropriate boundary condition on a local critical zone to predict the progress of possible damages/cracks through a PD simulation. Note that the critical zone can be selected anywhere in the structure depending on the unexpected von Mises strain differences between positions. In other words, the iFEM simulation can be performed in real time and examining the von Mises strains reconstructed through iFEM can be utilized to diagnose the unexpected von Mises strain concentrations in the laminate structure. The PD laminate model can then be created to zoom in the critical region of the structure for estimating the progress of the possible damage by the deformation data fed with iFEM.

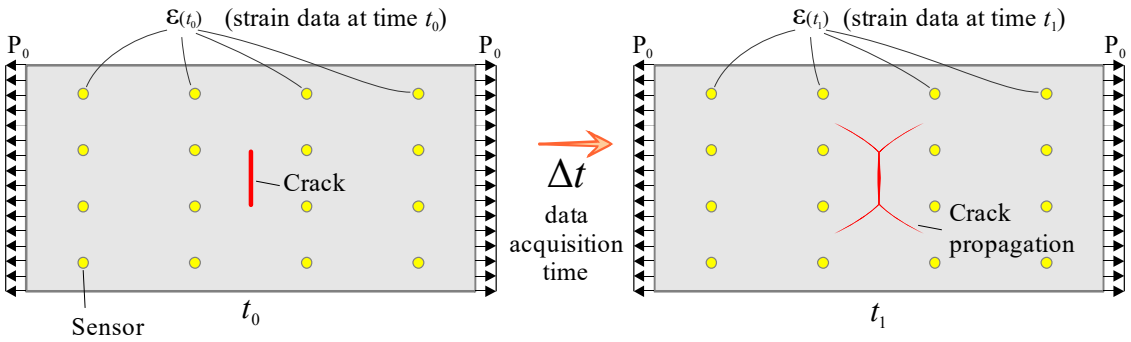

Fig. 6. Experimental test setup for crack monitoring

As shown in Fig. 7, let us assume that strain data is continuously collected in time intervals from a lamina with or without damage, and this data is analyzed by iFEM in real time. As the structure is under the effect of external loads, it will be constantly exposed to internal displacements. It is possible to predict these structural deformations and the resulting strains with iFEM by using only the sensor data as shown in Fig. 7. It may be not necessary to use the iFEM-PD damage diagnosis/prognosis system if there are no large strain variations. However, if the continuously monitored von Mises strains are above high critical values (e.g., larger than 8000 μm/m), then the strains differences between current (possibly damaged) and undamaged (reference) conditions can be employed to diagnose the critical damage zone and clearly distinguish its vicinity. To this end, the recent damage detection formula introduced in [44,46] can be utilized as:

$$D = \left| \frac{\varepsilon_{vm,current} - \varepsilon_{vm,undamaged}}{\varepsilon_{vm,undamaged}} \right| \times 100\% \tag{52}$$

26

where $\varepsilon_{vm,current}$ represents the currently measured von Mises strains and $\varepsilon_{vm,undamaged}$ denotes the von Mises strains before the damage occurrence. Since both strains are predicted by iFEM they become available in full-field structure. Therefore, the damage index given in Eq. (52) can be utilized to draw the main boundary of the local critical/damaged zone within the structure.

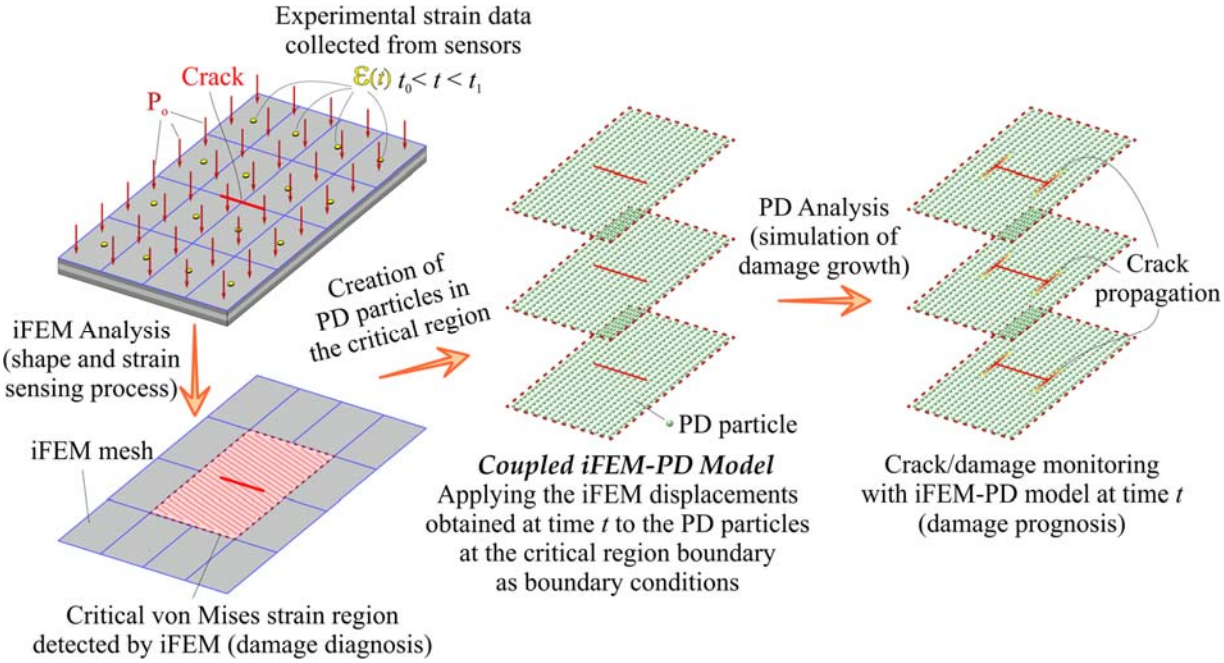

Fig. 7. Coupled iFEM-PD shape-sensing and crack-propagation monitoring model.

After the damage diagnosis step, as illustrated in Fig. 7, PD material points can be assigned within the boundaries of the critical zone at any time for prognosis of the damage accumulation. Expressly, PD material points can be defined inside the iFEM elements encountering high von Mises strains to detect damage in these areas. This definition is the first step of creating the coupled iFEM-PD system for three-dimensional laminates. As for the next step, the instantaneous displacements estimated by iFEM analysis can be applied as the boundary conditions along the edges of the PD laminate model. Subsequently, displacements in the damaged area can be recalculated by the PD model. Finally, these non-local displacements can be utilized with the PD damage criteria to examine the propagation of the cracks/damages during the PD simulation.

27

Algorithm 1 Shape Sensing and Crack Propagation Monitoring Algorithm

procedure COUPLED iFEM-PD ANALYSIS
  Read nodal coordinates, elements connectivity data, constraint boundary conditions, material properties of laminate
  for e = 1 to N_{el} **do**
    Compute $\mathbf{B}_i$ $(i = \mathbf{e}, \boldsymbol{\kappa}, \boldsymbol{\gamma})$ matrix using derivatives of shape functions, $\mathbf{D}_i\mathbf{N}^e$
    Compute $\mathbf{A}^e$ matrix defined in Eq. (23)
    Assemble $\mathbf{A}^e$ matrix to left-hand-side matrix of global system, $\boldsymbol{\Theta}$, for all inverse element
  end
  Reduce the $\boldsymbol{\Theta}$ matrix using constraint conditions and take its inverse to obtain $\boldsymbol{\Theta}_R^{-1}$
  for t_0 =1 to t_{all} **do**
    Strain data acquisition from sensors, $\boldsymbol{\varepsilon}_i^+(t_0), \boldsymbol{\varepsilon}_i^-(t_0)$
    run iFEM SOLUTION (Algorithm 2)
    if $D > D_{tr}$ (e.g., D_{tr} = 50%, 60%, …, 100%)
      Estimate critical zone, $\Omega^d \subset \Omega$
      run PD SOLUTION (Algorithm 3) on possibly damaged domain, Ω^d
    end
  end
  write Full-field data set for real-time shape sensing and crack monitoring
  exit

In the next loading increment, the collected sensor data can be analyzed by iFEM methodology again, and the deformed shape of the damaged structure can be updated. The resulting displacements are transferred to the PD composite model as boundary condition, and PD analysis can be reperformed for fracture simulation. In this framework, by creating a fully connected loop between the iFEM and PD models, the damage prognosis can be achieved until complete failure in the structure. The processes specified herein establish the coupled iFEM-PD method applicable for a lamina/laminate and/or isotropic materials depending on the suitability of selected individual iFEM/PD models. For ease of computer implementation of iFEM-PD approach, relevant computational flowchart and algorithm are given in Fig. 8 and Algorithms 1-3, respectively.

Algorithm 2 iFEM analysis for displacement and strain predictions, and damage diagnosis

1: **procedure** iFEM SOLUTION
2: Recall $\boldsymbol{\varepsilon}_i^+(t_0), \boldsymbol{\varepsilon}_i^-(t_0)$ sensors data and $\boldsymbol{\Theta}_R^{-1}$ matrix from Algorithm 1
3: **for** e = 1 to N_{el} **do**
4: Compute experimental section strains ($\mathbf{E}_i, \mathbf{K}_i$) using Eq. (4)
5: Compute $\mathbf{q}^e$ matrix defined in Eq. (24)
6: Assemble $\mathbf{q}^e$ matrix to right-hand-side matrix global set of system, $\boldsymbol{\Lambda}$, for all inverse elements
7: **end**
8: Reduce the $\boldsymbol{\Lambda}$ matrix using constraint condition to get $\boldsymbol{\Lambda}_R$
9: Solve the global displacement DOF of all elements, $\mathbf{U} = \boldsymbol{\Theta}_R^{-1}\boldsymbol{\Lambda}_R = [\mathbf{v}^1 \quad \cdots \quad \mathbf{v}^{N_{el}}]^T$
10: **for** e = 1 to N_{el} **do**
11: Compute the kinematic variables using element DOF vector, $\mathbf{v} = \mathbf{N}^e\mathbf{v}^e$
12: Use the $\mathbf{v}$ vector in Eq. (1) to get 3D full-field deformation vector, $\mathbf{u}$
13: Compute full-field strains using Eqs. (2-3), $[\varepsilon_{11} \quad \varepsilon_{22} \quad \gamma_{12}]^T$, $[\gamma_{1z} \quad \gamma_{2z}]^T$
14: Compute von Mises strains for the current state, $\varepsilon_{vm,current}$, using Eq. (25)
15: Compare initial (undamaged strains) with predicted strains and compute damage index, D, using Eq. (52)
16: **end**
17: **return** Full-field deformations, strains, and damage index (Algorithm 1: Line 11)

29

Algorithm 3 PD analysis for damage/crack propagation prognosis

procedure PD SOLUTION
    Recall laminate material properties and dimensions of Ω^d domain from Algorithm 1
    Initialize the PD parameters and compute bond constants using Eqs. (32-34), c_N, c_S, and c_ϕ
    Generate PD material points in the Ω^d domain, and import iFEM displacements at its boundary
    for i =1 to N_p **do**
        Determine the family members of each particle $\mathbf{x}_i$ in their horizon, $H_{\mathbf{x}}$
    end
    for i = 1 to N_p **do**
        for j = 1 to n **do**
            Compute surface correction factors for each particle, S_{cf}
            Apply pre-existing damage obtained from iFEM by breaking bonds according to Eqs. (37-39)
        end
    end
    Initialize displacement of the particles, $\mathbf{u}$, on Ω^d domain
    for n_i = 1 to N_t **do**
        Apply iFEM displacement as boundary condition for the step of n_i
        for i = 1 to N_p **do**
            for j = 1 to n **do**
                Compute PD force densities ($\mathbf{f}_N$, $\mathbf{f}_S$, $\mathbf{f}_\phi$) by multiplying Eqs. (30-31) with S_{cf} corrections
                Determine the failure condition of each material point using Eqs. (37-39)
                Solve equation of motion using PD force densities as given in Eqs. (27-28)
            end
        end
        Retrieve fiber, matrix, interlayer, shear damage of laminate, $\varphi_F, \varphi_M, \varphi_N, \varphi_S$, using Eq. (44)
    end
    return Full-field damage parameters φ_i in the critical zone (Algorithm 1: Line 14)

30

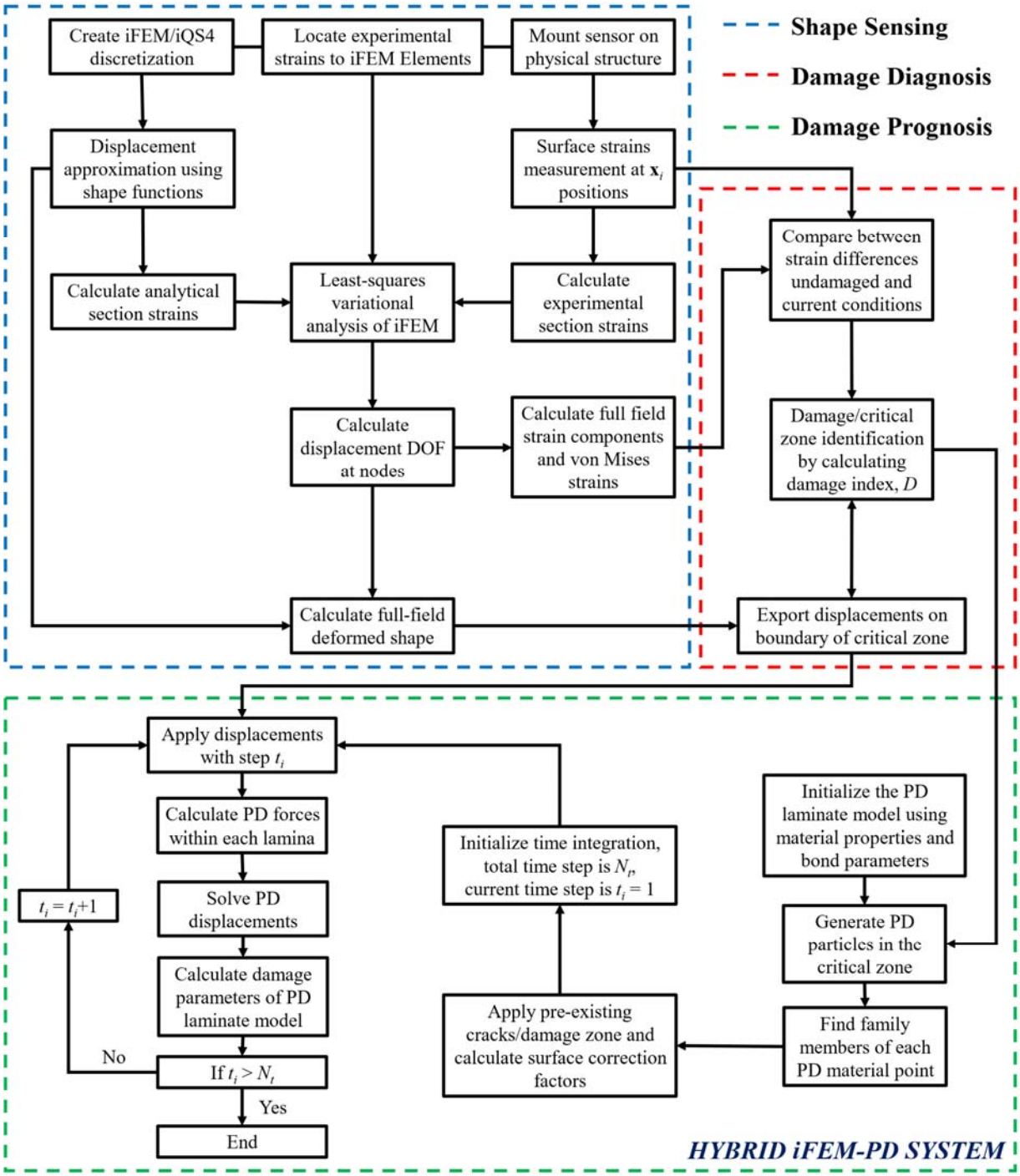

Fig. 8. Workflow of hybrid iFEM-PD system for its coding implementation.

31

3. Numerical and Experimental Examples

In this section, the integrated iFEM-PD model is applied to damage prognosis and diagnosis of composite materials. In this context, the static tensile/bending scenarios of a unidirectional composite lamina and a cross-ply laminate are numerically analyzed first. For each test case, forward analysis of the model is performed in case of the crack propagation to create a numerical (simulated) discrete strain input to the iFEM-PD analysis, namely representing experimental surface strains. In fact, there is no need for such an analysis to integrate the iFEM-PD model with a real/laboratory test case since the continuous/discrete experimental strain data can be collected from the in situ sensors (if the positions of the sensors are determined in the real structure), which can be used as direct input of the iFEM-PD code. After this numerical verification step, the high accuracy of the iFEM-PD method is then validated against DIC results for experimental shape sensing and crack propagation monitoring.

3.1. Damage detection and crack monitoring of a unidirectional thin lamina

The shape sensing and crack monitoring of a unidirectional thin lamina with a fiber angle direction of 0° with a central crack, shown in Fig. 9, is investigated under static tensile loading by using the iFEM-PD model. The main purpose here is to verify the accuracy of the integrated iFEM-PD formulation for a mode I crack opening condition in a composite lamina. The lamina has a rectangular geometry with a length of $L = 152.4$ mm, width of $W = 76.2$ mm, thickness of $2h^{(k)} = 0.1651$ mm, and crack size of $l = 17.78$ mm located at its center (i.e., parallel to the width of the plate). The fiber and transverse direction elastic modulus, major Poisson ratio and shear modulus of the composite (carbon fiber and epoxy) material are listed in Table 1. In addition, density, and critical energy release rate of the lamina as well as the elastic modulus, Poisson ratio, and shear modulus of isotropic matrix material are provided in Table 1.

Lamina is subjected to an axial tensile load of $P_0 = 159.96$ MPa from its left and right edges as depicted in Fig. 9. For simulating the experimental sensor-strain data (i.e., input for iFEM-PD analysis) in the case of the crack opening mode in the structure, first, a forward problem is analyzed using the PD laminate model. To this end, the lamina is modeled with a uniform particle distribution with the same grid spacing of $\Delta x = 0.635$ mm along both x and y directions. Therefore, in the PD model of the problem, there are 240 material points in the longitudinal

32

direction, while there are 120 material points in the width direction. In this PD model, the horizon size is selected as $\Psi = 3\Delta x$.

Table 1. Orthotropic material properties of the 0° unidirectional lamina and isotropic material properties of the epoxy.

Material	Elastic moduli, GPa	Poisson's ratio	Shear moduli, GPa	Density, kg/m^3	Critical energy release rate, J/m^2
Carbon-epoxy lamina	$E_1^{(k)} = 159.96$ $E_2^{(k)} = 8.96$ $E_3^{(k)} = 3.792$	$\nu_{12}^{(k)} = 1/3$ $\nu_{13}^{(k)} = 1/3$ $\nu_{23}^{(k)} = 1/3$	$G_{12}^{(k)} = 3.00537$ $G_{13}^{(k)} = 1.422$ $G_{23}^{(k)} = 1.422$	$\rho^{(k)} = 1700$	$G_{IC} = 2370$ $G_{IIC} = 592.5$
Epoxy	$E_m = 3.792$	$\nu_m = 1/3$	$G_m = 1.422$	-	-

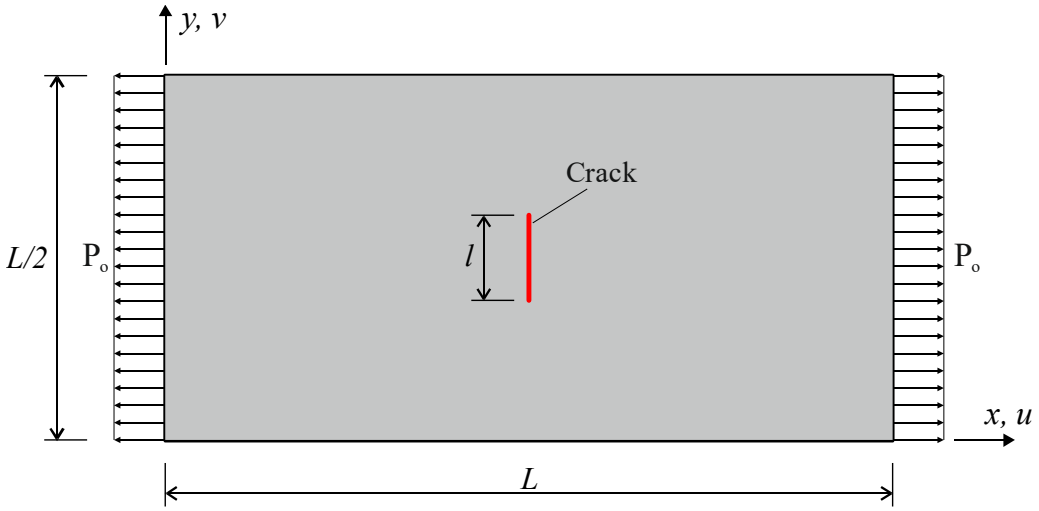

Fig. 9. Geometry and boundary conditions of a unidirectional lamina with central crack.

The PD analysis is statically solved using adaptive dynamic relaxation (ADR) technique for 10000 time steps, and the convergence of the displacement solution is examined at the points located far-field of the crack positions. The deformations obtained at the end of time integration are converted into strains for each PD material point with the formulas given in Eqs. (49-51). The strain values obtained here, namely the normal strains along the x- and y-axis and the xy-plane shear strains, are illustrated for both crack-free and crack-opening conditions as shown in Fig. 10. Note that for crack-opening condition, no fail zone is introduced at the vicinity of the crack tip to disable the breakage of the PD bonds. For the crack-free case, a constant distribution strain of

33

$\varepsilon_{xx} = P_o / E_1^{(k)} = 1\times10^{-3}$ m/m, $\varepsilon_{yy} = -\nu_{12}^{(k)}\varepsilon_{xx} = -3.333\times10^{-4}$ m/m, $\gamma_{xy} = 0$ is expected in the lamina analytically. As shown in Fig. 10, the PD model produces strain distribution that are highly compatible with these analytical results.

To elaborate on the results, the ε_{xx} strain contour obtained using PD can be examined for lamina without crack. It is seen that the light green colors are generally fixed and corresponding to 9.99×10^{-4}, except for the border regions of the plate. The main reason for the formation of tiny blue contours in the left and right boundaries of the plate can be attributed to the truncated horizons of the material points. Surface effect correction coefficients can be used to compensate for this surface effect [105]. However, the mentioned surface effect has only a negligible effect on the solution of the inverse problem (i.e., discussed later in this section) because the critical strain solution that is sought in the inner area of the plate, which has been obtained correctly. Similarly, when the ε_{yy} contour distribution is examined, a constant color distribution of approximately -3.36×10^{-4}, which corresponds to green color, was reached in the area inside the plate. Moreover, according to the γ_{xy} contour distribution obtained from the PD model, nearly zero constant shear strains are obtained in the range of $\pm4.75\times10^{-6}$ in the plate area excluding the corners of the plate. All results agree with the analytical values, demonstrating the accuracy of our in-house coding implementation as well as the PD laminate model for simulating synthetic sensor-strain data.

Additionally, when the strain values obtained for crack opening case is examined from Fig. 10, it is observed that all strain values have reached their absolute maximum values at the crack tips. In other words, in these critical regions, highly dense strain concentration is observed as known from the fundamental of the classical fracture mechanics. Besides, as can be seen in these contour images that the surface effects are dramatically reduced in this case due to the condensed strain regions. These results overall reveal the correctness of the predicted strain distribution for both crack-free and crack-opening conditions of the plate, thereby validating accuracy of simulated strains input for iFEM-PD analysis.

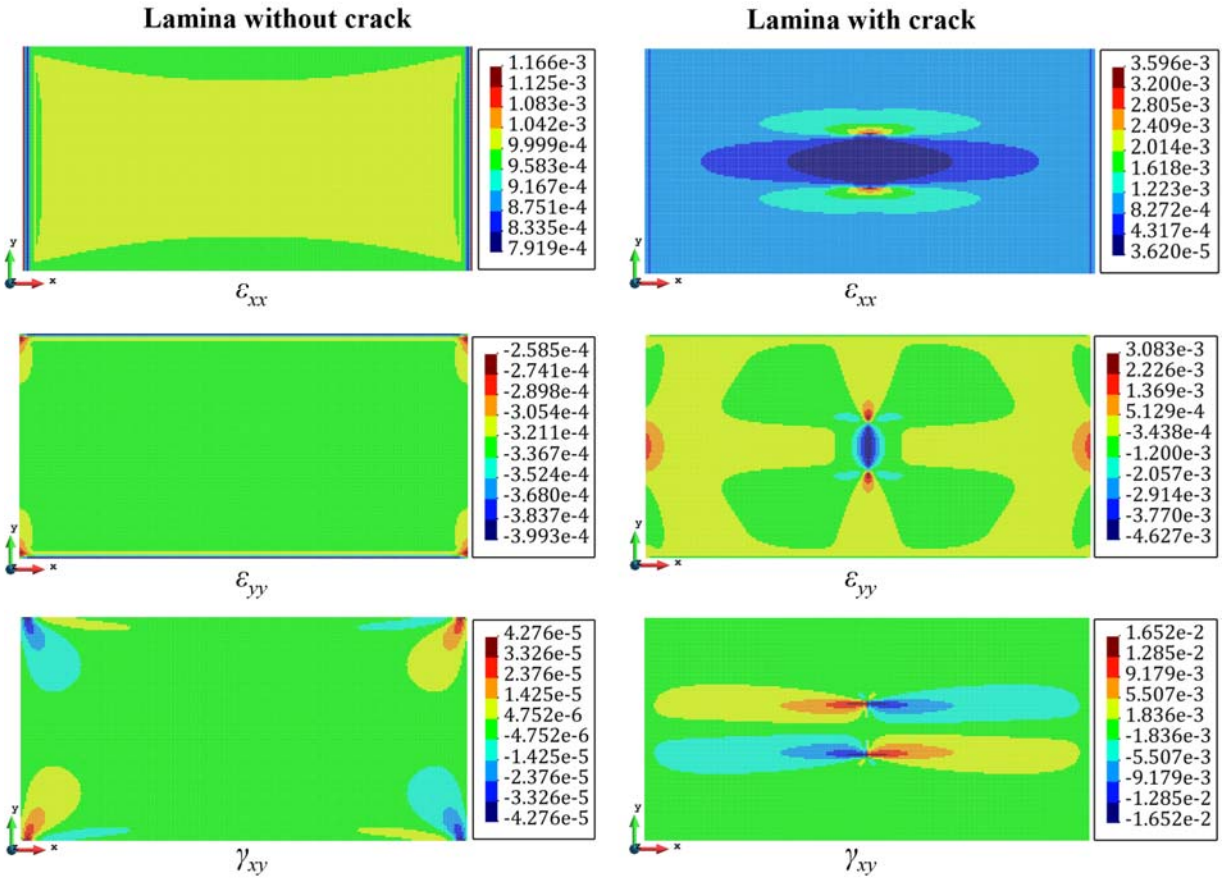

Fig. 10. Normal and shear strain contours of the lamina with/without crack.

Dense, medium, and sparse iQS4 discretization named as iFEM (80×40), iFEM (48×24), and iFEM (16×8) models are created for the shape sensing analysis of the lamina. At this stage, the main concern is to evaluate the sensitivity of the iFEM-PD results against the mesh density, therefore it is thought that there is a strain sensor positioned on all inverse elements in each iQS4 discretization. Note that the number of sensors can be reduced especially for the application to the real experimental setup by using a suitable weighting strategy of iFEM methodology for sensor placement [69]. Alternatively, sparse sensor data can be smoothed by employing 'a priori' smoothing techniques [102], resulting in full sensor data even for dense iFEM domains. Thus, it is possible to use a high density iFEM mesh even with a sparse sensor distribution as indicated in [71]. An example of sensor placement for iFEM (16×8) model is given in Fig. 11. Here, the strain data is generated at the center of each inverse element by performing a crack/damage growth simulation based on the PD lamina model with 10000 ADR time steps. This data is sampled and transferred to iFEM-PD code as an input at each 200 ADR time steps, thus yielding strain data

35

acquisition time range of $t \in [1, 50]$ for the shape sensing analysis. Such an intensive real-time data can be practically processed in a real experimental setup, thanks to the real-time monitoring capabilities of the iFEM-PD hybrid damage detection system.

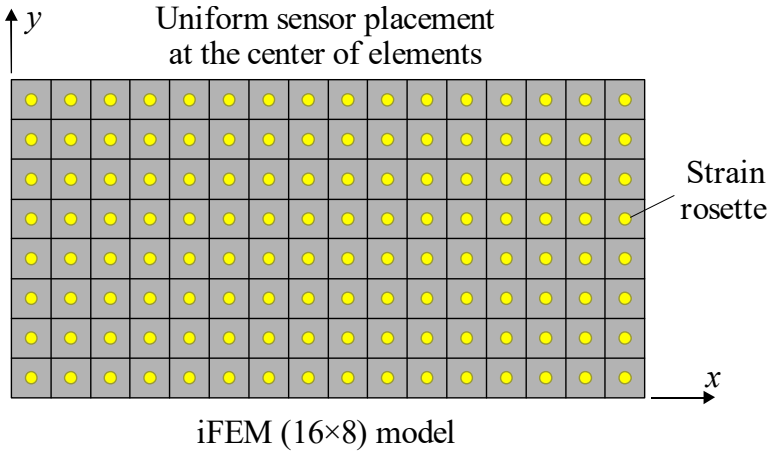

Fig. 11. Sparse resolution of iQS4 model for shape-sensing analysis.

In Figs. 12-14, total displacement contours obtained with three different iQS4 models in three different time steps are compared with the contours of the reference solutions obtained with PD in the respective time steps. As can be seen from these figures that the contours obtained by iFEM are almost indistinguishable from those of reference solution, demonstrating the highly accurate full-field shape sensing capability of the iFEM. When the maximum deformations predicted by iFEM are compared with the maximum values of the reference solutions, it is seen that the results obtained with the densest iFEM (80×40) model possess approximately 0.4%, 1.7% and 3.3% errors in different time steps, respectively. Looking at displacement percent difference for medium (48×24) and sparse (16×8) resolutions of iFEM meshes for the same time steps, they are computed as 1.31%, 3.4%, 4.8% and 3.3%, 4.2%, 4.3%, in the given order. Expectedly, as the mesh density increases, the margin of error generally decreases. The main reason why the margin of error increases for each mesh in ascending time steps can be attributed to the propagation of the damage/crack failure within the laminate.

36

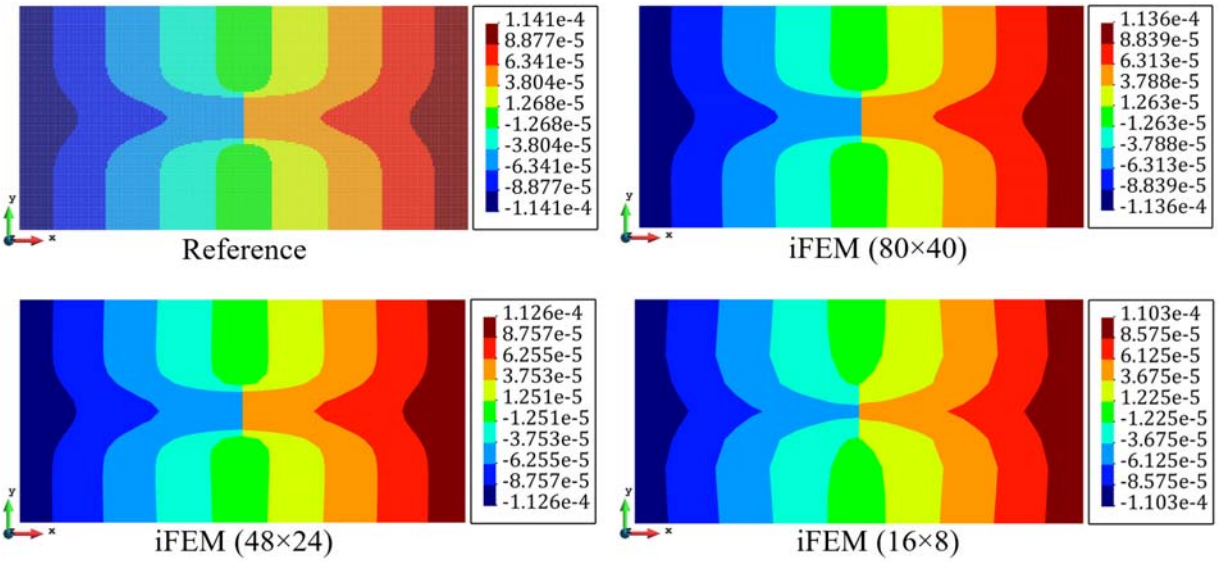

Fig. 12. Contours of u axial deformation at time step, $t = 7$, for unidirectional lamina.

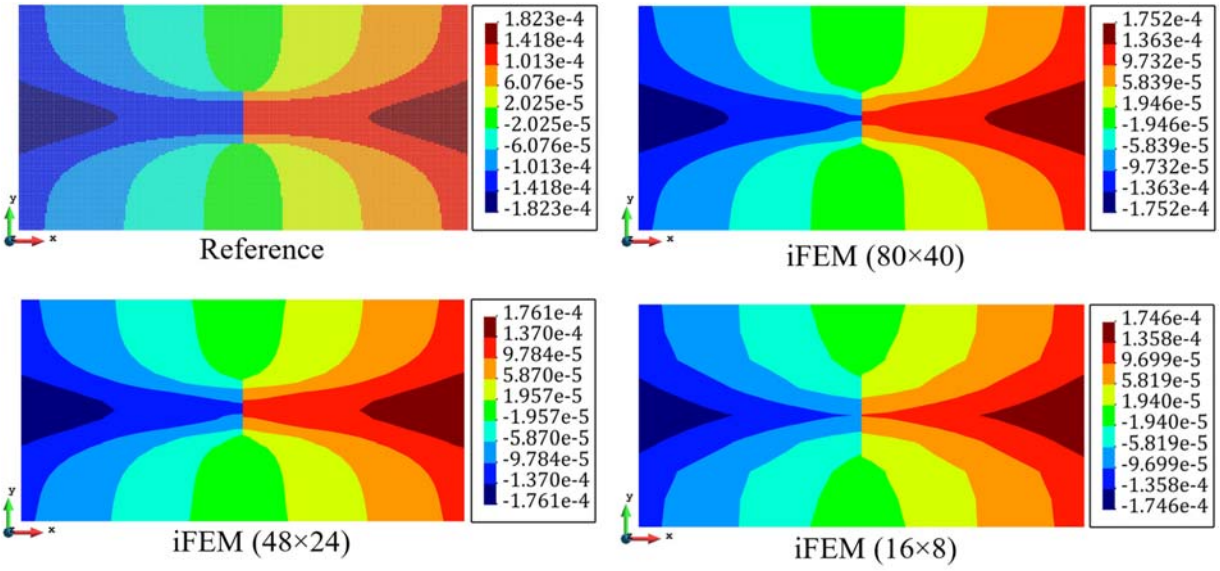

Fig. 13. Contours of u axial deformation at time step, $t = 15$, for unidirectional lamina.

Furthermore, in Fig. 15, the time variations of maximum deformation for each iQS4 model are compared with the reference solution to demonstrate the real-time shape sensing accuracy of the iFEM. According to this comparison, the iFEM results differ slightly from the reference results after the time step of $t = 15$. As indicated above, this difference can be ascribed to damage/crack propagation in the lamina; thus, it would be useful to examine the von Mises critical strains obtained using iFEM displacement results to find the exact diagnostic (high-strain concentration) zone. As a matter of fact, modelling of crack propagation in mesh-based systems is quite tedious

and requires extra operations such as crack tip identification and/or re-meshing. Here, instead of performing these tasks, we first aim to practically diagnose the damage location using the full-field strain data (generated by iFEM analysis) without updating the mesh, and secondly prognose the iFEM-reconstructed deformation data with the iFEM-PD method.

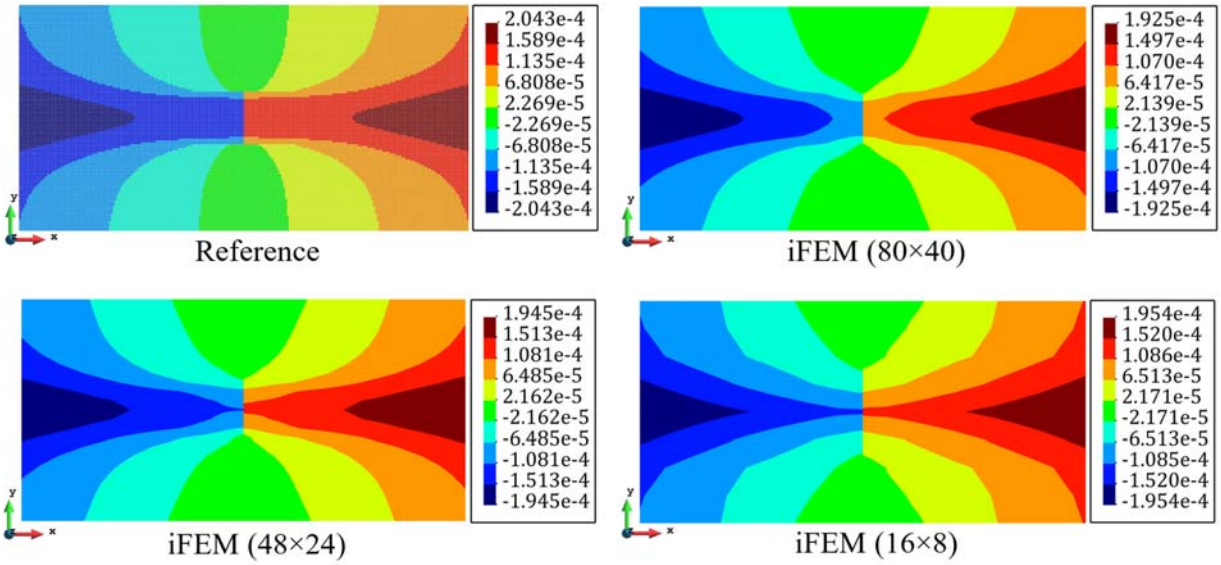

Fig. 14. Contours of u axial deformation at time step, $t = 50$, for unidirectional lamina.

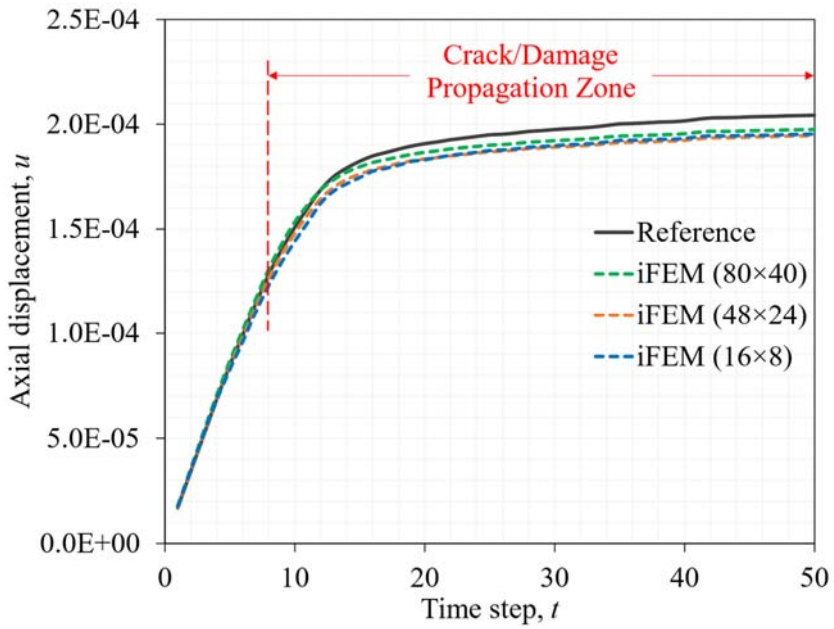

Fig. 15. Time variation of maximum u axial deformation for unidirectional lamina.

Note that it is possible to perform an integrated iFEM-PD analysis at any time step before and immediately after damage increment. In this way, the damaged areas can be defined into the iFEM

mesh according to the direction of the damage for increasing the sensitivity of the deformation results obtained with the current damage paths of the iFEM mesh in each time step. Nevertheless, for practicality of the present iFEM-PD hybrid system, we proceed the detailed damage prognosis of the lamina by neglecting the errors less than 5% in the maximum displacement.

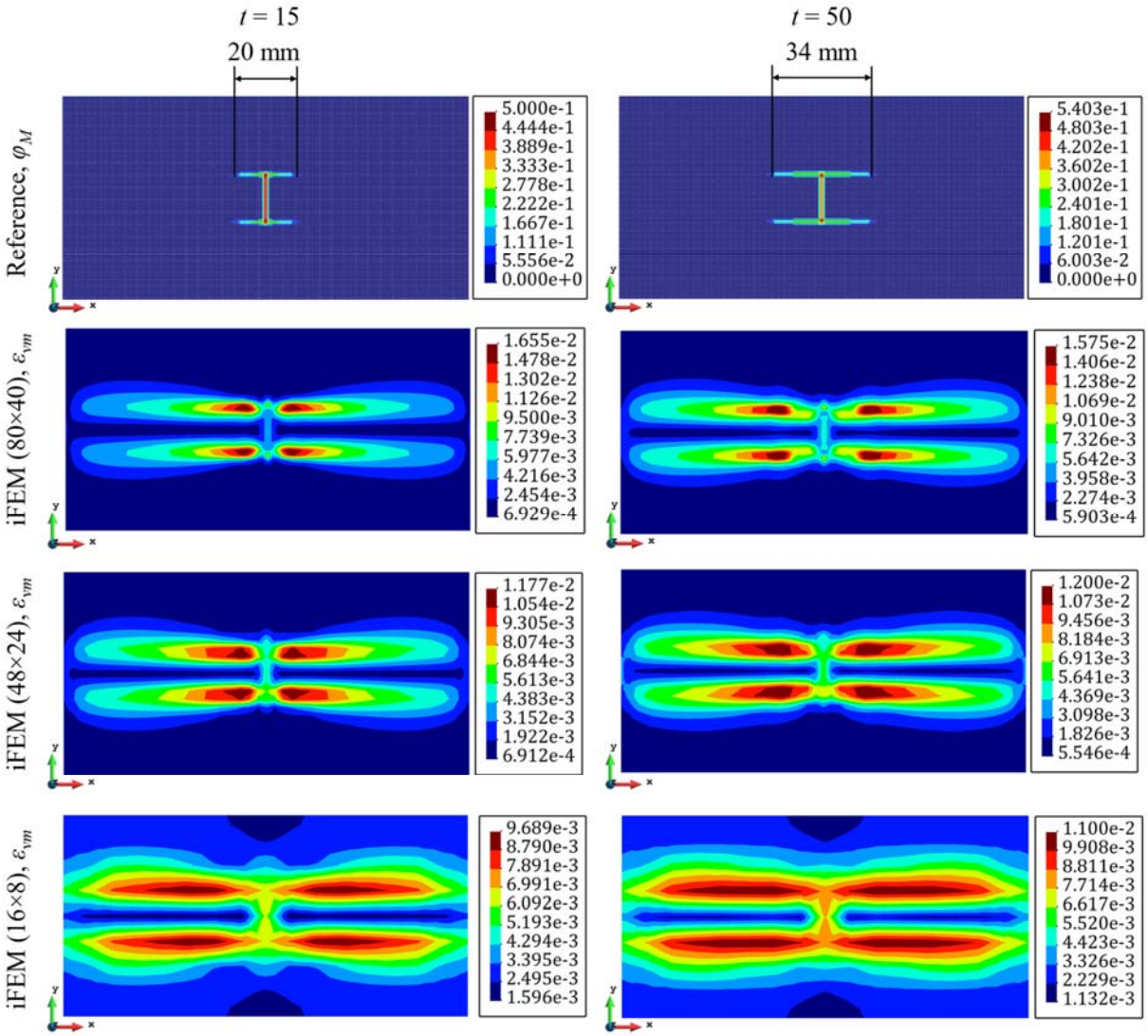

Fig. 16. Damage propagation and von Mises strain contours for unidirectional lamina.

To better observe the crack propagation and damage accumulation in the laminate, matrix damage contours estimated by direct PD analysis are shown in Fig. 16. Lengths of propagated matrix damage/cracks are approximately measured as 20 mm and 34 mm at the time steps of $t = 15$ and $t = 50$, respectively. Similar damage results were obtained in the study of Oterkus and Madenci [97], and in this context, the accuracy of the PD laminate model is demonstrated. In

39

parallel with this damage growth, the equivalent strain values of iFEM analysis are expected to be high at the crack tips and their increment may continue up to a certain length along the x-axis, whereby the damage progress can be examined as presented in Fig. 16. To this end, von Mises strain contours obtained at different time intervals using each iFEM model are compared with the damage evolution contours in Fig. 16.

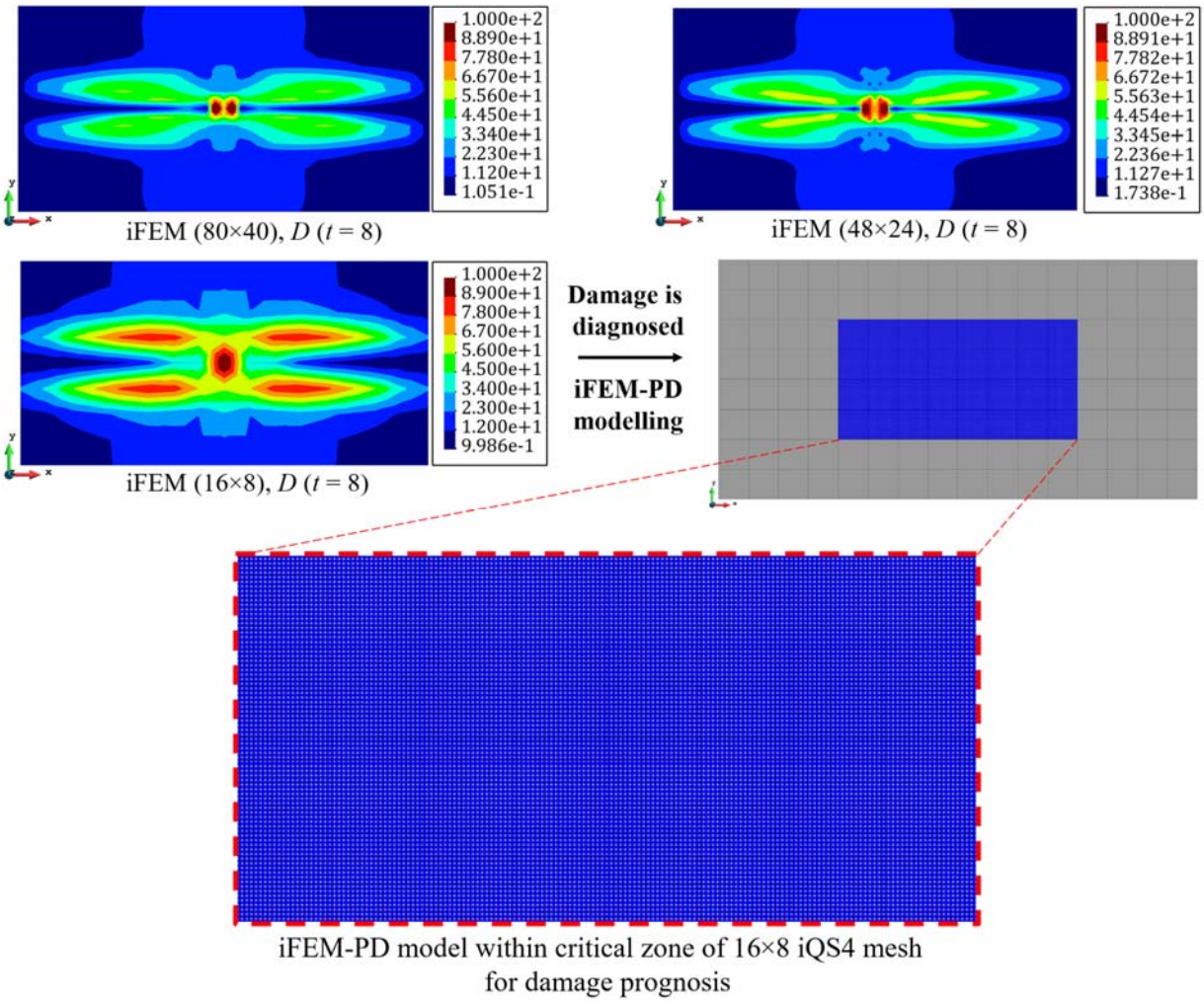

Fig. 17. Damage diagnosis and formation of PD material points in critical von Mises strain regions for unidirectional lamina.

Particularly, the distribution of the red von Mises strain contours indicates that there is a potential damage (high strain region) in the local area at the center of the structure, where may be a failure/crack propagation exist. Employing the von Mises predictions at the onset of crack propagation time step, $t = 8$, for the damage index computation in Eq. (52), the boundary lines of

40

this region can be roughly estimated for each iFEM model as depicted in Fig. 17. Subsequently, PD material points can be placed in these areas as can be seen in the close-up view in Fig. 17. For each iFEM discretization, the diagnosed critical regions dimensions and related uniform particle spacings are listed in Table 2. Note that all these models coincide with the center of the laminate as the damage index is mainly localized therein. Additionally, their horizon size is defined as $\Psi = 3\Delta x$. Through these new models, the PD particles are directly integrated with mechanical response of the iQS4 elements to re-estimate the deformations in this region by imposing the iFEM-predicted deformations to the boundary particles of the PD model. To this end, the deformation values obtained by using the relevant iQS4 models in three different time steps are assigned to the PD material points that limit the critical region, and then an integrated iFEM-PD analysis is performed. In the PD model, the solution of the displacement can be directly calculated for all the material points within the local critical region, and as a result the damage propagation can be consistently analyzed utilizing the PD lamina model at each different time step.

Table 2. Geometrical parameters of the iFEM-PD model in the critical damage zone.

Dimensions, mm	iFEM (80×40)	iFEM (48×24)	iFEM (16×8)
Domain size along x-axis	53.34	50.8	76.2
Domain size along y-axis	26.67	25.4	38.1
PD particle spacing, Δx	0.381	0.3175	0.47625

The crack/damage propagation results predicted by iFEM-PD analysis are shown in Fig. 18 for various mesh resolutions at two critical time steps. These damage estimations can be compared with the reference results (i.e., obtained from forward PD analysis) presented in Fig 16. It can be clearly seen from these damage contours that the dense, medium, and sparse iQS4 models are capable of tracking crack/damage with good precision in accordance with reference solutions. At the time step of $t = 15$, growing cracks length of is roughly estimated as 20 mm on average of the iFEM models, respectively, which agrees well with the reference results shown in Fig. 16. On the other hand, at the last time step, $t = 50$, the iFEM-PD solution predicts about 30 mm length of crack propagation, which differs from its reference solution by %12. Although the exact true

damage size is not perfectly reached at this step, the crack size is fairly estimated even with sparse iFEM-PD model and the direction of the damage progression is accurately estimated. When these results are evaluated in general, it can be concluded that the integrated iFEM-PD model prognoses sufficiently accurate size and direction of damage propagation in composite structures. Hence, this example verifies high precision of iFEM-PD approach for the crack detection and its propagation monitoring for composite structures.

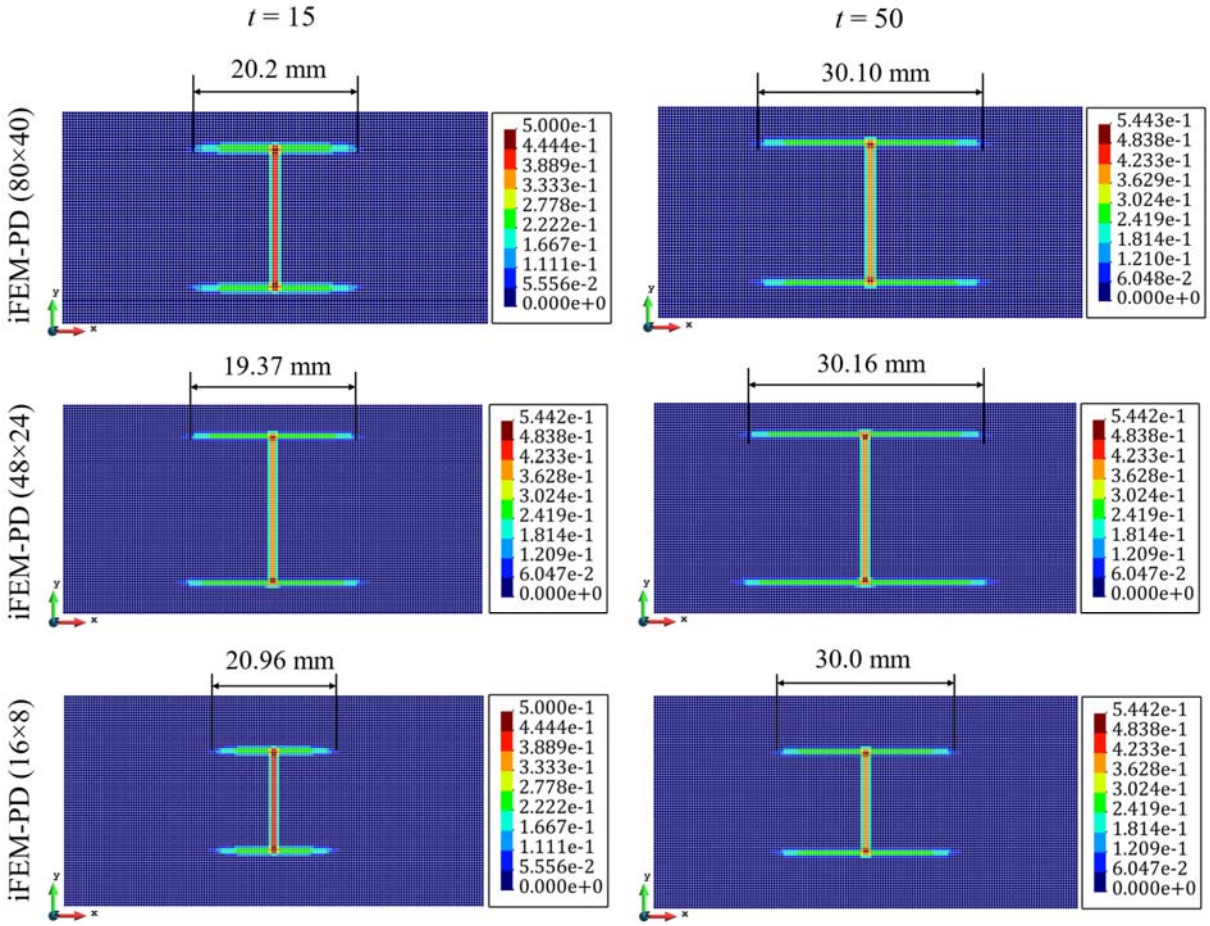

Fig. 18. Crack/damage propagation contours predicted by the hybrid iFEM-PD system for unidirectional lamina.

3.2. Damage detection and crack monitoring of a cross-ply laminate

In this section, the shape sensing and crack propagation monitoring of a three-layer (cross-ply) laminate with fiber angle directions of 0/90/0 is studied under dynamic tensile and bending loads. Similar to the previous example, the length and width of the plate are $L = 152.4$ mm and

42

$W = 76.2$ mm, and each lamina has a thickness of $2h^{(k)} = 0.1651$ mm, resulting in the total thickness of the laminate defined as $2h = 0.4953$ mm. As shown in Fig. 19, a crack with a length of $L/8 = 19.05$ mm, which cut all layers parallel to the y-axis, is located at the center of the laminate.

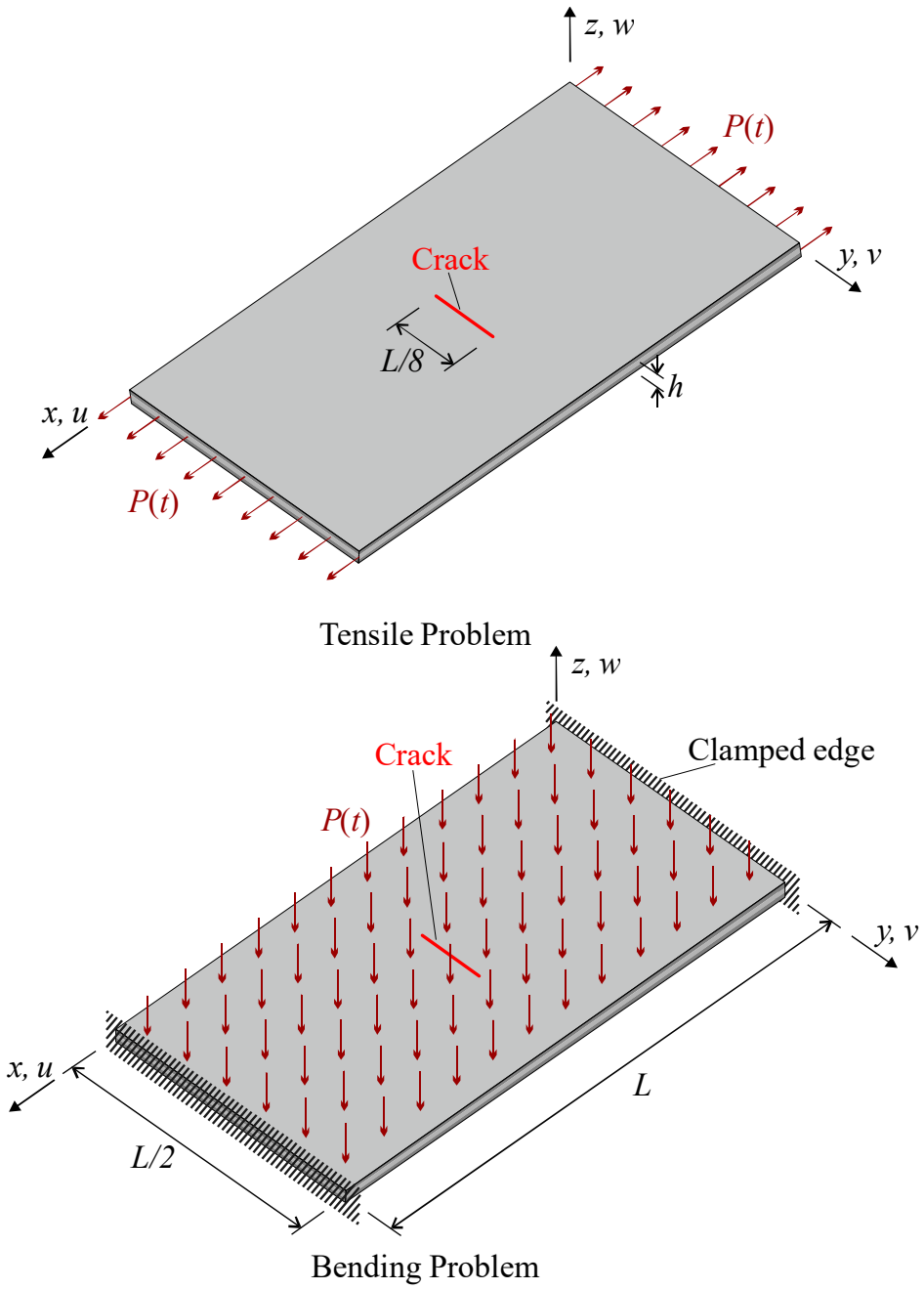

Fig. 19. Geometry and boundary conditions of cracked laminate in tension and bending.

43

The material properties of the lamina (namely, orthotropic carbon-epoxy properties and isotropic epoxy properties) are kept the same as that of lamina described in previous section (see Table 1). To create the three-dimensional PD laminate model of the problem, each lamina is discretized with 120×60 material points, and therefore a uniform discretization with equal spacing of $\Delta x = 1.27$ mm is obtained. Therefore, the laminate model consists of 120×60×3 = 21600 particles in total. The horizon size is chosen as $\Psi = 3\Delta x$ during forward PD and/or iFEM-PD analyses.

First, tensile test of the cracked laminate is simulated using the PD laminate model for a dynamic pressure applied on the left and right surface edges of the laminate as shown in Fig. 19. Here, tensile pressure is distributed equally to all three layers of the laminate. As illustrated in Fig. 20, the tensile pressure varies linearly in time by reaching its maximum value of 302.85 MPa in total time of 0.125 milliseconds. This loading is designated to propagate the crack in the laminate as like a real tensile test condition.

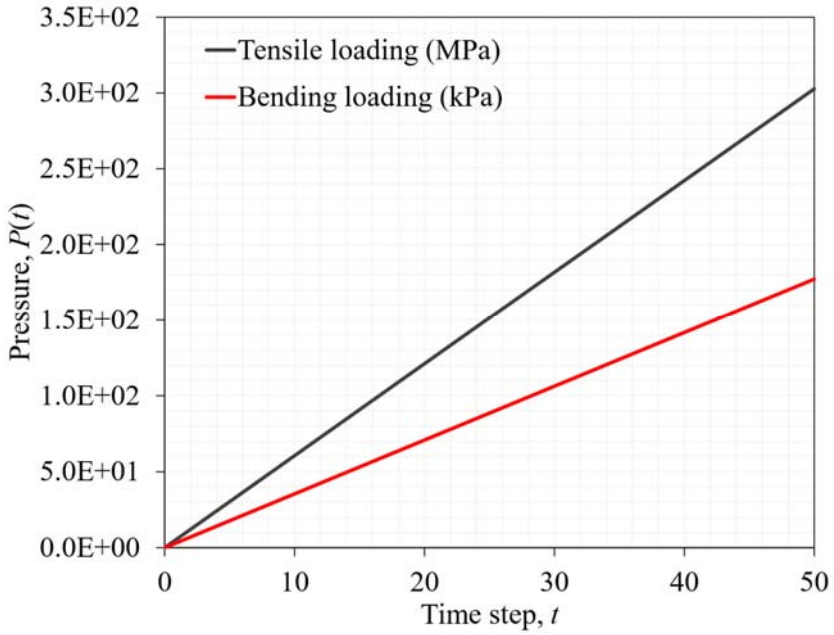

Fig. 20. Dynamic loading conditions applied for the laminate with central crack.

On the other hand, in the bending problem, the crack growth is observed by applying a smaller time-dependent pressure (with a linear increase in time) plotted in Fig. 20. Here, the maximum value of the pressure, 177.17 kPa, is reached at the time of 0.5 milliseconds. The bending pressure is applied on the top surface of the laminate along the negative z axis whereas both the $x = 0$ and

44

$x = L$ surface of the laminate are constrained against three-dimensional deformations as depicted in Fig. 19. The stable explicit time-step size of $\Delta t = 2.5 \times 10^{-8}$ is used for the PD analyses of both problem, which satisfies the stability condition given in Eq. (45). Therefore, the dynamic tensile and bending PD analyses are performed for 5000 and 20000 time steps in total, respectively. However, each analysis is divided into 50 equal time steps to examine the time-dependent variation of the results more effectively. Note that Fig. 20 shows the variation of the loads applied for both tensile and bending problems over these 50 time intervals.

As a result of the direct PD analysis, the reference displacement and damage propagation solutions are generated for each problem described herein. This data is used to verify the accuracy of the integrated iFEM-PD model for both shape sensing and damage assessment of cracked laminates. Besides, using the strain results of forward PD analysis, numerical sensor-strain data that will provide input to iFEM analysis is created. Essentially, this dataset represents strain data collected from sensors at specific locations in a real structure with cracks subjected to either tensile or bending dynamic loads. It should be noted that in a real experimental setup, there is no need to create such a digital (synthetic) data, and it will be sufficient to use the strain readings from real sensors for damage detection with the novel iFEM-PD system. In short, the basic setup in creating the dataset obtained by direct PD analysis is to prove theoretically and numerically that the iFEM-PD system works for laminated structures.

The shape sensing and damage monitoring of the laminate in two different loading conditions, i.e., tensile and bending problem, is performed by using two different iQS4 mesh resolutions: iFEM (40×20) and iFEM (24×12) models. The number of elements is 40 and 20 along the x and y axes of the first model, respectively, while it is equal to 24 and 12 for the relatively sparse solution domain. Besides, a strain sensor is mounted at the center of each iFEM element (see Fig. 11 as representative sensor placement model). The sensor-strain data is collected at 50 different time steps from the direct PD analysis of the laminate. The number of sensors used here may seem to be quite intensive for the experimental setup. However, the main reason for performing dense sensor iFEM analysis is to examine the shape sensing and damage detection capabilities of the iFEM-PD hybrid algorithm in the case of full sensor measurement (all element having sensor, i.e., ideal iFEM solution domain). As explained earlier studies [34-37], the iFEM method does not

require a sensor in every element to perform accurate deformation reconstruction. In this context, the number of sensors can be reduced for making an experimental application.

The maximum axial (u) and transverse (w) displacement results predicted by iFEM models are compared with their reference solutions (generated by direct PD laminate analyses) as shown in Figs. 21-22. Here, the maximum u displacement along x-axis corresponds to the critical deformation of the tensile problem whereas the w displacement along the z-axis is highest deformation of the bending problem. In addition, it should be noted that these real-time solutions are obtained for 50 different strain-data-acquisition (time) steps. As graphed in Figs. 21-22, the deformations reconstructed from sensor data are in very well agreement with their reference solutions for iFEM models. These results also indicate that sparse sensor model (24×12) provides quite close results to those generated by the denser model, except short time intervals during the crack propagation zone. Overall, these comparisons reveal the high accuracy of the iFEM analysis for performing shape sensing of a cracked laminate under either tensile or bending loads.

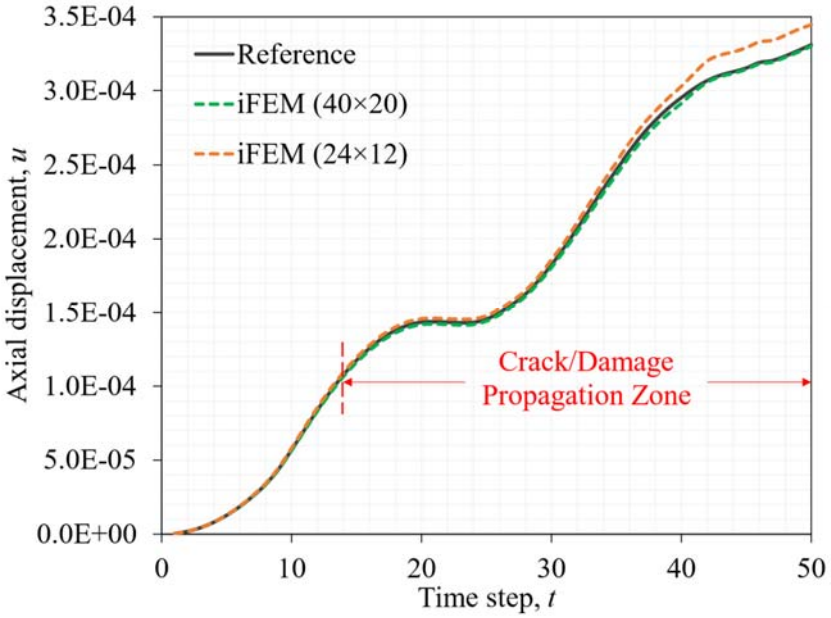

Fig. 21. Comparison of critical displacement results for tension at different time steps.

46

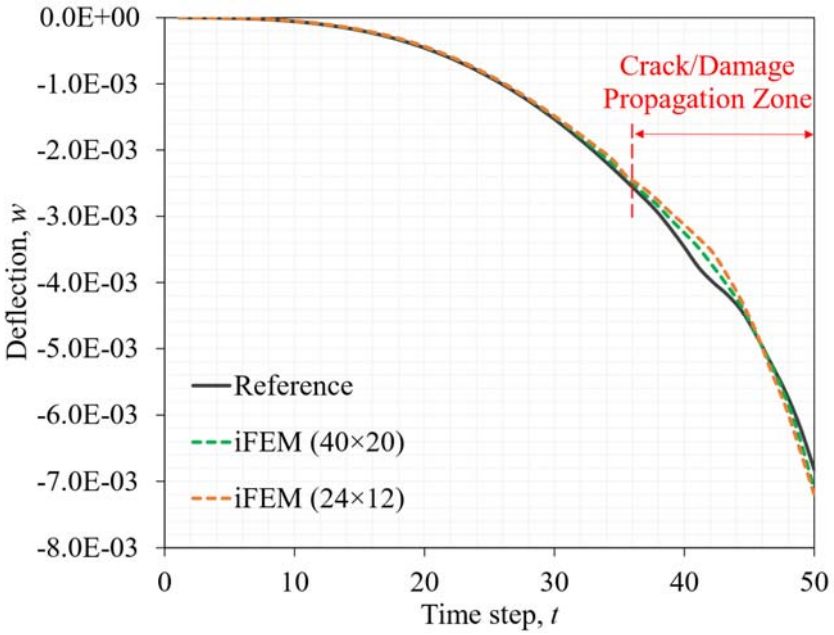

Fig. 22. Comparison of critical displacement results for bending at different time steps.

To evaluate the shape sensing performance of the iFEM algorithm over the full computational domain, total displacement contours are presented everywhere in the laminate at two different time steps as shown in Fig. 23. These time steps, $t = 10,50$, are critically selected out of all time steps to scrutinize the crack propagation within the laminate by using hybrid iFEM-PD model under tensile loading (see time step in Fig. 21 for crack propagation zone). In Fig. 23, iFEM produces very close deformation distributions that are almost indistinguishable from those of the reference PD results in both time steps. The maximum displacement values produced by dense and sparse iFEM models at $t = 10$ time step can be read as 0.05662 mm and 0.05816 mm from Fig. 23, respectively. According to the reference result (0.05694 mm), the percent errors pertaining to these models are around 0.56% and 2.14% only. With the similar calculation method at $t = 50$ time step, the percentage maximum displacement errors are found as 0.24% and 4.1% for the dense and sparse sensor placement models. These small differences between iFEM and reference maximum displacement demonstrate the high accuracy iFEM models for deformation monitoring of a cracked laminate under tensile loading. While there are very low error rates for both sensor placement models, it is seen that the margin of error is slightly higher when the solution domain becomes sparser. This can be only attributed to a natural effect of discretization resolution on the result accuracy.

47

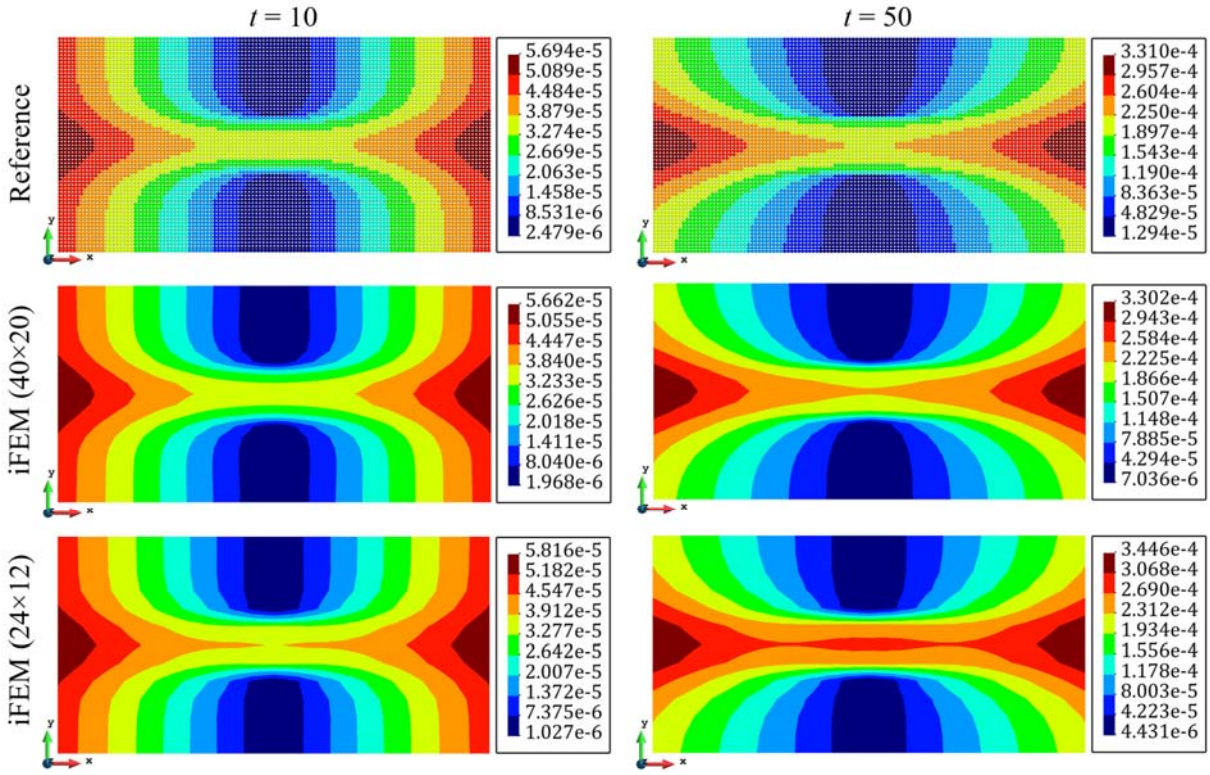

Fig. 23. Total displacement contours of the laminate under tensile loads at different time steps.

Like the axial deformation monitoring of the laminate, the various displacement contours estimated for the bending case are shown separately for critical strain-data-acquisition steps in Fig. 24-25. As can be seen from Fig. 22 that these steps, $t = 40, 45, 50$, encounter the crack propagation zone of the laminate under bending loads. In Fig. 24, the total displacement contours obtained using the iFEM (40×20) and (24×12) models have very close distribution to that of reference PD result almost anywhere in the laminate. To assess the accuracy of the predicted displacements, the maximum bending displacements at $t = 40$ time step, i.e., 3.528 mm (reference), 3.435 mm (iFEM-40×20), 3.349 mm (iFEM-24×12), can be considered as illustrated in Fig. 24. Accordingly, the percent difference between iFEM and reference PD solution is only 2.63% and 5.07%. Besides, for the next time step, $t = 45$, displacement prediction accuracy of iFEM (40×20) and (24×12) models are computed as 95.8% and 93.5%, in the given order. Moreover, the u, v, w displacement contours produced by the iFEM (24×12) model in the last time step ($t = 50$) of shape-sensing analysis are compared with their reference solutions in Fig. 25. The maximum values of these displacement components are predicted as $u_{\max} = 0.392$ mm, $v_{\max} = 0.103$ mm, and $w_{\max} = 7.34$

48

mm by iFEM analysis whereas they are obtained as $u_{\max} = 0.335$ mm, $v_{\max} = 0.112$ mm, and $w_{\max} = 7.53$ mm from direct PD analysis. Expectedly, the largest displacement value belongs to the w displacement in the z direction due to bending state of the laminate. Remarkably, this fact is well estimated by the iFEM methodology even if there exist a growing crack within the laminate. Furthermore, the error margins for the $w_{\max}$ predictions remain in small values (being less than 2.6%), and the u, v, w deformation contours produced by reference PD and iFEM analysis are almost indistinguishable from each other in every region of the laminate as presented in Fig 25. Hence, these results validate the high accuracy of iFEM methodology in terms of achieving full-field displacement solution as compared to the PD reference results.

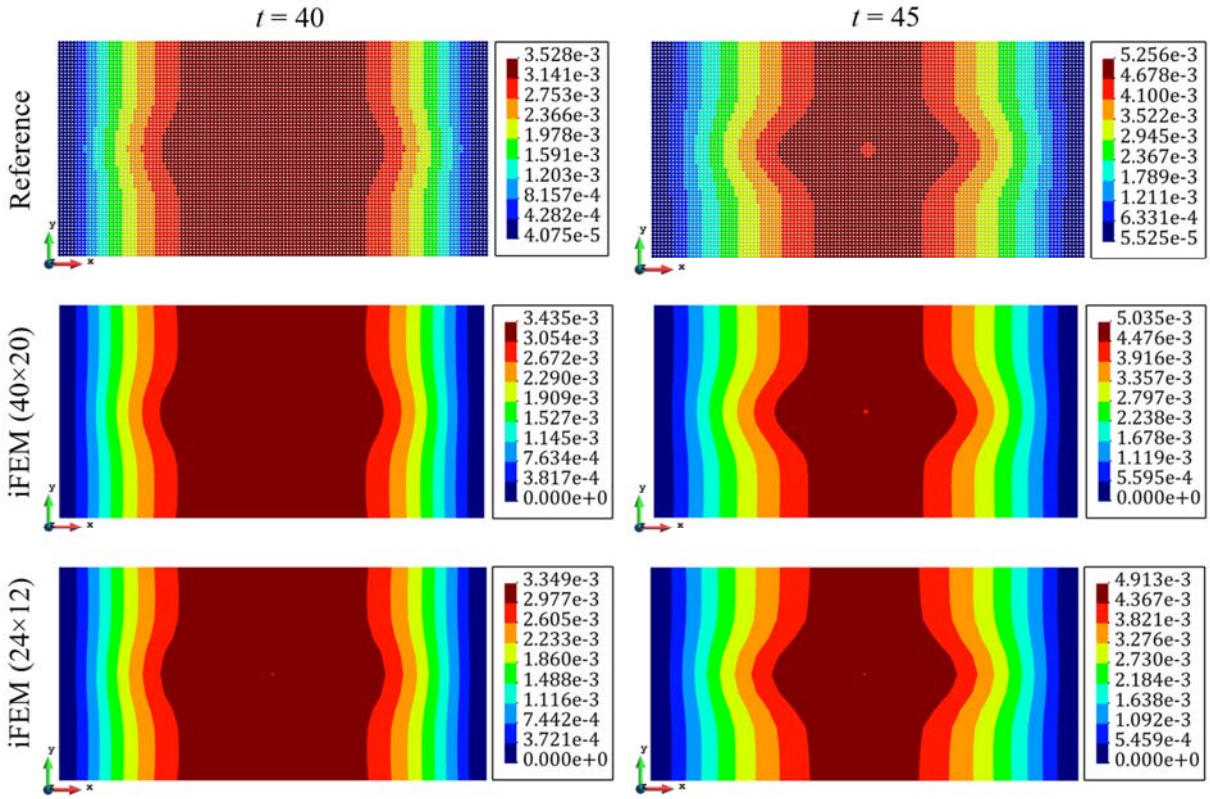

Fig. 24. Total displacement contours of the laminate under bending loads at different time steps.

49

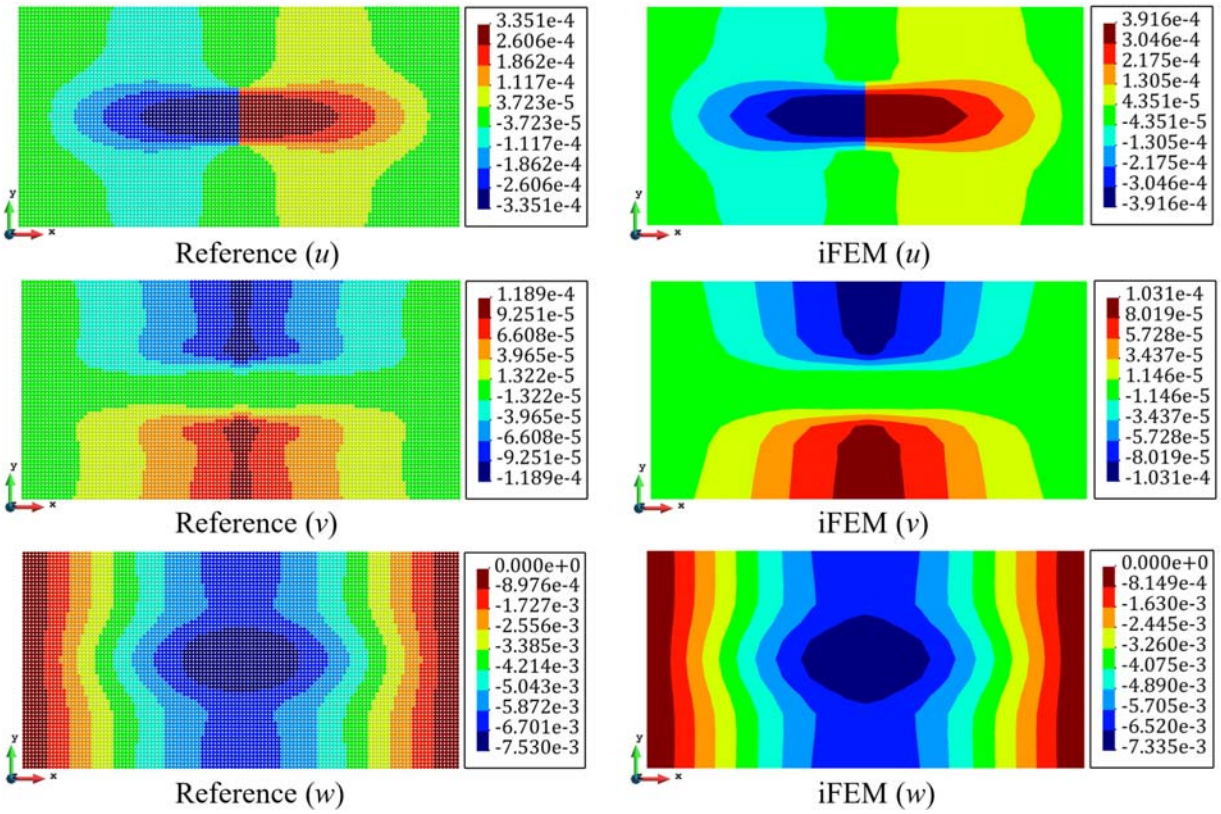

Fig. 25. Axial, lateral, and transverse displacement contours of the laminate under bending loads at the last time step, $t = 50$.

The full field displacement solution estimated by iFEM analysis can be utilized to compute the von Mises strains within the laminate for performing full-field strain sensing in both cases of tensile and bending conditions. It should be noted that damage prognosis and/or crack propagation monitoring may not be analyzed directly over the von Mises strain contours. Nevertheless, the von Mises strain predictions can play an important role to detect a critical/potential damage region for detailed prognosis of damage accumulation therein based on the hybrid iFEM-PD system. Here, the critical region is classified according to the high von Mises strains that exceed large strain values of 9000-10000 μm/m.

For the tensile problem, the von Mises strains calculated by iFEM at $t = 30, 50$ time steps are illustrated together with the matrix damage contours obtained by the PD code, representing the reference solution in Fig. 26. Here, one can clearly observe hot spot regions where the von Mises strain value exceeding 10000 μm/m match with the damage zones in different time steps. Such comparison can enable a damage-diagnosis criterion between von Mises strain values and

damage/crack propagation in the laminate. More specifically, the maximum strain value is approximately 14460 μm/m at $t = 30$ time step while the PD results confirms that the damage starts to propagate within the laminate. Remarkably, at last time step of the problem, the strain level increases up to 30000 μm/m as such drawing the boundaries of the highly susceptible failure area.

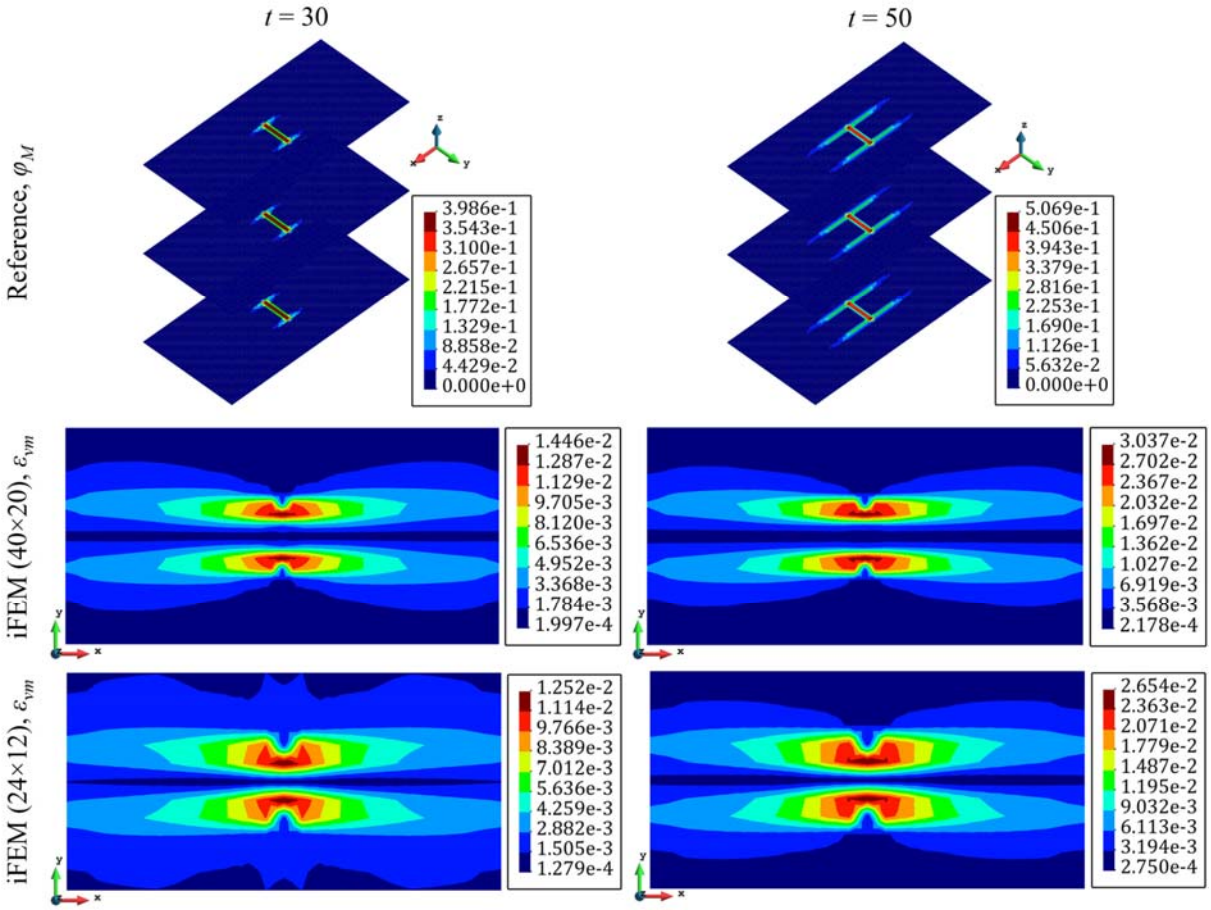

Fig. 26. Comparison of the von Mises strain contours obtained by iFEM with the PD damage results at different time steps in the tensile loading of the laminate.

Additionally, the comparison between PD damage and iFEM von Mises strain contours are shown in Fig. 27 for the bending problem. These contours clarify how the maximum values of von Mises strain over time can be used to diagnose the damage propagation around the crack. For instance, maximum strains for iFEM (40×20) and (24×12) models reach 26840 and 28260 μm/m at $t = 45$ time step, respectively. At this stage, when the PD damage contours are examined, it is obvious that the damage have progressed within the laminate. Marching to the last time step, $t = 50$

51

, as illustrated in Fig. 27, the iFEM von Mises strains increase exponentially up to the maximum value of 56110 μm/m whereas the matrix damage grows rapidly from the tip of the crack towards clamped edges.

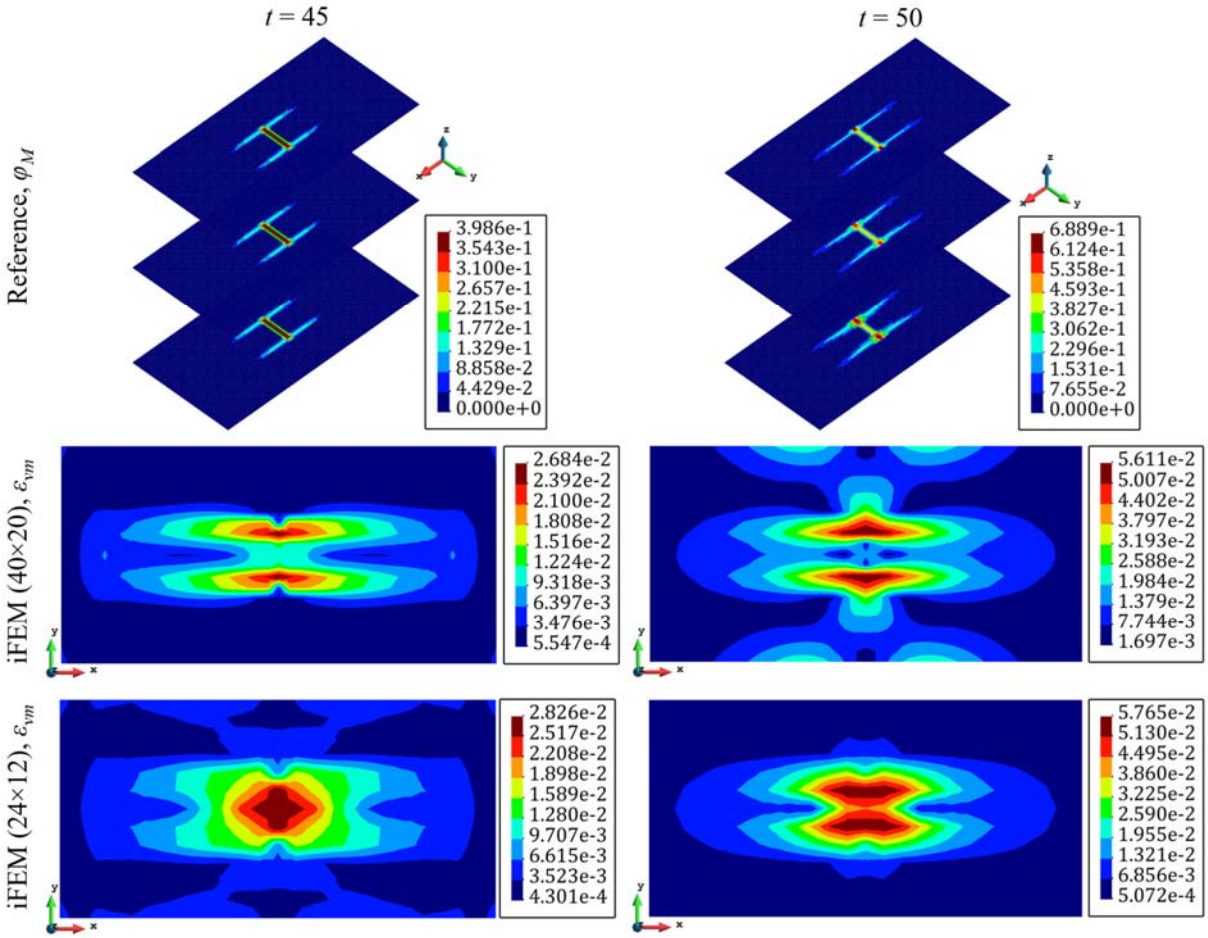

Fig. 27. Comparison of von Mises strain contours obtained by iFEM with PD damage results at different time steps in the bending loading of the laminate.

The damage indices are calculated to define the critical damage zone for both mesh resolutions as depicted in Fig. 28. To this end, time steps of $t = 14$ and $t = 36$ corresponding to the onset of crack propagation is chosen for tensile and bending problems, in the given order. The relative damages are diagnosed and localized at these specific time steps for evaluating damage prognosis of the laminate through iFEM-PD hybrid algorithm. Comparing these contours with Figs. 26-27, the strain values surpassing 10000 μm/m over the critical damaged zone confirm that the damage has started to propagate in this period for the iFEM models. In other words, these critical zones conform the high von Mises strain locations such that they are susceptible to any damage

occurrence, thus the development of the damage in this area is examined using the PD laminate model. For this purpose, as shown in Fig. 28, blue PD model is first generated in the critical zone with the particle discretization of 60×30 for both tensile and bending conditions of the laminate. Then, the displacement results obtained from the iFEM analysis are used as the input in the PD laminate code. Namely, the displacements on the red lines of the critical region in Fig. 28 are determined from the iFEM analysis and subsequently used as boundary conditions in the PD analysis. After that, iFEM-PD analyses of both loading problems are performed, and the matrix damage results are finally evaluated as presented in Figs. 29-30.

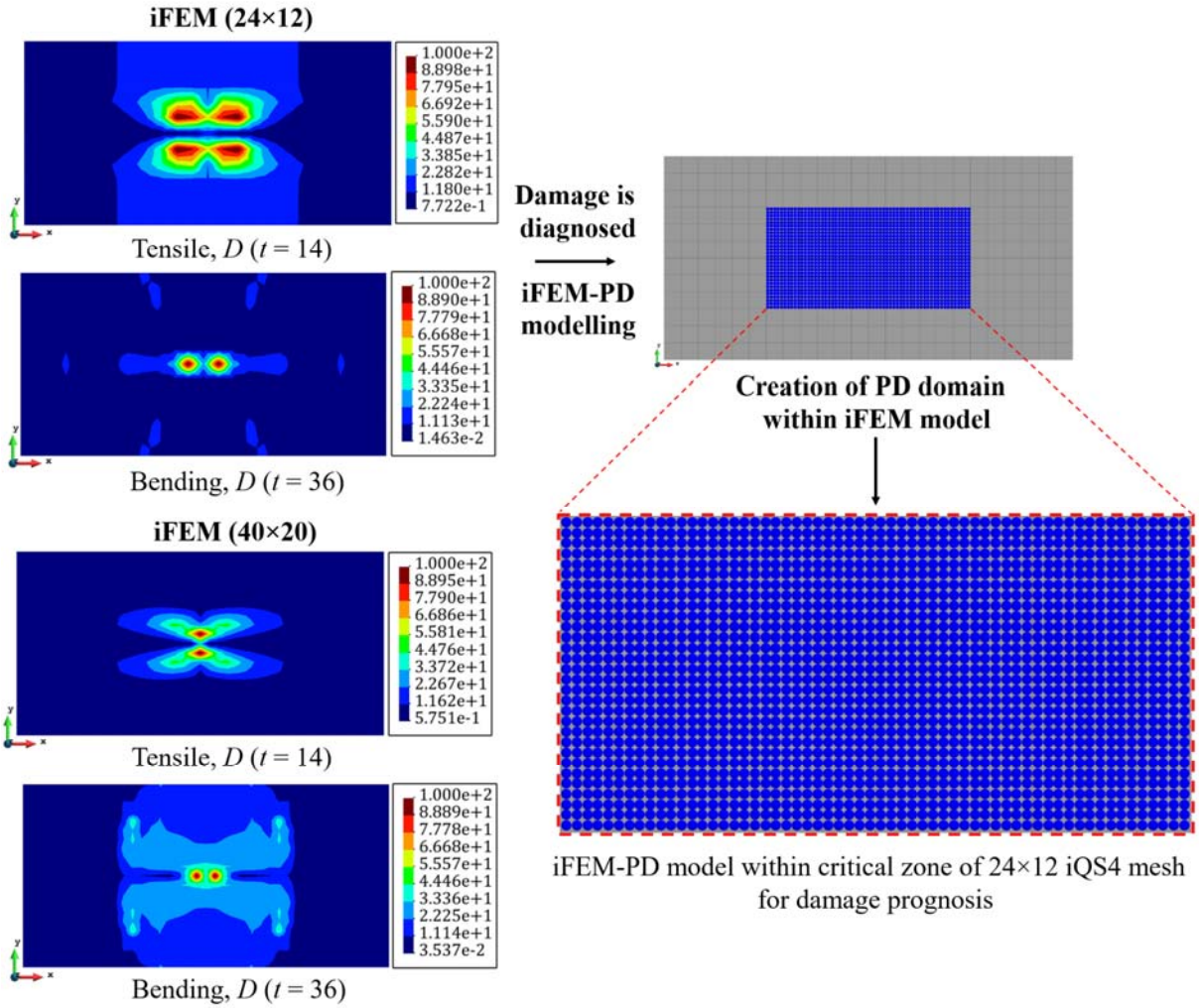

Figure 28. Formation of PD material points in critical von Mises strain zones for both tensile and bending problem of the laminate.

53

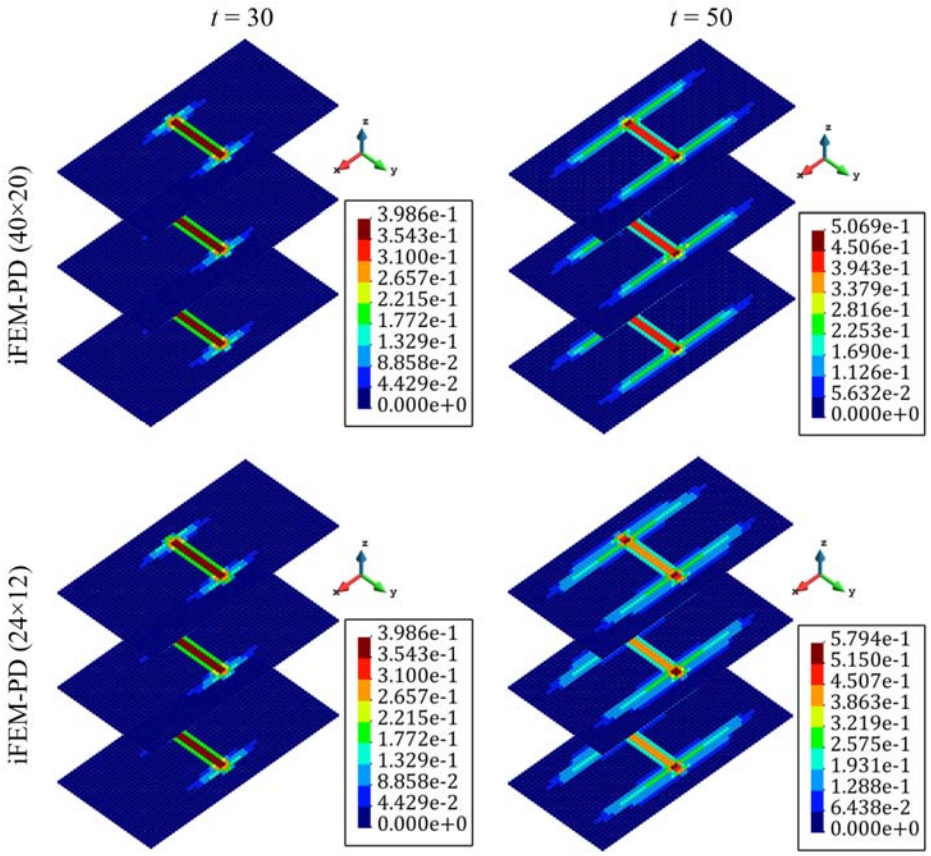

Fig. 29. iFEM-PD damage predictions in critical area of laminate subjected to tensile loading: damage prognosis.

As an output of the iFEM-PD hybrid system for the tensile problem, the damage contours obtained by the PD analysis are presented on the critical high strain regions of two different iFEM-iFEM models at different time steps in Fig. 29. Note that the results corresponding to the $t = 30, 50$ time steps are monitored herein as they are the most crucial steps of the damage accumulation. To validate the accuracy of the iFEM-PD results in Fig. 29, they can be compared with the reference solution generated by direct PD analysis illustrated in Fig. 26 at the associated time steps. From such a comparison, it will be observed that damage contours prognosed by the coupled iFEM-PD analysis are in very good agreement with their reference matrix damage solutions at sequential strain-data-acquisition steps. Besides, the damage magnitudes for the iFEM-PD models are almost identical to those estimated by direct PD analysis. These comparisons clearly verify the high accuracy of coupled iFEM-PD system for prognosis of damage/crack propagation in laminated structures subjected to tensile loads by utilizing only a network of strain sensors. In summary, it

can be concluded that the iFEM-PD methodology merges the merits of iFEM and PD algorithms to monitor crack propagation in composite laminates in detail.

In addition to the damage-prognosis comparisons made for the tensile problem, damage accumulation results produced by the coupled iFEM-PD algorithm are shown in Fig. 30 for the critical time steps of $t = 45, 50$ in the case of bending problem. Like to the tensile problem comparison, it is possible to compare these damage contours obtained in the high-strain-region with their reference solutions illustrated in Fig. 27. This assessment reveals that the direction and shape of the matrix damage growth in the layers of the laminate are almost identically estimated by the iFEM-PD hybrid system to those of direct PD results. Namely, iFEM-PD analysis can forecast a highly precise crack paths that are very similar to the reference results shown in Figs. 27 and 30.

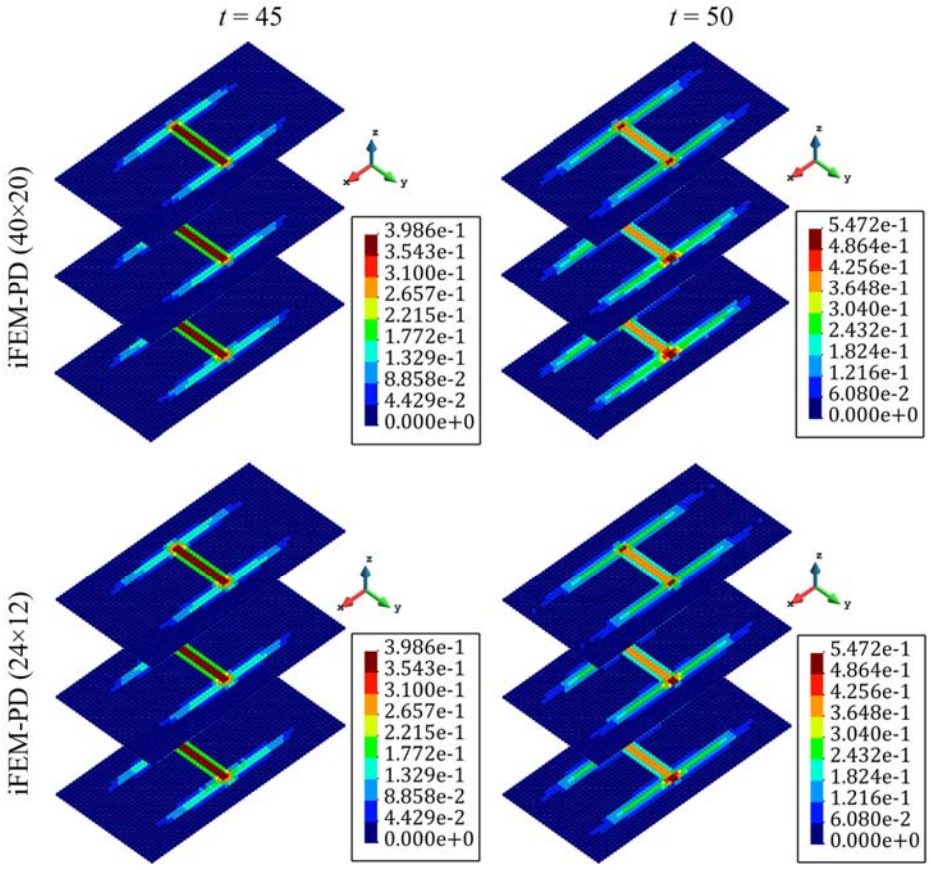

Fig. 30. iFEM-PD damage predictions in critical area of laminate subjected to bending loading: damage prognosis.

55

In fact, both iFEM-PD (40×20) and (24×12) models generates almost the same damage contours in the same local regions shown in Fig. 27 at the $t = 45$ time steps. Yet it may be important to notice that the amount of similarity in the damage contours is higher when the finer iFEM-PD model is used at $t = 50$. Regarding the magnitudes of the damage accumulations, both iFEM-PD models predict the same result of the PD solution at the time step of $t = 45$. However, for last step of the bending problem, $t = 50$, iFEM-PD analysis slightly underestimates the amount of the maximum damage at the crack tip in the bottom ply. Nevertheless, except for this small region, the spatial distributions of matrix damage values produced in iFEM-PD analyses are in excellent agreement with their reference PD solutions over the whole laminate. Hence, the iFEM-PD hybrid structural health monitoring system can accurately prognose the damage/crack propagation in laminates exposed to bending loads using in-situ sensor-strain data only.

3.3. Experimental study for crack monitoring of a woven laminate

For experimental validation of the present approach, woven (twill fabric) carbon fiber reinforced composite plates with a central crack are prepared as shown in Fig. 31. The dimensions of the rectangular tensile specimens are 200×75 mm^2 and glass fiber reinforced laminates with the size of 25×75 mm^2 are adhered as tab at both ends of the specimens as illustrated in Fig. 31(a). Thus, the gauge length of each tensile sample becomes 150 mm after tabbing (Fig. 31b). For each specimen, a central crack with the length of 18.7 mm is cut using water jet. During the mechanical tests, the in situ full-field deformation and strain data are collected by DIC system. To this end, as depicted in Fig. 31(b), a random speckle pattern is applied on one side of the samples and a detectable high contrast region is created for the DIC camera. Here, the post-processing of the DIC images is accomplished with GOM Correlate software using facet and step sizes as 25 and 19 pixels, respectively. A coarse and sparse sensor placement iFEM/iQS4 model of the specimen (conforming the 150×75 mm^2 gauge/DIC region) is generated as illustrated in Fig. 31(b), where the discrete strain sensors are positioned at the center of the iQS4 elements having sensors. In this sparse model, only 40% of the iQS4 elements are fed with in-situ data, others have no experimental input for shape sensing analysis. Note that the weighting coefficients for membrane, bending and transverse-shear strains of the iQS4 elements with no sensor are set to 10^{-4} to maintain the strain connectivity between the elements having sensors. All three specimens are sequentially fixed to the universal test machine as depicted in Fig. 32(a), the load is introduced at a constant speed of

2mm/min, and DIC system is active for each sample during the tensile tests. Similar force-displacement plots are observed for the tested specimens in Fig. 32(b), and almost identical fracture patterns of the samples are examined with the naked eye as shown in Fig. 31(a), which prove the accuracy and repeatability of the performed experimental tests. More details of the preparation of the test sample and experimental setup are given in our recent study [107].

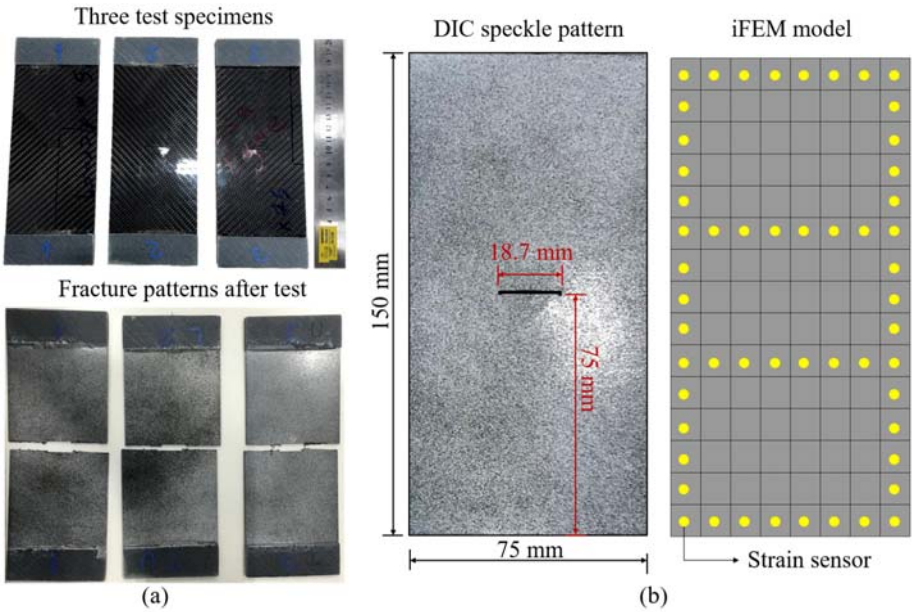

Fig. 31. (a) Three specimens (with the size of 200×75) before and after tensile test and (b) geometry, speckle pattern and sensor placement of the specimens.

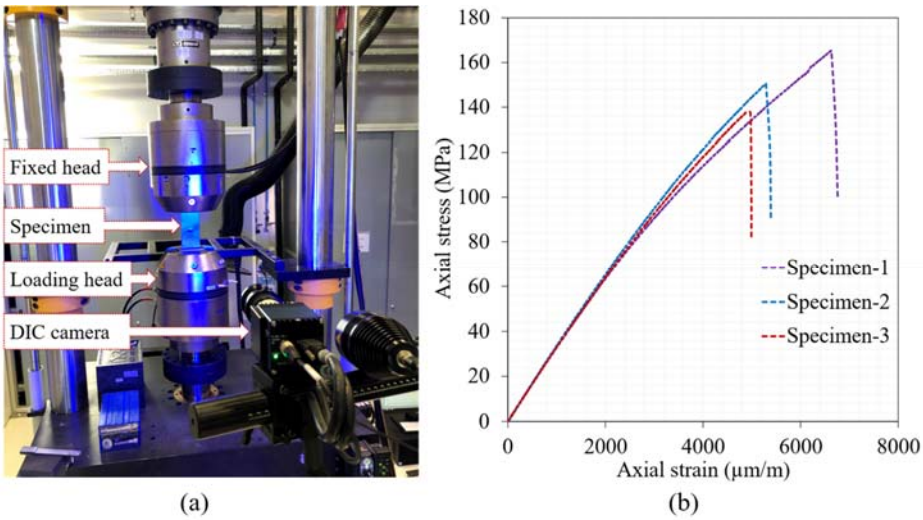

Fig. 32. (a) Tensile test and DIC system set up and (b) strain-stress curve obtained from three specimen during the test.

57

The discrete real-time strain data obtained from sensors are the main input for the iFEM model to reconstruct the full-field displacements. Here, the continuous DIC strain data is used to represent collected data from the resistive strain gauges and/or FBG sensors at various locations on the surface of the test specimens. Namely, as input to iFEM simulation, the discrete strains at the sparse configuration in Fig. 31(b), i.e., corresponding to the yellow circles, are sampled from the continuous DIC strain information at each load increment during the tensile tests. It is also important to know that none of the iFEM models of the specimens considers the presence of crack in the laminate. Thus, no *'a priori'* data regarding the discontinuity are provided to the iFEM model. Performing the iFEM analysis at pre-failure, failure, and post-failure moments, the full-field displacements are reconstructed and subsequently compared with the continuous deformation results of DIC system as shown in Fig. 33. According to the variations of total displacement contours, excellent agreement between the DIC and iFEM results is apparent despite no information of crack in iFEM analysis.

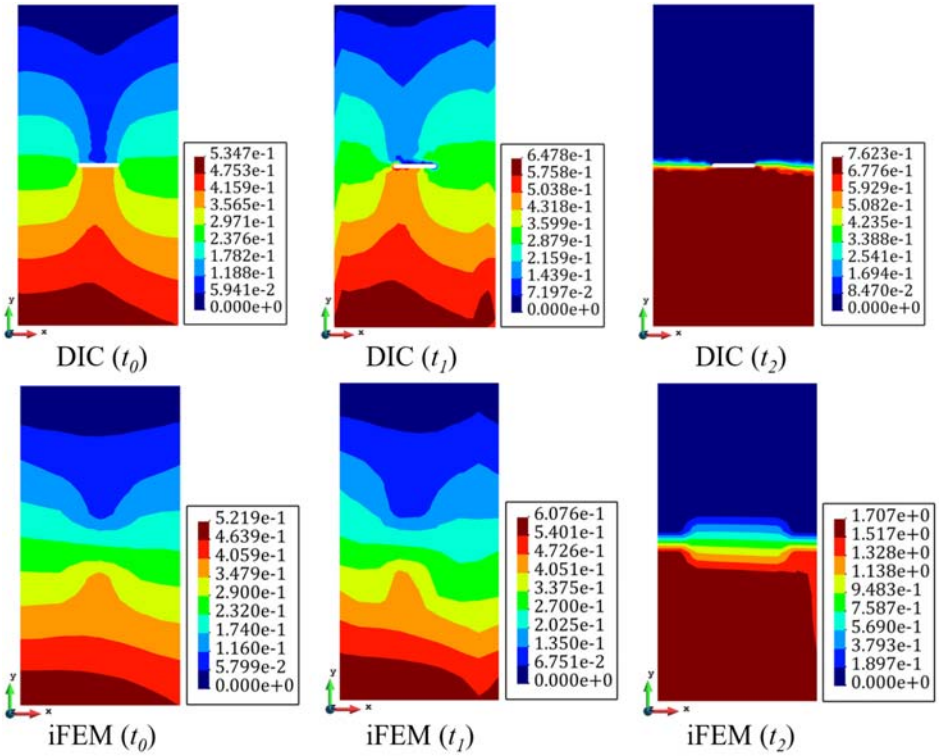

Fig. 33. Comparison of full-field total displacements, u_T, predicted by iFEM and DIC analyses at t_0 (pre-failure), t_1 (failure), t_2 (post-failure) load steps.

58

At the t_0 (pre-failure) and t_1 (failure) steps, the displacement contours of iFEM and DIC results are almost indistinguishable from each other, and percent different maximum displacements are calculated as, 2.4% and 6.2%, respectively. On the other hand, at the t_2 (post-failure) step, the contours of the iFEM total displacement matches with the those of DIC, except details of the color pattern in the crack propagation region at the center of the specimen. Further, the magnitude of the maximum deformation is not predicted accurately with iFEM as compared to the DIC simulation. This important implication can be attributed that iFEM has no initial knowledge of central crack. Nonetheless, iFEM provides an intuition of crack propagation path with weak fluctuations in the composite specimens. To have a detailed view of the crack by zooming in its pattern, one can utilize iFEM-PD methodology.

Even though the iFEM method itself does not provide detailed crack propagation output, it enables detection of the critical damaged region as well as the crack length, on which PD material points can be populated to run coupled iFEM-PD analysis. For this reason, von Mises strain maps monitored via iFEM analysis is leveraged to identify the exact damage position and its near-field regions within the composite specimen as shown in Fig. 34. In this figure, the maximum von Mises strain is found as 7653 μm/m at pre-failure stage. Although no previous information about discontinuities is provided to the iFEM methodology, the high stain gradient regions indicate significant damage presence at the middle of the laminate. Note that sudden variation of continuous von Mises strain maps were examined at failure moment, indicating growth of damage in horizontal direction [107]. According to these results, the damaged region is detected via iFEM methodology, and a horizontal crack is designated at the center of the plate (in region of von Mises strains exceeding 6000 μm/m) as shown in Fig. 34.

Moreover, the peridynamic material points are populated in the near-field of critical damage/crack region, constituting the iFEM-PD model as sketched clearly in Fig. 34. For the PD model, the number of material points along x and y directions are 120 and 144, respectively. Thus, the discretization size, Δx, is equal to 0.625 mm. The horizon size is chosen as $\Psi = 3\Delta x$. Moreover, according to von Mises strain results, the predicted crack with the size of 18.75 mm is placed to the center of iFEM-PD model. Since the woven composite plate demonstrates similar material properties along the horizontal and vertical directions, it is assumed that it satisfies transversely isotropic symmetry condition. Hence, the orthogonal xy-plane has the isotropic

symmetry behavior. The reason of this is that the elastic moduli along x and y directions are equal for woven composites [70-71, 107], where the details of the present material properties are provided.

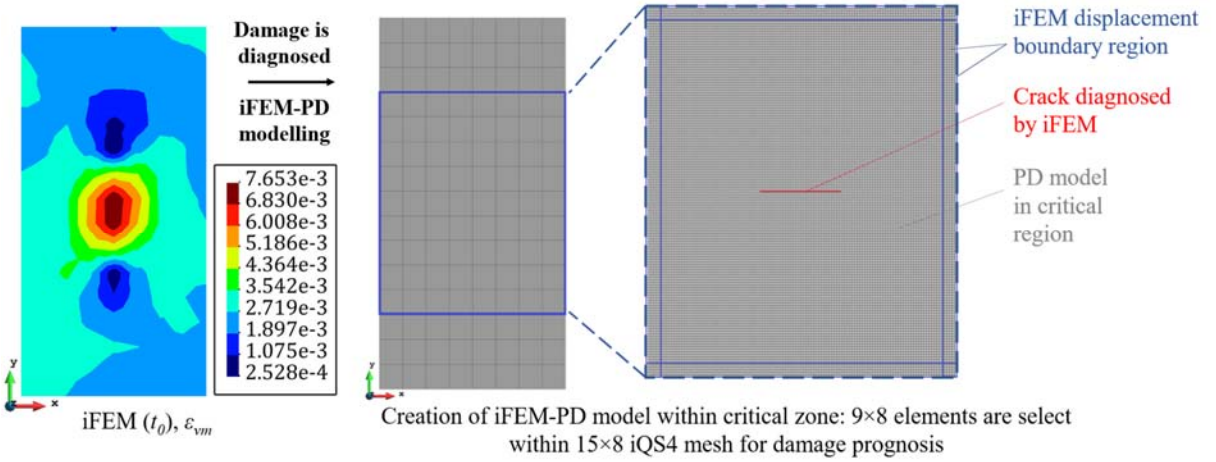

Fig. 34. Damage detection using von Mises strains predicted by iFEM and formation of PD material points in critical strain zones for coupled iFEM-PD analysis.

Subsequently, the full-field iFEM displacements are applied as boundary conditions to the peridynamic model in the boundary region, chosen as $5\Delta x$, as depicted in Fig. 34. The deformation results obtained from iFEM at pre-failure, failure and post-failure stages are imposed as boundary conditions to peridynamic analysis. Note that the ADR method is adopted to solve the PD model quasi-statically for each failure stage. The damage/crack growth and displacement results obtained from iFEM-PD simulations are compared with the raw images taken via DIC cameras as shown in Fig. 35 at pre-failure, failure, and post-failure stages.

According to DIC images at failure states, the composite specimen is split into two parts which present almost no deformations above and below to the pre-crack region, which is confirmed by the displacement results of iFEM-PD approach. As seen in Fig. 35, the maximum displacement obtained from horizontal boundary of the critical region at pre-failure stage is estimated as 0.41 mm using iFEM-PD model, which is also observed as 0.42 mm from DIC measurements in Fig. 33. Moreover, the maximum displacements at failure and post-failure stages are predicted as 0.49 mm and 0.68 mm, respectively, in the iFEM-PD analysis. Their counterparts are observed as 0.51 mm and 0.68 mm from DIC displacement contours in Fig. 33. Hence, the magnitude of the deformations (max ~0.7 mm) at the all-failure stage is minuscule as compared to the gauge length

60

of the specimen, 150 mm. Further, displacement contours produced by the iFEM-PD hybrid methodology are in very good agreement with those of DIC results.

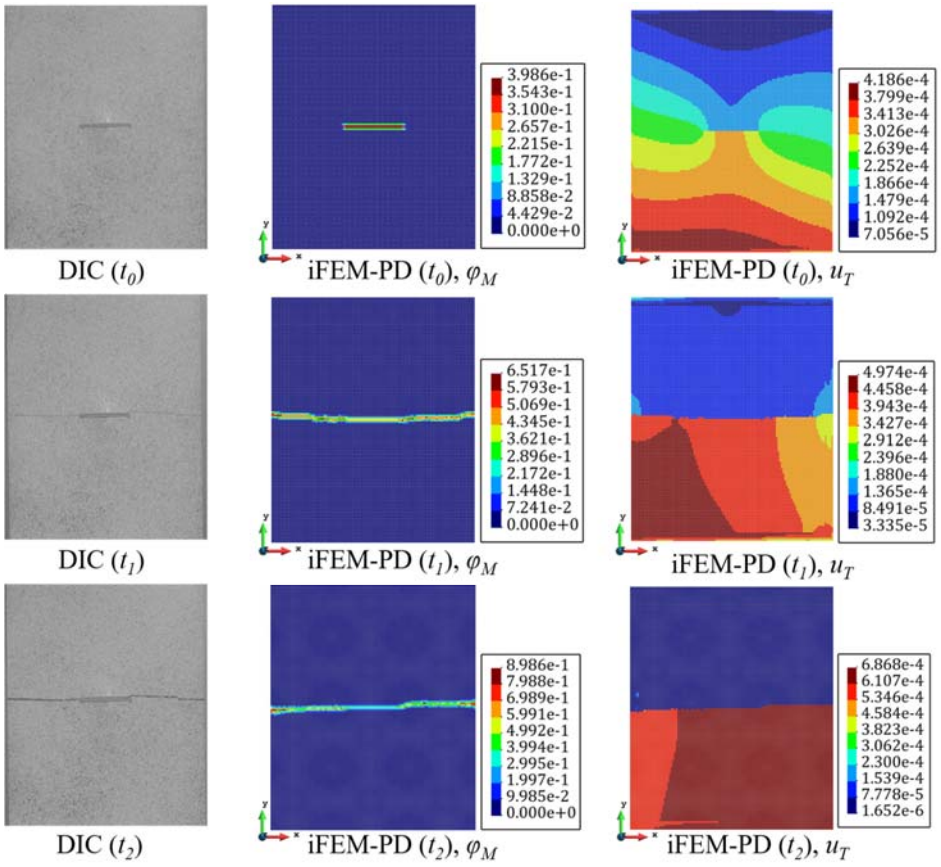

Fig. 35. Comparison of DIC crack propagation path and iFEM-PD damage (φ_M) and total displacement (u_T) predictions at t_0 (pre-failure), t_1 (failure), t_2 (post-failure) load steps within the critical zone of the laminate.

Fig. 35 also presents peridynamic damage results in the laminated plate. These contours clearly demonstrate mode-I crack propagation path parallel to the horizontal edges of plate. The maximum damage value is found as ~0.4 at pre-failure stage whereas it is ~0.65 at failure stage. This value increases up to ~0.9 when the crack reached the boundaries at the post-failure stage. It is obvious that the plate is split into two parts at this stage. Accordingly, the damage/crack propagation path estimated by iFEM-PD almost perfectly coincides with those of DIC system. Hence, it can be concluded that the high accuracy of the iFEM-PD methodology is experimentally proved for both shape sensing and crack propagation monitoring in composite structures.

61

4. Conclusions

In this research effort, a coupled iFEM-PD system is developed for real-time displacement monitoring and the damage growth diagnosis/prognosis of three-dimensional laminate structures by using only in situ strains (discrete experimental data) collected from sensors. The mathematical models of iFEM and PD approaches are respectively established for a quadrilateral inverse-shell element (iQS4) and bond-based nonlocal models of lamina/laminate, and their novel coupling is algorithmically scrutinized for specific computer implementation. The new SHM formulation developed herein is applicable to crack monitoring of a general class of plate structures made of laminated composite or brittle isotropic materials.

The hybrid iFEM-PD system is numerically applied to monitor and analyze the mechanical behavior of a cracked lamina/laminate structures subjected to tensile and flexural loadings. In this context, the experimental input to be given to the iFEM-PD system is simulated using the direct PD analysis. Subsequently, this synthetic strain data is analyzed utilizing various coarse and fine iFEM sensor placement models. For each sensor network, full-field shape and strain sensing results are generated for the critical time steps of the crack propagation within the composite structures. In other words, the three-dimensional displacements that occur in the structure in case of crack propagation are calculated through performing iFEM analysis, and using this deformation information, full-field von Mises strains are obtained for all sensor placement configurations.

Comparison of the deformation results produced by iFEM with reference solutions demonstrates high accuracy of iFEM-PD approach for displacement reconstruction during crack growth. Moreover, the full-field strains estimated by iFEM are employed to define the critical regions of the laminates, especially at the vicinity of the cracks, where the equivalent strains exceed 10000 μm/m. Providing iFEM deformation data obtained at the boundaries of this critical region to the PD model as the boundary condition enables the prognosis of the damage propagation within the critical region. In addition, the full-field deformations of the critical zone are reevaluated through the iFEM-PD hybrid system. Accordingly, the SHM results indicated that utilization of the nonlocal PD kinematics with the iFEM formulation enables accurate displacement and damage estimation within the laminate. Namely, precise displacement distribution is achieved as compared to the reference solution, thus validating the iFEM-PD for shape sensing in hot-spot regions of the damaged structures. Furthermore, the crack growth results obtained from the iFEM-PD system are

rigorously compared with the reference results, demonstrating the superior capabilities of this new damage/crack monitoring algorithm. The results in Sections 3.1 and 3.2 show that the cracks are propagated along with the fiber directions, indicating that the fibers are not damaged due to the small-scale imposed load and the matrix cracks are propagated through the fiber direction. Additionally, the underlying discretization and horizon sizes have no effect to the results as explained in our previous studies [97-99]. Nevertheless, the current formulation can be extended by using dual-horizon peridynamics [108-109] effectively for non-uniform discretization sizes in future studies. All in all, the numerical results verify the full-field displacement and strain monitoring capabilities of the iQS4 element for a growing crack in composites, and clearly demonstrate that the iFEM-PD methodology is robust for realistic SHM applications.

In addition to the numerical verification, experimental validation of the iFEM-PD methodology is performed on a woven-fabric tensile test specimen. These specimens are prepared with a central crack and their fracture patterns are observed utilizing DIC contactless monitoring systems during the mechanical test. Moreover, iFEM-PD simulations of these specimens are conducted using coarse (low-fidelity discretization) and sparse (missing data) sensor placement iQS4 models, where several locations at the vicinity of the crack have no sensors. According to the results obtained in Section 3.3, the iFEM-PD methodology can predict a highly accurate position of the damage albeit no *'a priori'* knowledge of the crack position in the iQS4 model. Comparison of the crack growth paths estimated by iFEM-PD and DIC systems reveals that the present SHM model is superior for crack monitoring in an experimental test of composite structures. Furthermore, the DIC images show that the fibers are broken in the woven fabric, which is identically predicted with the iFEM-PD approach. It is also observed that the sparse sensor placement model has no drawback on the accuracy of the reconstructed results, confirming the practical utility of the iFEM-PD methodology. Hence, it can be concluded that the findings of this study demonstrate the high potential of the iFEM-PD computational platform for real-time shape sensing and damage/crack propagation monitoring in engineering structures. Finally, it is important to restate that the present iFEM formulation is applicable for curved-shell structures whereas the present iFEM-PD methodology is only valid for straight plate structures due to the PD laminate model. To fully upgrade this methodology for shell structures, the PD formulation can be extended for curved structures with the help of references [110-111] in future works.

Acknowledgement

The financial support provided by the Scientific and Technological Research Council of Turkey (TUBITAK) under the grant No: 217M207 is greatly acknowledged.

References

[1] Stull, C.J., Earls, C.J. and Koutsourelakis, P.S., 2011. Model-based structural health monitoring of naval ship hulls. Computer Methods in Applied Mechanics and Engineering, 200(9-12), pp.1137-1149.

[2] Giurgiutiu, V., 2020. Structural health monitoring (SHM) of aerospace composites. In Polymer composites in the aerospace industry (pp. 491-558). Woodhead Publishing.

[3] Song, Gangbing, Chuji Wang, and Bo Wang. "Structural health monitoring (SHM) of civil structures." (2017): 789.

[4] Farrar, C.R. and Worden, K., 2010. An introduction to structural health monitoring. New Trends in Vibration Based Structural Health Monitoring, pp.1-17.

[5] Van der Auweraer, H. and Peeters, B., 2003. Sensors and systems for structural health monitoring. Journal of Structural Control, 10(2), pp.117-125.

[6] Sebastian, J., Schehl, N., Bouchard, M., Boehle, M., Li, L., Lagounov, A. and Lafdi, K., 2014. Health monitoring of structural composites with embedded carbon nanotube coated glass fiber sensors. Carbon, 66, pp.191-200.

[7] Amorebieta, J., Ortega-Gomez, A., Durana, G., Fernández, R., Antonio-Lopez, E., Schülzgen, A., Zubia, J., Amezcua-Correa, R. and Villatoro, J., 2021. Compact omnidirectional multicore fiber-based vector bending sensor. Scientific Reports, 11(1), pp.1-11.

[8] Glisic, B. and Inaudi, D., 2008. Fibre optic methods for structural health monitoring. John Wiley & Sons.

[9] Di Sante, R., 2015. Fibre optic sensors for structural health monitoring of aircraft composite structures: Recent advances and applications. Sensors, 15(8), pp.18666-18713.

[10] Nicolas, M.J., Sullivan, R.W. and Richards, W.L., 2016. Large scale applications using FBG sensors: determination of in-flight loads and shape of a composite aircraft wing. Aerospace, 3(3), p.18.

[11] Amanzadeh, M., Aminossadati, S.M., Kizil, M.S. and Rakić, A.D., 2018. Recent developments in fibre optic shape sensing. Measurement, 128, pp.119-137.

[12] Kurashima, T., Horiguchi, T. and Tateda, M., 1990. Distributed-temperature sensing using stimulated Brillouin scattering in optical silica fibers. Optics letters, 15(18), pp.1038-1040.

[13] Posey, R., Johnson, G.A. and Vohra, S.T., 2000. Strain sensing based on coherent Rayleigh scattering in an optical fibre. Electronics Letters, 36(20), pp.1688-1689.

[14] Ko, W.L., Richards, W.L. and Fleischer, V.T., 2009. Applications of Ko displacement theory to the deformed shape predictions of the doubly-tapered Ikhana Wing. NASA/TP-2009-214652.

[15] Jutte, C.V., Ko, W.L., Stephens, C.A., Bakalyar, J.A. and Richards, W.L., 2011. Deformed shape calculation of a full-scale wing using fiber optic strain data from a ground loads test. NASA/TP-2011-215975

[16] Davis, M.A., Kersey, A.D., Sirkis, J. and Friebele, E.J., 1996. Shape and vibration mode sensing using a fiber optic Bragg grating array. Smart Materials and Structures, 5(6), p.759.

[17] Bogert, P. B., Haugse, E. D., and Gehrki, R. E., 2003. Structural shape identification from experimental strains using a modal transformation technique. In Proceedings of 44th AIAA/ASME/ASCE/AHS Structures, Structural Dynamics and Materials Conference, Norfolk, Virginia.

[18] Kim, N. S., and Cho, N. S., 2004. Estimating deflection of a simple beam model using fiber optic Bragg-grating sensors. Experimental Mechanics, 44(4), pp. 433-439.

[19] Bruno, R., Toomarian, N. and Salama, M., 1994. Shape estimation from incomplete measurements: a neural-net approach. Smart Materials and Structures, 3(2), p.92.

[20] Moreira, L. and Soares, C.G., 2020. Neural network model for estimation of hull bending moment and shear force of ships in waves. Ocean Engineering, 206, p.107347.

[21] Nguyen, H., Tran, T., Wang, Y. and Wang, Z., 2021. Three-dimensional shape reconstruction from single-shot speckle image using deep convolutional neural networks. Optics and Lasers in Engineering, 143, p.106639.

[22] Xu, K. and Darve, E., 2021. Solving inverse problems in stochastic models using deep neural networks and adversarial training. Computer Methods in Applied Mechanics and Engineering, 384, p.113976.

[23] Tessler, A., and Spangler, J. L., 2005. A least-squares variational method for full-field reconstruction of elastic deformations in shear-deformable plates and shells. Computer Methods in Applied Mechanics and Engineering, 194(2), pp. 327-339.

[24] Tikhonov, A. N., and Arsenin, V. Y., 1977. Solutions of ill-posed problems. Winston, Washington, DC.

[25] Cortiella, A., Park, K.C., and Doostan, A., 2021. Sparse identification of nonlinear dynamical systems via reweighted ℓ1-regularized least squares. Computer Methods in Applied Mechanics and Engineering, 376, p.113620.

[26] Wang, L., Wang, Z., and Qian, Z., 2017. A meshfree method for inverse wave propagation using collocation and radial basis functions. Computer Methods in Applied Mechanics and Engineering, 322, pp.311-350.

[27] Li, X.Y. and Law, S.S., 2010. Adaptive Tikhonov regularization for damage detection based on nonlinear model updating. Mechanical Systems and Signal Processing, 24(6), pp.1646-1664.

[28] Gherlone, M., Cerracchio, P. and Mattone, M., 2018. Shape sensing methods: Review and experimental comparison on a wing-shaped plate. Progress in Aerospace Sciences, 99, pp.14-26.

[29] Esposito, M. and Gherlone, M., 2020. Composite wing box deformed-shape reconstruction based on measured strains: Optimization and comparison of existing approaches. Aerospace Science and Technology, 99, p.105758.

[30] Esposito, M. and Gherlone, M., 2021. Material and strain sensing uncertainties quantification for the shape sensing of a composite wing box. Mechanical Systems and Signal Processing, 160, p.107875.

[31] Ren, L., You, R., Liu, J. and Li, H., 2021. Development of a novel inclinometer by inverse finite element method for soil deformation monitoring. Smart Materials and Structures, 30(8), p.085037.

[32] Tessler, A., and Spangler, J. L., 2004. Inverse FEM for full-field reconstruction of elastic deformations in shear deformable plates and shells. In: Proceedings of 2nd European Workshop on Structural Health Monitoring, Munich, Germany.

[33] Kefal, A., Oterkus, E., Tessler, A., and Spangler, J.L., 2016. A quadrilateral inverse-shell element with drilling degrees of freedom for shape sensing and structural health monitoring. Engineering Science and Technology, an International Journal, 19, pp. 1299-1313.

[34] Kefal, A., 2019. An efficient curved inverse-shell element for shape sensing and structural health monitoring of cylindrical marine structures. Ocean Engineering, 188, p.106262.

[35] Kefal, A., and Oterkus, E., 2016. Displacement and stress monitoring of a chemical tanker based on inverse finite element method. Ocean Engineering, 112, pp. 33-46.

[36] Kefal, A., and Oterkus, E., 2016. Displacement and stress monitoring of a Panamax containership using inverse finite element method. Ocean Engineering, 119, pp. 16-29.

[37] Kefal, A., Mayang, J.B., Oterkus, E., Yildiz, M., 2018. Three dimensional shape and stress monitoring of bulk carriers based on iFEM methodology. Ocean Engineering, 147, 256-267.

[38] Kobayashi, M., Jumonji, T. and Murayama, H., 2019, September. Three-dimensional shape sensing by inverse finite element method based on distributed fiber-optic sensors. In Practical Design of Ships and Other Floating Structures (pp. 40-48). Springer, Singapore.

[39] Li, M., Kefal, A., Oterkus, E. and Oterkus, S., 2020. Structural health monitoring of an offshore wind turbine tower using iFEM methodology. Ocean Engineering, 204, p.107291.

[40] Oboe, D., Colombo, L., Sbarufatti, C. and Giglio, M., 2021. Comparison of strain pre-extrapolation techniques for shape and strain sensing by iFEM of a composite plate subjected to compression buckling. Composite Structures, 262, p.113587.

[41] Oboe, D., Colombo, L., Sbarufatti, C. and Giglio, M., 2021. Shape Sensing of a Complex Aeronautical Structure with Inverse Finite Element Method. Sensors, 21(4), p.1388.

[42] Roy, R., Tessler, A., Surace, C. and Gherlone, M., 2020. Shape Sensing of Plate Structures Using the Inverse Finite Element Method: Investigation of Efficient Strain–Sensor Patterns. Sensors, 20(24), p.7049.

[43] Abdollahzadeh, M.A., Kefal, A. and Yildiz, M., 2020. A comparative and review study on shape and stress sensing of flat/curved shell geometries using C0-continuous family of iFEM elements. Sensors, 20(14), p.3808.

[44] Colombo, L., Sbarufatti, C., Giglio, M., 2019. Definition of a load adaptive baseline by inverse finite element method for structural damage identification. Mechanical Systems and Signal Processing, 120, 584-607.

[45] Roy, R., Gherlone, M. and Surace, C., 2020. Damage Localisation in Thin Plates Using the Inverse Finite Element Method. In Proceedings of the 13th International Conference on Damage Assessment of Structures (pp. 199-212). Springer, Singapore.

[46] Li, M., Kefal, A., Cerik, B.C. and Oterkus, E., 2020. Dent damage identification in stiffened cylindrical structures using inverse Finite Element Method. Ocean Engineering, 198, p.106944.

[47] Roy, R., Gherlone, M., Surace, C. and Tessler, A., 2021. Full-Field Strain Reconstruction Using Uniaxial Strain Measurements: Application to Damage Detection. Applied Sciences, 11(4), p.1681.

[48] Li, M., Wu, Z., Yang, H. and Huang, H., 2021. Direct damage index based on inverse finite element method for structural damage identification. Ocean Engineering, 221, p.108545.

[49] Li, T., Cao, M., Li, J., Yang, L., Xu, H. and Wu, Z., 2021. Structural Damage Identification Based on Integrated Utilization of Inverse Finite Element Method and Pseudo-Excitation Approach. Sensors, 21(2), p.606.

[50] Gherlone, M., Cerracchio, P., Mattone, M., Di Sciuva, M., and Tessler, A., 2012. Shape sensing of 3D frame structures using an inverse finite element method. International Journal of Solids and Structures, 49(22), pp. 3100-3112.

[51] Savino, P., Gherlone, M. and Tondolo, F., 2019. Shape sensing with inverse finite element method for slender structures. Structural Engineering and Mechanics, 72(2), pp.217-227.

[52] You, R., Ren, L., Yuan, C. and Song, G., 2021. Two-Dimensional Deformation Estimation of Beam-Like Structures Using Inverse Finite-Element Method: Theoretical Study and Experimental Validation. Journal of Engineering Mechanics, 147(5), p.04021019.

[53] You, R. and Ren, L., 2021. An enhanced inverse beam element for shape estimation of beam-like structures. Measurement, p.109575.

[54] Gherlone, M., Cerracchio, P., Mattone, M., Di Sciuva, M., and Tessler, A., 2014. An inverse Finite Element Method for beam shape sensing: theoretical framework and experimental validation. Smart Materials and Structures, 23(4), pp. 045027.

[55] Song, X. and Liang, D., 2018. Dynamic displacement prediction of beam structures using fiber bragg grating sensors. Optik, 158, pp.1410-1416.

[56] Savino, P., Tondolo, F., Gherlone, M. and Tessler, A., 2020. Application of Inverse Finite Element Method to Shape Sensing of Curved Beams. Sensors, 20(24), p.7012.

[57] Roy, R., Gherlone, M. and Surace, C., 2021. A shape sensing methodology for beams with generic cross-sections: Application to airfoil beams. Aerospace Science and Technology, 110, p.106484.

[58] Kefal, A. and Oterkus, E., 2020. Isogeometric iFEM analysis of thin shell structures. Sensors, 20(9), p.2685.

[59] Kefal, A. and Oterkus, E., 2017. Shape Sensing of Aerospace Structures by Coupling Isogeometric Analysis and Inverse Finite Element Method. In Proceedings of 58th AIAA/ASCE/AHS/ASC Structures, Structural Dynamics, and Materials Conference (p. 0427).

[60] Kefal, A., 2017. Structural health monitoring of marine structures by using inverse finite element method (Doctoral dissertation, University of Strathclyde).

[61] Hughes, T.J., Cottrell, J.A. and Bazilevs, Y., 2005. Isogeometric analysis: CAD, finite elements, NURBS, exact geometry and mesh refinement. Computer methods in applied mechanics and engineering, 194(39-41), pp.4135-4195.

[62] Cottrell, J.A., Hughes, T.J. and Bazilevs, Y., 2009. Isogeometric analysis: toward integration of CAD and FEA. John Wiley & Sons.

[63] Zhao, F., Xu, L., Bao, H. and Du, J., 2020. Shape sensing of variable cross-section beam using the inverse finite element method and isogeometric analysis. Measurement, 158, p.107656.

[64] Zhao, F. and Bao, H., 2021. An improved inverse finite element method for shape sensing using isogeometric analysis. Measurement, 167, p.108282.

[65] Tessler, A., Di Sciuva, M., and Gherlone, M., 2010. A consistent refinement of first-order shear deformation theory for laminated composite and sandwich plates using improved zigzag kinematics. Journal of Mechanics of Materials and Structures, 5(2), pp. 341-367.

[66] Cerracchio, P., Gherlone, M., Di Sciuva, M., Tessler, A., 2015. A novel approach for displacement and stress monitoring of sandwich structures based on the inverse Finite Element Method. Composite Structures, 127, 69-76.

[67] Kefal, A., Tessler, A., Oterkus, E., 2017. An enhanced inverse finite element method for displacement and stress monitoring of multilayered composite and sandwich structures. Composite Structures, 179, 514-540.

[68] Zhao, F., Bao, H., Liu, J. and Li, K., 2021. Shape sensing of multilayered composite and sandwich beams based on Refined Zigzag Theory and inverse finite element method. Composite Structures, 261, p.113321.

[69] Kefal, A., Yildiz, M., 2017. Modeling of Sensor Placement Strategy for Shape Sensing and Structural Health Monitoring of a Wing-Shaped Sandwich Panel Using Inverse Finite Element Method. Sensors, 17(12), 2775.

[70] Kefal, A., Tabrizi, I.E., Tansan, M., Kisa, E. and Yildiz, M., 2021. An experimental implementation of inverse finite element method for real-time shape and strain sensing of composite and sandwich structures. Composite Structures, 258, p.113431.

[71] Kefal, A., Tabrizi, I.E., Yildiz, M. and Tessler, A., 2021. A smoothed iFEM approach for efficient shape-sensing applications: Numerical and experimental validation on composite structures. Mechanical Systems and Signal Processing, 152, p.107486.

[72] Farrar, C.R. and Lieven, N.A., 2007. Damage prognosis: the future of structural health monitoring. Philosophical Transactions of the Royal Society A: Mathematical, Physical and Engineering Sciences, 365(1851), pp.623-632.

[73] Bigoni, C. and Hesthaven, J.S., 2020. Simulation-based anomaly detection and damage localization: an application to structural health monitoring. Computer Methods in Applied Mechanics and Engineering, 363, p.112896.

[74] He, W.Y., Zhu, S. and Chen, Z.W., 2017. Wavelet-based multi-scale finite element modeling and modal identification for structural damage detection. Advances in Structural Engineering, 20(8), pp.1185-1195.

[75] Bigoni, C., Zhang, Z. and Hesthaven, J.S., 2020. Systematic sensor placement for structural anomaly detection in the absence of damaged states. Computer Methods in Applied Mechanics and Engineering, 371, p.113315.

[76] Read, I., Foote, P. and Murray, S., 2001. Optical fibre acoustic emission sensor for damage detection in carbon fibre composite structures. Measurement Science and Technology, 13(1), p.N5.

[77] Tabrizi, I.E., Kefal, A., Zanjani, J.S.M., Akalin, C. and Yildiz, M., 2019. Experimental and numerical investigation on fracture behavior of glass/carbon fiber hybrid composites using acoustic emission method and refined zigzag theory. Composite structures, 223, p.110971.

[78] Ali, H.Q., Tabrizi, I.E., Khan, R.M.A., Tufani, A. and Yildiz, M., 2019. Microscopic analysis of failure in woven carbon fabric laminates coupled with digital image correlation and acoustic emission. Composite Structures, 230, p.111515.

[79] Tabrizi, I.E., Khan, R.M.A., Massarwa, E., Zanjani, J.S.M., Ali, H.Q., Demir, E. and Yildiz, M., 2019. Determining tab material for tensile test of CFRP laminates with combined usage of digital image correlation and acoustic emission techniques. Composites Part A: Applied Science and Manufacturing, 127, p.105623.

[80] AlKhateab, B., Tabrizi, I.E., Zanjani, J.S.M., Rahimi, M.N., Poudeh, L.H., Kefal, A. and Yildiz, M., 2020. Damage mechanisms in CFRP/HNT laminates under flexural and in-plane shear loadings using experimental and numerical methods. Composites Part A: Applied Science and Manufacturing, 136, p.105962.

[81] Zhang, H., Zhang, X. and Qiao, P., 2021. A new peridynamic mixed-mode bond failure model for interface delamination and homogeneous materials fracture analysis. Computer Methods in Applied Mechanics and Engineering, 379, p.113728.

[82] Zhi, J. and Tay, T.E., 2019. Explicit modeling of matrix cracking and delamination in laminated composites with discontinuous solid-shell elements. Computer Methods in Applied Mechanics and Engineering, 351, pp.60-84.

[83] Vadakke, V., and Carlsson, L.A., 2004. Experimental investigation of compression failure of sandwich specimens with face/core debond. Composites Part B: Engineering, 35(6), pp. 583-590.

[84] Silling, S.A., 2000. Reformulation of elasticity theory for discontinuities and long-range forces. Journal of the Mechanics and Physics of Solids, 48(1), pp.175-209.

[85] Javili, A., Morasata, R., Oterkus, E. and Oterkus, S., 2019. Peridynamics review. Mathematics and Mechanics of Solids, 24(11), pp.3714-3739.

[86] Diehl, P., Prudhomme, S. and Lévesque, M., 2019. A review of benchmark experiments for the validation of peridynamics models. Journal of Peridynamics and Nonlocal Modeling, 1(1), pp.14-35.

[87] Bode, T., Weißenfels, C. and Wriggers, P., 2021. A consistent peridynamic formulation for arbitrary particle distributions. Computer Methods in Applied Mechanics and Engineering, 374, p.113605.

[88] Kefal, A., Sohouli, A., Oterkus, E., Yildiz, M. and Suleman, A., 2019. Topology optimization of cracked structures using peridynamics. Continuum Mechanics and Thermodynamics, 31(6), pp.1645-1672.

[89] Sohouli, A., Kefal, A., Abdelhamid, A., Yildiz, M. and Suleman, A., 2020. Continuous density-based topology optimization of cracked structures using peridynamics. Structural and Multidisciplinary Optimization, 62, pp.2375-2389.

[90] Xu, J., Askari, A., Weckner, O. and Silling, S., 2008. Peridynamic analysis of impact damage in composite laminates. Journal of Aerospace Engineering, 21(3), pp.187-194.

[91] Kilic, B., Agwai, A. and Madenci, E., 2009. Peridynamic theory for progressive damage prediction in center-cracked composite laminates. Composite Structures, 90(2), pp.141-151.

[92] Hu, W., Ha, Y.D. and Bobaru, F., 2012. Peridynamic model for dynamic fracture in unidirectional fiber-reinforced composites. Computer Methods in Applied Mechanics and Engineering, 217, pp.247-261.

[93] Mehrmashhadi, J., Chen, Z., Zhao, J. and Bobaru, F., 2019. A stochastically homogenized peridynamic model for intraply fracture in fiber-reinforced composites. Composites Science and Technology, 182, p.107770.

[94] Yu, Y. and Wang, H., 2014. Peridynamic analytical method for progressive damage in notched composite laminates. Composite Structures, 108, pp.801-810.

[95] Guo, J., Gao, W., Liu, Z., Yang, X. and Li, F., 2019. Study of Dynamic Brittle Fracture of Composite Lamina Using a Bond-Based Peridynamic Lattice Model. Advances in Materials Science and Engineering, 2019.

[96] Hu, Y.L., Yu, Y. and Madenci, E., 2020. Peridynamic modeling of composite laminates with material coupling and transverse shear deformation. Composite Structures, 253, p.112760.

[97] Oterkus, E. and Madenci, E., 2012. Peridynamic analysis of fiber-reinforced composite materials. Journal of Mechanics of Materials and Structures, 7(1), pp.45-84.

[98] Oterkus, E., Madenci, E., Weckner, O., Silling, S., Bogert, P. and Tessler, A., 2012. Combined finite element and peridynamic analyses for predicting failure in a stiffened composite curved panel with a central slot. Composite Structures, 94(3), pp.839-850.

[99] Diyaroglu, C., Oterkus, E., Madenci, E., Rabczuk, T. and Siddiq, A., 2016. Peridynamic modeling of composite laminates under explosive loading. Composite Structures, 144, pp.14-23.

[100] Ren, H., Zhuang, X. and Rabczuk, T., 2020. A nonlocal operator method for solving partial differential equations. Computer Methods in Applied Mechanics and Engineering, 358, p.112621.

[101] Rabczuk, T., Ren, H. and Zhuang, X., 2019. A nonlocal operator method for partial differential equations with application to electromagnetic waveguide problem. Computers, Materials & Continua 59 (2019), Nr. 1.

[102] Tessler, A., Riggs, H. R., Freese, C. E., and Cook, G. M., 1998. An improved variational method for finite element stress recovery and a posteriori error estimation. Computer Methods in Applied Mechanics and Engineering, 155(1), pp. 15-30.

[103] Abdollahzadeh, M.A., Tabrizi, I.E., Kefal, A. and Yildiz, M., 2021. A Combined Experimental/Numerical Study on Deformation Sensing of Sandwich Structures through Inverse Analysis of Pre-Extrapolated Strain Measurements. Measurement, p.110031.

[104] Tessler, A. and Hughes, T.J., 1983. An improved treatment of transverse shear in the Mindlin-type four-node quadrilateral element. Computer methods in applied mechanics and engineering, 39(3), pp.311-335

[105] Madenci, E. and Oterkus, E., 2014. Peridynamic theory. In Peridynamic Theory and Its Applications (pp. 19-43). Springer, New York, NY.

[106] Lapidus, L. and Pinder, G.F., 2011. Numerical solution of partial differential equations in science and engineering. John Wiley & Sons.

[107] Kefal, A., Tabrizi, I. E. and Yıldız, M., 2021. Real-time monitoring of crack propagation in fiber-reinforced composite plates using iFEM methodology. In Proceedings of 8th International Conference on Marine Structures (MARSTRUCT2021), Trondheim, Norway. *Appeared in* Amdahl, J. and Guedes Soares, C. (Eds.) Developments in the Analysis and Design of Marine Structures. CRC Press.

[108] Ren, H., Zhuang, X., Cai, Y. and Rabczuk, T., 2016. Dual-horizon peridynamics. International Journal for Numerical Methods in Engineering, 108(12), pp.1451-1476.

[109] Ren, H., Zhuang, X. and Rabczuk, T., 2017. Dual-horizon peridynamics: A stable solution to varying horizons. Computer Methods in Applied Mechanics and Engineering, 318, pp.762-782.

[110] Chowdhury, S.R., Roy, P., Roy, D. and Reddy, J.N., 2016. A peridynamic theory for linear elastic shells. International Journal of Solids and Structures, 84, pp.110-132.

[111] Zhang, Q., Li, S., Zhang, A.M., Peng, Y. and Yan, J., 2021. A peridynamic Reissner-Mindlin shell theory. International Journal for Numerical Methods in Engineering, 122(1), pp.122-147.